OUT-OF-PHASE THERMOMECHANICAL FATIGUE OF MONOLITHIC TITANIUM ALLOYS

Thesis

Submitted to

Graduate Engineering & Research
School of Engineering

University of Dayton

In Partial Fulfillment of the Requirements for

The Degree

Master of Science in Materials Engineering

by

Carl Boehlert

University of Dayton

Dayton, Ohio

May, 1993

OUT-OF-PHASE THERMOMECHANICAL FATIGUE OF MONOLITHIC TITANIUM ALLOYS

APPROVED BY:

Dr. D. Eylon, D. Sc.
Professor
Chemical & Materials Engineering
Committee Chairman

Dr. J.A. Snide, Ph. D.
Professor and Chair
Chemical & Materials Engineering
Committee Member

Dr. K. Krishnamurthy, Ph. D.
Associate Professor
Chemical & Materials Engineering
Committee Member

Franklin Eastep, Ph. D.
Interim Associate Dean/Director
Graduate Engineering & Research
School of Engineering

Joseph Lestingi, D. E., P. E.
Dean
School of Engineering

ABSTRACT

OUT-OF-PHASE THERMOMECHANICAL FATIGUE OF MONOLITHIC TITANIUM ALLOYS

Name: Boehlert, Carl Joseph
University of Dayton, 1993

Faculty Advisor: Dr. Daniel Eylon
Technical Advisor: Mr. Stephan Russ

Before being accepted for practical application, titanium matrix composites, some of the most recent advanced materials being evaluated for high temperature aerospace engine components, need to be evaluated under simulated service conditions involving the simultaneous cycling of temperature and applied load, thermomechanical fatigue. Out-of-phase thermomechanical fatigue conditions provide a more severe test on the matrix of these composites. Due to the in'.erent consolidation difficulties and expense associated with metal matrix composites today, it is beneficial to correlate and project composite behavior from the evaluation of fiberless matrices. This work investigated the out-of-phase thermomechanical fatigue behavior of three classes of titanium alloys; alpha-2, beta, and near-orthorhombic, in monolithic sheet form, in order to compare material behaviors and correlate monolithic behavior to composite behavior under similar testing conditions. Testing were performed with maximum stresses ranging from 350-700 MPa, minimum stresses ranging from 17.5-35 MPa, temperature ranging from 150-650°, and a frequency associated with three minute cycling. Fatigue, oxidation, and creep damage mechanisms participated in failures where crack initiation and propagation played an important role in fatigue life. Comparing alloys, the beta alloy, Timetal 21S, exhibited the greatest fatigue strength at the highest stress ranges and the worst fatigue

strength at the lowest stress ranges. The near-orthorhombic alloy, Ti-23.5Al-16.5Nb(at%), exhibited good fatigue strength over the entire tested stress range, holding the advantage at intermediate stress ranges. The alpha-2 alloy, Ti-24Al-11Nb(at%), exhibited the greatest fatigue strength at the the lowest stress and the worst fatigue strength at the highest stresses. Using a micromechanical stress analysis code for composites, a correlation was proposed linking calculated matrix stress range and composite experimental data to applied monolithic stress range and monolithic experimental data.

ACKNOWLEDGMENTS

This work was conducted under the Educational Partnership Agreement (EPA) between Wright Laboratory Materials Directoriate at Wright Patterson Air Force Base and the University of Dayton. The specimen machining was performed by Stan Hilton at the University of Dayton Research Institute (UDRI). The specimen testing, metallography, and fractography were performed at Wright Laboratory Materials Directorate.

The experimentation and development of this thesis could not have been performed without the help of others. I thank Drs. Daniel Eylon and James Snide for the opportunity and support necessary for the completion of this thesis. I thank Paul Smith, Materials Directorate, for the opportunity to be involved in this specific research project. I am grateful to John Porter for his advice and guidance in use of the SEM and Eric Fletcher, Michael Scott, and Robert Lewis for their helpful discussions on metallography. I am sincerely indebted to Steve Russ, Materials Directorate, for his valuable assistance, patience, and instruction in the completion of this thesis.

TABLE OF CONTENTS

LIST OF ILLUSTRATIONS

LIST OF TABLES

LIST OF ABBREVIATIONS AND SYMBOLS

at%	Atomic Percent
BCC	Body Center Cubic
ß	disordered beta phase titanium
ß2	ordered beta phase titanium
CTE	Coefficient of Thermal Expansion
DAC	Data Acquisition Cycle
FIDEP	Finite Difference Code for Elastic-Plastic Analysis of Composites
HCP	Hexagonal Close Packed
HIP	Hot Isostatically Pressing
Hv	Vickers Hardness
IF	Isothermal Fatigue
IP	In-Phase
LPBP	Load Phase Break Point
MMC	Metal Matrix Composite
OM	Optical Microscopy
OOP	Out-of-phase
PC	Personal Computer
Seff	Effective Stress
SEM	Scanning Electron Microscopy
S-N Curve	Stress versus Fatigue Life Data Plot
Sz	Axial Stress
TEM	Transmission Electron Microscope
TMC	Titanium Matrix Composite
TMF	Thermomechanical Fatigue
TPBP	Temperature Phase Break Point
UDRI	University of Dayton Research Institute
wt%	Weight Percent

INTRODUCTION

Today, the aerospace industry needs materials with higher strength and lower density, especially for high temperature applications. Envisioned advanced turbine engines and hypersonic airframes will demand temperature, strength, stiffness, and weight requirements that cannot be achieved with available conventional materials. Specific components are being designed for sustained and cyclic loading conditions at temperatures of 550°C and higher, some approaching 815°C. Titanium matrix composites (TMCs) represent one class of materials currently being pursued for these extreme conditions. Present emphasis is focused on high temperature titanium and titanium-aluminides as matrix alloys. A first generation titanium-aluminide composite, SCS-6/Ti-24Al-11Nb(at%), has attractive properties, but only over a limited temperature range due to its susceptibility to oxygen embrittlement and environmentally assisted cracking[1-10]. A more ductile beta titanium alloy matrix composite, SCS-6/Timetal 21S, has exhibited properties which are viewed as sufficient for use as an airframe material for a potential hypersonic aircraft[11]. More recently "orthorhombic" titanium alloys (containing an orthorhombic Ti_2AlNb phase), because of their high strength and fracture toughness at temperature, are being considered for use as matrix alloys[12].

The eventual utilization of TMCs is dependent upon, among other things, the ability to understand, characterize, and model their mechanical behavior. It is essential that the potential materials be evaluated under similar temperature and loading conditions as will be experienced during projected flights. Cyclic thermomechanical fatigue (TMF) conditions exist in aerospace engines, and therefore must be simulated to evaluate

materials for adequate strength and fatigue resistance at temperature. Russ et. al.[7] investigated the SCS-6/Ti-24Al-11Nb(at%) composite under various TMF conditions. A life fraction model was proposed that contained fiber stress dominant and matrix stress dominant terms. In these experiments the out-of-phase (OOP) TMF tests, where the maximum stress and maximum temperature are applied in an out-of-phase sequence, was governed predominantly by the matrix term. Correspondingly, a matrix dominated failure mechanism was also observed. Hanson[13] and Mall et. al.[14] demonstrated that the life fraction model could be adopted to an SCS-6/Timetal 21S $[0/90]_{2S}$ composite. Others have found OOP TMF to be a matrix dominated phenomenon as well[15-17]. Based on these observations, OOP TMF would be the most sensitive test to evaluate matrix effects in fatigue and TMF. Because of the large expense and consolidation difficulties inherent to metal matrix composites (MMCs), it would be beneficial to correlate composite behavior to monolithic behavior. This study will investigate the OOP TMF behavior of monolithic titanium alloys in an effort to characterize differing material behaviors and correlate monolithic and composite behavior under similar testing parameters.

The monolithic materials used in this study included three classes of titanium: the beta alloy, Timetal 21S, the alpha-2 + beta alloy, Ti-24Al-11Nb(at%), and the alpha-2 + beta + orthorhombic alloy, Ti-23.5Al-16.5Nb(at%), all in 2 mm thick rolled sheet form. To date, no published work has addressed the out-of-phase thermomechanical fatigue behavior of any of the above mentioned monolithic sheet materials. The samples were systematically tested in OOP thermomechanical load control fatigue to characterize the effects on the monolithic alloys. No fiber reinforced materials were tested in this work. Comparison OOP TMF results of the SCS-6/Timetal 21S and SCS-6/Ti-24Al-11Nb(at%) composite systems, for similar stress levels the SCS-6/Timetal 21S composite experienced longer OOP TMF lives than the SCS-6/Ti-24Al-11Nb[7,17]. Therefore, it is expected in this work that monolithic Timetal 21S will experience longer lives than Ti-

24Al-11Nb. OOP TMF testing on the "orthorhombic" composite system has not been extensively performed.

All tests were run at 0.00556 Hz (3 minute cycle) with a minimum temperature of 150°C and a maximum temperature of 650°C and a stress ratio ($\sigma_{min}/\sigma_{max}$) of 0.05. Stress, temperature, and strain data were monitored and recorded throughout the tests and evaluated for indications of damage progression. Fractography and metallography of failed samples were conducted in attempt to gain insight into the primary mechanical and environmental damage mechanisms inherent to the various monolithic alloys. Additional analysis correlating applied and micromechanical stresses and cycles-to-failure was performed in order to determine parameters that may assist in predicting TMF lives of TMCs.

CHAPTER I

BACKGROUND

This chapter is intended to include a general review of the current literature involving topics related to this study. For the readers' convenience this section is divided into four topical parts: material description, TMF description, damage mechanisms in TMF, life correlation, and micromechanical analysis.

Material Description

Associated with each titanium alloy studied are variations in microstructural conditions. During processing of titanium alloys, several phases can be produced as a result of specified heat treatments and alloy additions. The phases present play an important role in determining the properties and characteristic behavior of the alloy. For example, the crystal structure of pure titanium below 885°C is hexagonal close packed (HCP); however, beta phase titanium has a body center cubic (BCC) crystal structure which is characteristic of most ductile metals[18]. During deformation, BCC structures have a greater capability for slip in several directions. This accounts for the increased elongation characteristic of beta phase titanium, which is much more ductile than either the alpha, alpha-2, orthorhombic, or omega phases. Timetal 21S is comprised primarily of beta phase due to the high concentration of molybdenum. It should be noted that in the aged condition, this alloy has a structure of fine precipitated alpha in a continuous matrix of beta phase. In contrast, the HCP alpha-2 phase, which comprises the greatest volume fraction of Ti-24Al-11Nb, is less ductile, especially at low temperature, and therefore

exhibits low strains-to-failure when pulled in tension. The orthorhombic phase, present in small amounts in Ti-23.5Al-16.5Nb, lies somewhere between the ductile and brittle phases mentioned. It possesses more ductility than the alpha-2 phase at high temperatures and less ductility than the beta phase. A more comprehensive description of the microstructures associated with the three titanium alloys studied is provided in Chapter II.

MMCs

MMCs, consisting of ceramic fibers embedded in a metallic matrix, combine high strength and stiffness with low density. The intent is to combine the attractive properties of both the matrix and reinforcement to provide unique properties for structural design. Figure 1 compares the room temperature properties of a silicon carbide (SiC) fiber commonly used in TMCs, SCS-6, to those of the three matrices studied. If the fiber properties can be incorporated into the matrix, TMCs should provide a unique combination of properties not attainable by the matrix alone. SCS-6 is a beta silicon carbide monofilament having a diameter of 142 micrometers and containing a double pass carbon rich outer coating added to reduce reaction with titanium matrices[19]. Manufacture of the composite systems referenced involved hot-isostatically pressing (HIP) layers of matrix to layers of fibers using the foil/fiber/foil technique [20,21].

Understanding MMC mechanical behavior, especially under fatigue, is complicated by the differences in strength, ductility, volume fraction, and coefficient of thermal expansion (CTE) of the matrix and fiber[21,22]. During the consolidation of MMCs the matrix is deformed around the fibers and diffusion bonded. This process occurs at relatively high pressures and temperatures. When cooled, residual micromechanical stresses develop in the constituent materials due primarily to the difference in CTE between the fiber and matrix. At room temperature the tensile residual stresses in the matrix are at a maximum[16]. These stresses have been predicted using a

analytical computer code, FIDEP, which will be discussed later in this chapter. The matrix stresses calculated at the fiber/matrix interface as a function of temperature during the cooldown portion of the consolidation cycle are plotted for the SCS-6/Ti-24Al-11Nb composite in Figure 2. The data predicts that the matrix will undergo plastic deformation, as depicted by effective stress following the yield surface at temperatures below 600°C.

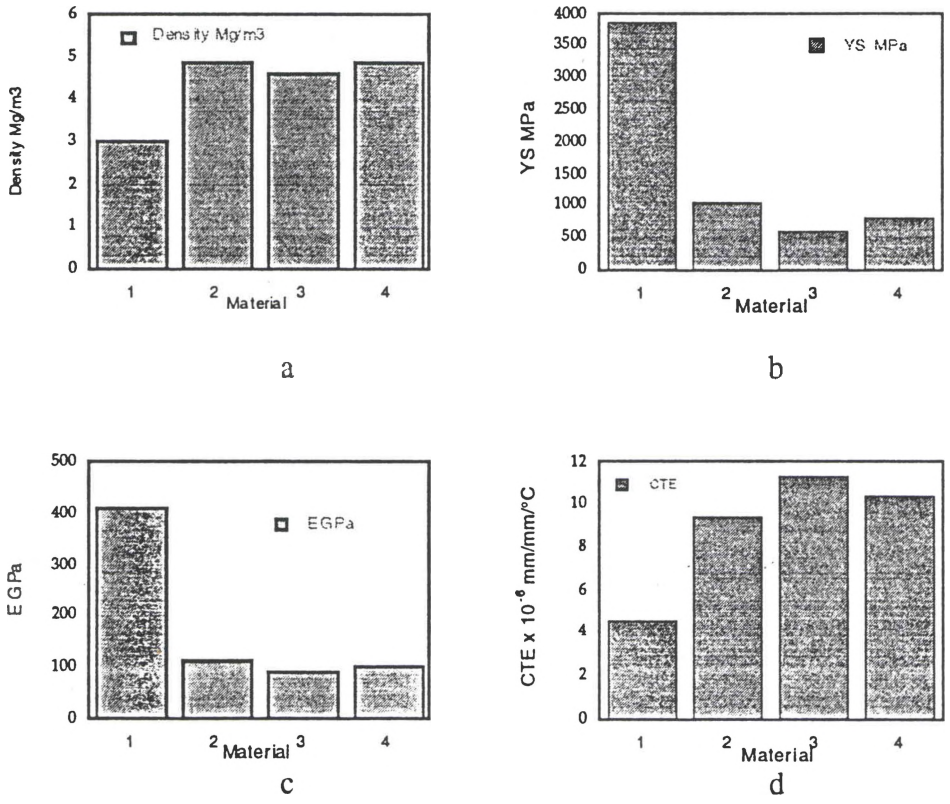

Figure 1. Room temperature properties: a) density b) yield stress (YS) c) elastic modulus and d) coefficient of thermal expansion (CTE) for materials: 1 - SCS-6 fiber; 2 - Timetal-21S; 3 - Ti-24Al-11Nb; and 4 - Ti-23.5Al-16.5Nb.
Density data taken from Larsen, WPAFB; Fiber YS data taken from Spear[19]; Modulus, CTE and Matrix YS data are located in Appendix B.

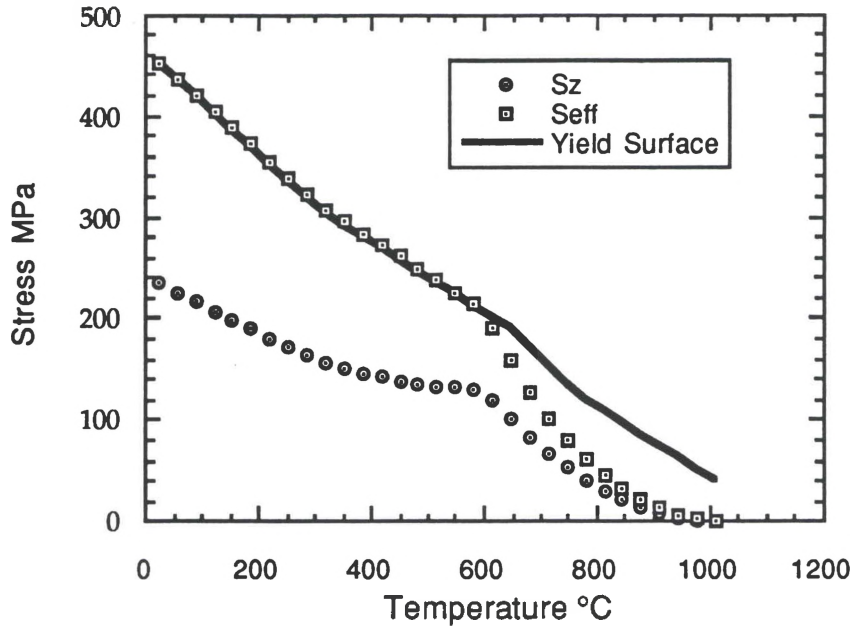

Figure 2. Predicted micromechanical matrix stresses at the fiber/matrix interface during the cooldown from consolidation temperature for SCS-6/Ti-24Al-11Nb. The stresses were output from a computer code, FIDEP, developed by Coker of UDRI.

Subsequent temperature excursions result in a cycling of the thermal stresses within the constituents, and stress gradients in the matrix between the region adjacent to the fiber and the free surface can be significant. The addition of a mechanical load cycle has different effects depending on the phasing with the thermal cycle. Fatigue damage can be initiated through plastic deformation of the matrix caused by thermal, mechanical, or both (thermomechanical) loading conditions, and stress risers, such as voids, inclusions, and fiber/matrix interfaces can invoke plastic deformation even if the mechanically applied stresses are below the bulk matrix's yield level[23]. Even though the fibers provide excellent strength at high temperatures, the composite behavior can be governed by the matrix properties and localized matrix stresses. Therefore, in fatigue and thermomechanical fatigue, the matrix alloy, with its respective properties, can play a major role in influencing the failure mode.

TMF Description

TMF testing is a more recent development than other well established fatigue methodologies. Simulating TMF conditions is necessitated by the realization that actual components experience thermal and mechanical cycling simultaneously. Therefore, TMF characterization of structural materials, especially those involved in the aerospace industry, provides for a better understanding of material behavior in actual service conditions than does the conventional isothermal fatigue (IF). IF tests run at maximum service temperatures have been shown to overestimate lives as compared to TMF conditions, thereby reinforcing the acceptance of TMF for predicting real life component behavior under realistic service conditions[24,25].

A thermomechanical fatigue test is devised to study material damage under varying load/temperature histories. Both the temperature and mechanical load imposed on the specimen are controlled. In the literature two common TMF cycles, representing the extremes in the relationship between load and temperature scenarios, are commonly utilized: in-phase (IP) refers to a condition when temperature and load are cycled coincident with each other, out-of-phase (OOP) refers to the opposite, when temperature and load are cycled 180 degrees apart. Schematics of both conditions are shown in Figures 3 and 4.

During testing of continuous fiber composites, each loading/temperature scenario has an unique effect on the micromechanical stresses of the fiber and matrix. IP conditions, involving maximum applied stress at maximum temperature, have been found to increase the micromechanical stresses, both maximum and range, of the fiber[7,26,27]. OOP conditions, through the combination of the maximum applied mechanical load and maximum thermal residual stresses at minimum temperature, produce the worst case scenario with respect to the matrix. Therefore, OOP TMF is a more severe test of the matrix and the matrix properties' influence on composite fatigue behavior.

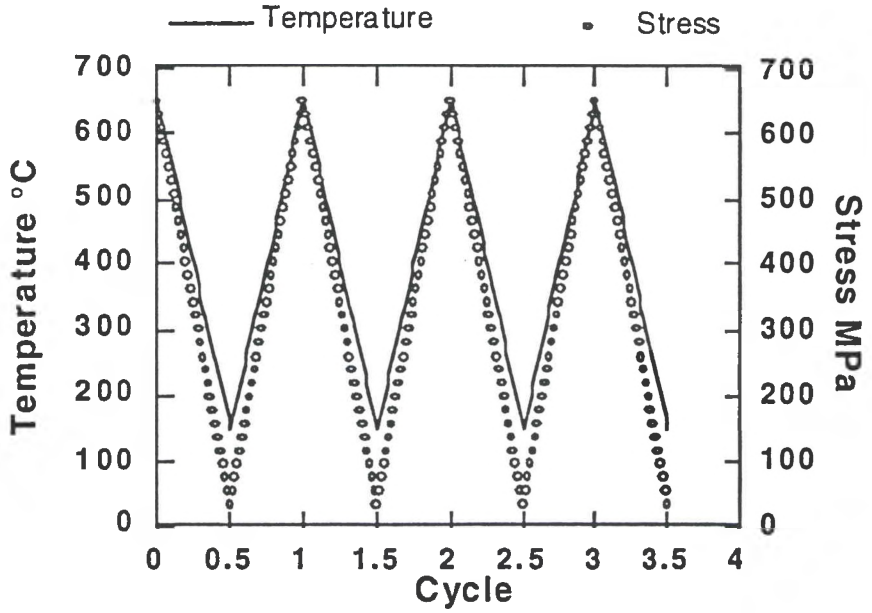

Figure 3. IP TMF cycling for max. stress = 650 MPa, ΔT = 150-650°C, R = 0.05.

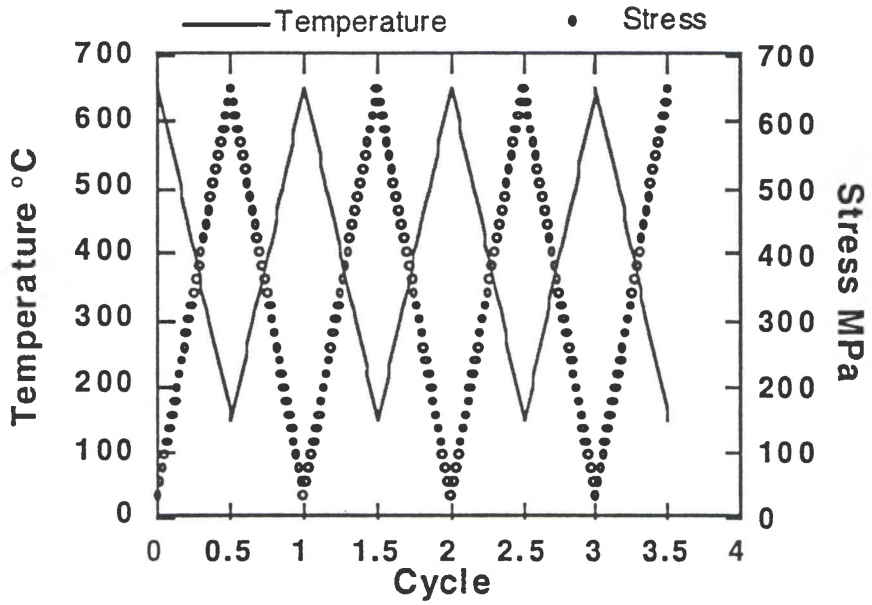

Figure 4. OOP TMF cycling for max. stress = 650 MPa, ΔT= 150-650°C, R= 0.05.

A general description of the concept relating fiber and matrix stresses to OOP loading is best described through aid of the CTE mismatch between the fiber and the matrix. Due to the lower CTE of the fiber compared to the matrix, see Figure 1, at higher temperature the matrix will attempt to expand more than the fiber. Consequently, the fiber experiences tensile stresses and the matrix, compression. When a minimal load is applied to the composite in this condition, the stresses on the fiber and matrix will increase only slightly. At lower temperature, the matrix will attempt to contract more than the fiber resulting with the matrix in tension and the fiber in compression. When the maximum tensile mechanical load is applied to the composite in this condition, the matrix thermal and mechanical stresses will be additive. The tensile mechanical load will act to overcome the thermal compressive stress in the fiber resulting in a relatively benign fiber stress state. Therefore, when the extremes of the OOP cycle are considered, the greater stress range occurs in the matrix. Figure 5 diagrams the micromechanical matrix stresses predicted at the fiber/matrix interface during the first cycle of an OOP TMF test resulting in a matrix effective stress range of approximately 390 MPa.

IP loading will associate opposite effects. Using a micromechanics model, Mirdamadi et. al.[15] found that under IP TMF loading, the peak stress in the fiber is higher than for the OOP loading. Additionally, matrix stresses were found to be higher for the OOP loading than for IP loading. These calculations are consistent with the fact that in the case of IP loading the load carrying capacity of the matrix is greatly reduced at elevated temperatures and the matrix residual stresses are minimal at temperatures above 555°C[16]. Therefore, more load is carried by the fibers than in the case of OOP loading.

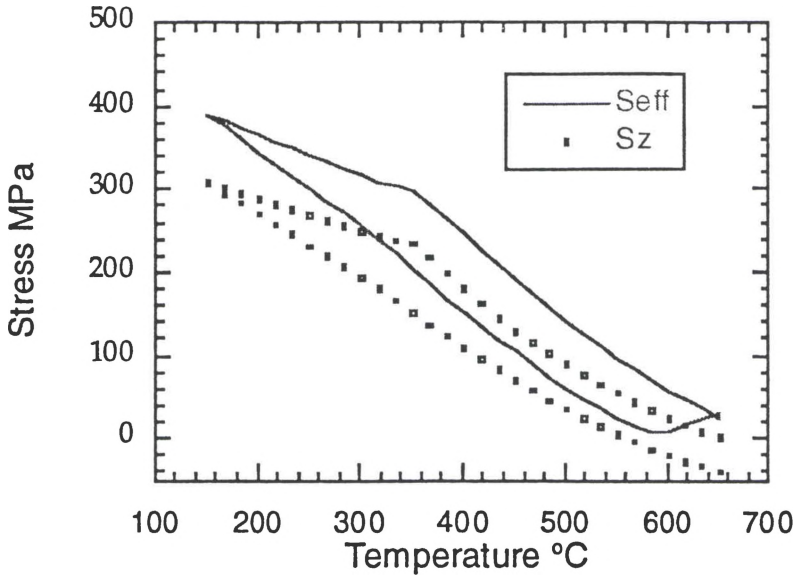

Figure 5. Predicted micromechanical matrix stresses at the fiber/matrix interface for SCS-6/Ti-24Al-11Nb during the first OOP TMF cycle for maximum stress = 500 MPa, ΔT = 150-650°C, R = 0.05. The stresses were output from a computer code, FIDEP, developed by Coker of UDRI.

Although there is a lack of literature on TMF of monolithic titanium alloys, thermomechanical fatigue studies have been performed on other metal alloys where multiple damage mechanisms combined to significantly reduce fatigue lives. Sehitoglu and Boismier[26] found that oxidation damage was the dominant damage mechanism in OOP TMF of a nickel based superalloy. They noted significant surface and crack tip oxidation, where preferential grain boundary environmental attack occurred due to the easier path of oxygen diffusion. In this work, the rate of oxidation was determined to be a function of stress. Additionally, extensive oxide rupturing, both at the surface and crack tips, were discovered for 1070 steel when tested under OOP TMF[24]. In this work, it was concluded that both environmental (oxidation) and creep damage contributed to significantly lower TMF lives as compared to IF.

Numerous studies can be found in the literature on TMF of TMCs. The composite data utilized in this work was limited to SCS-6/Timetal 21S and SCS-6/Ti-

24Al-11Nb. OOP TMF studies involving the composite systems mentioned have identified the matrix dominated phenomenon through fractographic analysis and life prediction modeling[7,17]. Life prediction is discussed later in this chapter and the following discussion will describe the matrix dominated failure.

Failures observed in the SCS-6/Ti-24Al-11Nb(at%) composite under OOP TMF conditions have involved extensive matrix cracking initiating primarily at the surface and edges of specimens[7]. The matrix in the overload region displayed a granular appearance and lack of dimpling indicating failure occurred at the lower temperature (150°C), when the matrix exhibits less ductility. There was also a lack of fiber pull-out. Therefore, it was speculated that the fibers failed in the crack plane as the crack tip progressed through the composite and fiber bridging did not occur. In SCS-6/Timetal 21S, damage during OOP TMF was attributed to matrix cracks which initiated at the surface and were assisted by the environment[17]. The matrix in the overload region displayed dimpling, indicating a ductile tensile failure. In other OOP TMF studies, metallography has revealed extensive matrix damage and minimal fiber cracking[16]. OOP tests have also resulted in significant stiffness losses prior to failure as a result of the environmentally-assisted cracking[28,29].

Damage Mechanisms in TMF

Potentially, several damage mechanisms can operate under thermomechanical fatigue conditions as a result of the mechanical load cycling, thermal cycling, and elevated temperature exposure. The following discussion is intended to include a general overview of the potential damage characteristics which may be evidenced in OOP TMF.

Fatigue

A macroscopic examination of many service failures resulting from cyclic loading reveal distinct fracture surface markings[30]. The fracture surface is generally flat

indicating the absence of an appreciable amount of gross plastic deformation. In many cases, particularly failures occurring over a long period of time, the fracture surface contains lines referred to in the literature as "clam shell markings", arrest lines, and/or "beach markings", which are assumed to be attributed to different periods of crack extension. These markings often are curved, with the center of curvature being at the origin, and therefore serve as a useful guide to direct the investigator to the point of crack initiation. Also, the alternate crack growth and dormant periods cause regions on the fracture surface to be oxidized and/or corroded by differing amounts, resulting in the formation of a fracture surface containing concentric rings of non uniform color.

Initiation, one of the most intriguing aspects of fatigue, can be explained through substructural changes experienced during cyclic loading. The cyclic strains induced by cyclic stresses produce surface offsets, such as intrusions and extrusions which represent the initial stage of microcrack formation. These surface offsets represent the free surface terminations of dense bands of highly localized slip, the predominant mode of plastic deformation in titanium. Slip occurs when a force great enough to break all atomic bonds along a plane, referred to as a slip plane, is applied. The bonds holding the plane together are the first to yield and deformation occurs by slipping between adjacent planes. The stress necessary to induce slip may be reduced by defects, termed dislocations, which define the border between slipped and unslipped regions. During cycling a surface layer of high dislocation density may be formed and the stress concentration associated with this dislocation pileup is then thought to trigger the development of a crack.

Cracks are therefore believed to be the result of stress concentrations at the slip band interactions and usually occur at heterogeneous nucleation sites within the material, whether they be preexistent, such as inclusions, gas pores or local soft spots in the microstructure, or generated during the cyclic straining process itself. As the severity of a design imposed stress concentration and/or the applied stress increases, the number of nucleation sites increase. Therefore, the number of initiation sites is a function of stress

state, material, and design. Crack growth occurs by localized deformation and slip in the cyclic plastic zone ahead of the crack tip. The size of the fatigue crack at the point of final failure is directly related to the applied stress level and the fracture toughness of the material.

Fracture in the overload region is governed by one of two main failure mechanisms, dimpling or cleavage. Ductile fractures from tensile overload of homogeneous materials are typically characterized by high strains-to-failure associated with plastic behavior. Ductile failure is characterized by dimpling associated with the commonly observed stages of void formation, growth, and coalescence. Specifically, these stages of ductile failure include the formation of a free surface at an inclusion or second phase particle by either interface decohesion or particle cracking, growth of the void around the particle, by means of plastic strain and hydrostatic stress, and coalescence of the growing void with adjacent voids[31]. Cleavage, on the other hand, is a brittle-type fracture where minimal strains-to-failure are usually experienced, and the material mainly exhibits elastic behavior. Cleavage fracture can be defined as rapid propagation of a crack along a particular crystallographic plane. The preferred cleavage planes are those associated with the lowest energy, such as the planes with the lowest packing density, since fewer bonds must be broken and the spacing between planes is greater. The fracture path of these cleavage planes is typically transgranular. For example, the propagating crack changes direction each time it crosses a grain boundary, where the crack seeks the most favorably oriented cleavage plane in each grain. The normal orientation of the cleavage crack is typically perpendicular to the maximum principal stress. Hexagonal close packed (HCP) metals, such as alpha phase titanium, are susceptible to cleavage because there are not ample slip systems to provide ductile behavior. The slip modes in beta phase titanium are expected to be the same for BCC metals, which provide additional slip systems for structures to undergo ductile fracture[18].

Oxidation

Oxidation damage mechanisms include crack nucleation in surface oxides and oxide-induced crack growth. Crack nucleation can be defined as the rupture of the first surface oxide layer while oxide-induced crack growth is described as the repeated formation of an oxide layer at the crack tip and its rupture, exposing fresh metallic material to the environment. Nucleation, therefore, is a one-time event associated with initiation, while oxide-induced crack growth occurs continuously thereafter. Crack nucleation under TMF can be described through a series of occurrences. Depending on the alloy, at elevated temperature oxygen diffuses into the material which leads to the formation of an oxygen embrittled region and oxide formation at the surface. The surface oxide experiences a mechanical stress which can result from either the applied mechanical loading, CTE mismatch between the oxide and the substrate, the relative creep behavior between the oxide and the substrate, geometry effects, or a combination of these[24]. Because oxygen is an alpha phase stabilizer, oxygen diffusion results in precipitation of the brittle alpha phase[32]. A tensile mechanical loading in the oxide above some critical stress will cause the brittle oxide to fracture. Tensile oxide fracture can then lead to crack nucleation of the base metal. Exposure of the crack tip to an oxidative environment causes additional precipitation of the alpha phase and reduced fracture properties.

Thermal cycling is inherent in TMF testing and provides an example of detrimental oxidation effects. Thermal cycling relaxes the residual stresses as the composite is heated and increases residual stresses upon cooling. The cyclic constituent stresses can lead to matrix and interface damage even without applied mechanical loading. During thermal cycling in air, the exposure to oxygen as the temperature increases leads to the oxidation damage previously mentioned, where oxygen embrittlement, and its associated degradation, continues with each thermal cycle and thus accounts for the cyclic dependence of strength loss[33]. Russ[10] found severe loss of

strength of SCS-6/Ti-24Al-11Nb(at%) when thermally cycled with no load in air from 150-815°C after only 100 cycles. Revelos and Smith[1] demonstrated the importance of oxidation during thermal fatigue of this composite system. Severe cracking and loss of strength were observed in experiments performed in air, where no damage was observed under the same conditions in an inert environment. Additionally, Revelos et. al.[32] found that thermally cycling Timetal 21S composites causes a microstructural change where the alpha phase precipitates out of the beta phase at oxygen effected zones. These studies and others[16,28,34] demonstrate the potential severity of thermally cycling TMCs.

Creep

Creep, a diffusion controlled phenomenon, can be described to occur in stages. Stage 1, primary creep, represents the onset of the test when strain increases rapidly. This stage typically associates substructure changes that increase the overall resistance of the material to dislocation motion. Stage 2, secondary creep, represents the relatively constant strain rate experienced over a majority of life and is associated with microstructural stability. Characteristic of this stage is the extensive formation of dislocation pileups at obstacles such as grain boundaries and free surfaces. Stage 3, tertiary creep, occurs just prior to failure and involves weakening metallurgical instabilities such as localized necking, microvoid formation, and/or precipitation of brittle second phase particles. The damage mechanisms that indicate creep-induced damage and creep-fatigue interactions include: coalescence of intergranular voids ahead of an advancing crack, a greater crack tip plastic zone resulting from the summation of the plastic zones of voids ahead of a crack, grain boundary sliding initiation wedge-type cracks at grain boundaries, grain boundaries acting as weak paths for flow localization and crack growth, and combinations of these[24].

The OOP TMF condition involves high stresses at "cold" temperatures and low stresses at "hot" temperatures which is not as conducive to creep-ratcheting effects as is IP TMF, which involves high stresses at "hot" temperatures and low stresses at "cold" temperatures. Correspondingly, IP TMF has been found to produce more creep ratcheting than OOP TMF[35]. However, a low frequency and corresponding slow strain rate may produce creep effects in load control OOP TMF as well.

Wright[36] showed that creep is sensitive to the matrix microstructure and although the strong fibers reduce creep and allow matrix relaxation, longitudinal creep rates are ultimately controlled by matrix properties. Khobaib[3] found that creep damage in SCS-6/Ti-24Al-11Nb(at%) was linked to multiple initiation sites, in most cases at surface flaws, such as a cut fiber or oxygen embrittled matrix, followed by a dominant crack that led to final fracture. The fracture surfaces of that work exhibited an oxidized zone with a relatively flat surface representing the time dependent slow growth region, while the adjacent zone, dominated by fiber pull-out, was indicative of an overload fracture. It was concluded that stress-assisted environmental degradation played a major role in the failure of the composite. A TEM study showed slip bands in the matrix and dislocation pileups against the fiber/matrix reaction zone for creep specimens at 650°C and an applied stress of 345 MPa[9]. Therefore, it was concluded that the reaction zone was serving as a barrier to dislocation movement. Similar creep failure modes have been discovered for the SCS-6/Timetal 21S composite, where matrix cracking near edges progressed the depth of two fiber diameters, or approximately 300 micrometers, into the specimens[37].

It is summarized that degradation occurs in the form of matrix cracking, as a result of fatigue and/or creep, ultimately leading to failure. This degradation is enhanced by environmental attack. Surface cracking was common to each study mentioned, where crack initiation is suggested to occur at or near surface locations. Therefore, initiation and growth of cracks within composite matrices are important in OOP TMF.

Life Correlation

In the literature, life prediction models have been developed for TMF of composites based on observed damage mechanisms. Russ et al.[7] proposed a model where a fraction of the fatigue life is attributed to fiber and matrix dominated terms and the sum of these individual damage terms are combined to predict failure according to the following equation:

$$N/N_f + N/N_m = 1$$

where N is the total cycles-to-failure, and N_m and N_f are the portion of life contributed to the composite by the matrix and fiber dominated conditions; respectively. N_f was found to dominate the IP TMF condition while N_m was found to dominate the OOP conditions. N_m was determined to be a function of the stress range in the matrix as calculated from the micromechanical code, FIDEP, described in the next section. The relationship is of power law form:

$$N_m = B(\Delta\sigma)^{-n}$$

where σ is the matrix stress and B and n are empirical constants determined by trial and error using the experimental test data. This model was used to fit IP and OOP TMF as well as isothermal and thermal fatigue data for the SCS-6/Ti-24Al-11Nb(at%) composite. It was further adopted for an SCS-6/Timetal 21S $[0/90]_{2S}$ composite by Hanson[13] and Mall et. al.[14].

Other life prediction TMF models have been based on microstructural observations where damage was considered to be caused by fatigue, environmental oxidation, and creep according to[16,38]:

$$D^{tot} = D^{fat} + D^{ox} + D^{creep}$$

where D^{tot} is the total damage done to the composite, and D^{fat}, D^{ox}, and D^{creep} are the damage resulting from fatigue, oxidation, and creep; respectively. The corresponding life equation entailed each damage mechanism's contribution to the failure of the composite,

where the term which contributed the most damage to the composite in each strain-temperature phasing was considered the dominant damage mechanism.

Micromechanical Model

In the literature, there are numerous models predicting the micromechanical stress/strain state of composites using a variety of theories and assumptions[35,39-41]. FIDEP, a Finite Difference Code for Elastic-Plastic Analysis of Composites, was used in this work to predict the micromechanical stresses of the fibers and matrices. The code, developed by Coker[42], is based on a concentric cylinder approximation of composite behavior where the fiber is treated as elastic and the matrix material behavior is represented as elastic-plastic with linear strain hardening. The yield stress, elastic and plastic moduli, poisson's ratio, and CTE of the matrix and fiber are all represented as a function of temperature. The output includes axial, radial, tangential, and effective stresses at the fiber/matrix interface and, at specified times within the cycle, the various stresses as a function of radial location. Results from FIDEP have shown good correlation to experimental work[7].

FIDEP was developed using the following assumptions:

1) The temperature distribution is uniform and quasi-static.

2) A perfect bond exists between the constituents of the composite so that there is no slippage or separation of the constituents.

3) The concentric cylinders are in generalized plane strain and are subjected to axisymmetric loadings and displacements so that the shear stresses are zero.

4) The constituent properties are isotropic.

5) The fiber is linearly elastic.

6) The matrix follows a Von Mises yield surface and is incompressible in the plastic region.

7) Hydrostatic stresses do not cause plastic deformation.

8) Plastic deformation of the matrix is governed by the Prandtl-Reuss flow rule.

9) Boundary conditions include continuous radial displacements and radial stresses at the interface and finite radial stresses at the surface of the concentric cylinder and at the center of the fiber.

Specifically, FIDEP employs assumptions specific to titanium alloys with regard to temperature dependency including:

10) Titanium matrix properties are assumed constant from room temperature to 150°C.

11) Titanium matrices exhibit thermoviscoplastic behavior above 480°C[15].

A typical product of a FIDEP calculation is plotted in Figure 6 for the SCS-6/Timetal 21S composite at 150°C and 600 MPa after simulating three OOP TMF cycles. Both effective stress, Seff, and axial stress, Sz, are plotted as a function of radial location, where R is the distance from the center of the fiber and B represents the free surface of the concentric cylinder model, or the point farthest away from the center of the fiber. The discontinuity at R/B of 0.62 identifies the fiber/matrix interface. Effective stress is calculated from the axial, radial, and tangential stress components using the Von Mises stress criterion, defined in Appendix A. For this particular case the matrix has not experienced any plastic deformation, identified by the horizontal nature of the axial stress and the continual decline of the effective stress. Similar plots for the other composite OOP TMF simulations can be found in Appendix A.

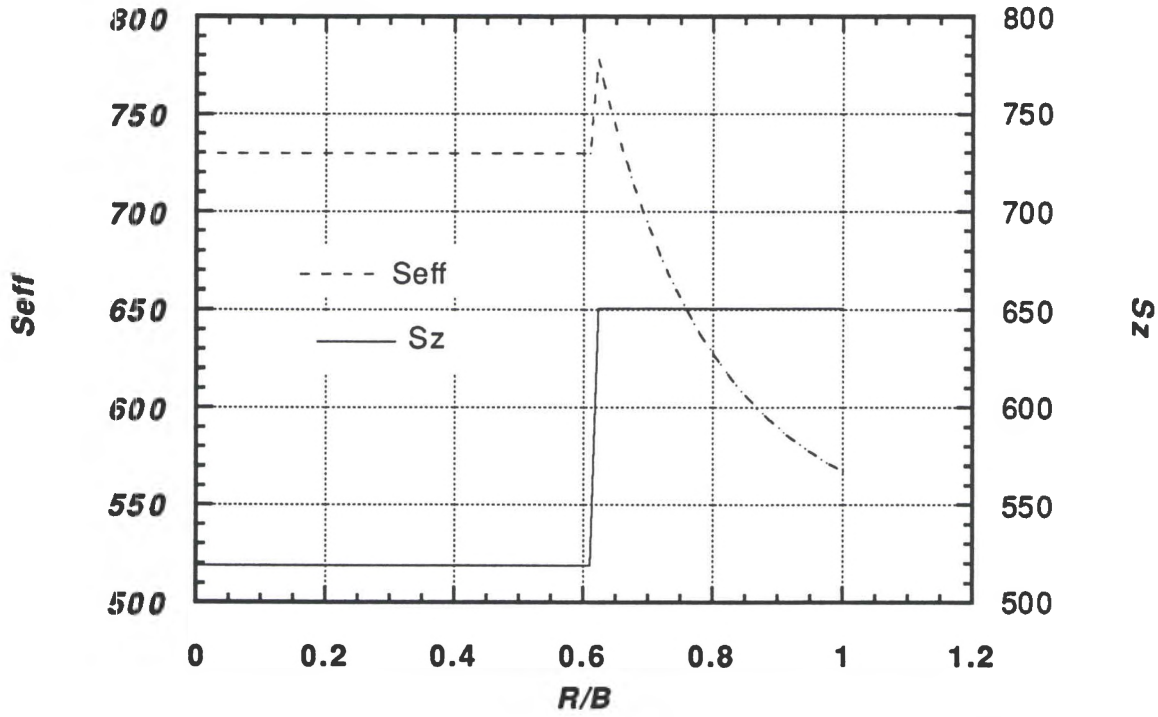

Figure 6. Stresses of the fiber and matrix along a cross-section of the SCS-6/Timetal 21S composite at 150°C and 600 MPa of an OOP TMF cycle as calculated using FIDEP.

CHAPTER II

TEST MATERIALS

Timetal 21S

Timetal 21S (Ti-15Mo-2.6Nb-3Al-0.2Si(wt%)) is a metastable beta titanium alloy with oxidation resistance comparable to alpha-2 alloys and far exceeding other beta alloys, which can mainly be attributed to the high molybdenum content[43]. With the development of a microstructurally stabilizing heat treatment, where a fine dispersion of acicular alpha phase precipitated within the prior beta grains and along the grain boundaries, Timetal 21S has exceeded the strength and ductility of many other beta titanium alloys[11]. The effectiveness of this aging treatment can mainly be attributed to the precipitation of the fine and strong alpha phase. As the volume fraction of alpha phase increases during the hold at 620°C (below the beta transus temperature of 780°C) for 8 hours, beta stabilizers diffuse from the alpha into the surrounding beta phase. The increased concentration of beta stabilizers suppresses the formation of the brittle omega phase in the remaining beta phase. The alpha phase within the prior beta grains consumes more than 50% of the total volume fraction after the subsequent cool down to room temperature. This results in a unique combination of both strength, attributed to the alpha phase, and ductility, attributed to the beta phase. Figures 7 and 8 illustrate the microstructures of Timetal 21S both before and after heat treatment.

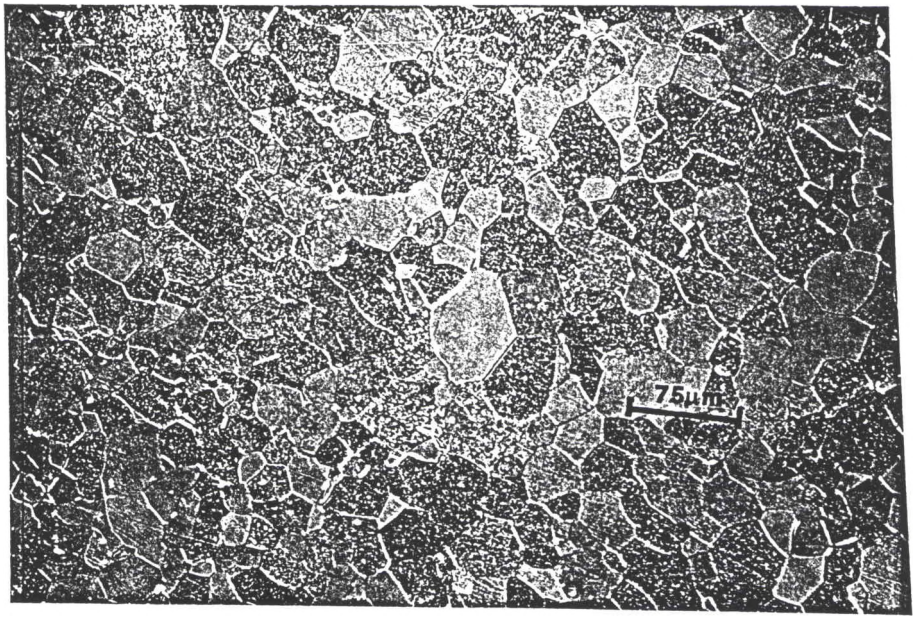

Figure 7. Timetal 21S in the as-processed condition (200X).

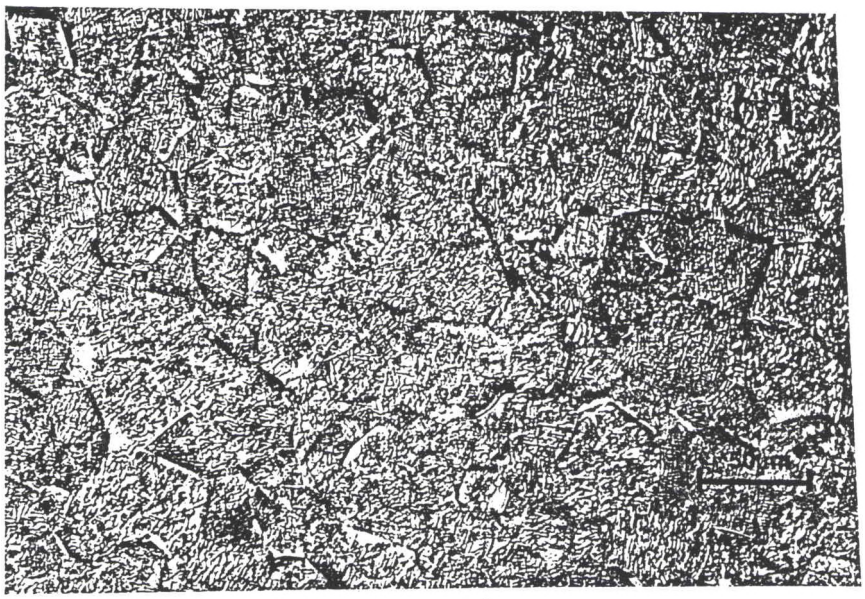

Figure 8. Timetal 21S after heat treatment (300X).

Ti-24Al-11Nb

Ti-24Al-11Nb(at%) is composed of both an ordered hexagonal alpha-2 phase, Ti_3Al, and a beta phase, which can be either ordered ($ß_2$) or disordered (ß). Figure 9 represents the fine alpha-2 dominated microstructure of Ti-24Al-11Nb. In monolithic form this material possesses high specific strength and stiffness at temperatures up to 650°C, and when combined with ceramic fibers, there is a significant enhancement of these properties. However, due to the brittle nature of the alpha-2 phase, Ti-24Al-11Nb suffers from environmental embrittlement when exposed in an air environment at high temperatures and has been unable to achieve the desired balance of properties acceptable for the 630-750°C aerospace applications[44]. The environmental damage can mainly be attributed to oxygen, an alpha stabilizer, which further reduces the ductility[45]. Additionally, characteristic of alpha-2 composite systems, the matrix is depleted of the ductile/toughening beta phase at locations near the fiber/matrix interface, and the reaction zone between the fiber and the matrix contains brittle carbides and silicides[44].

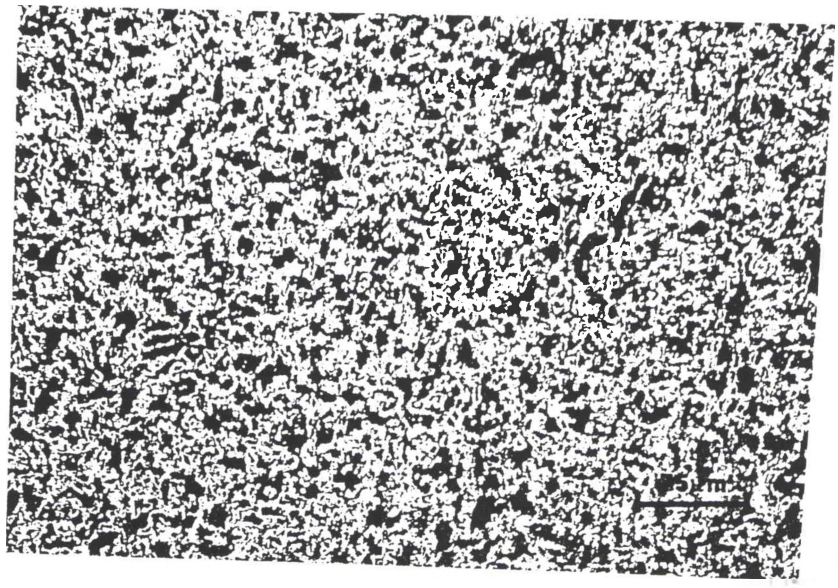

Figure 9. Ti-24Al-11Nb in the as-processed condition (200X).

Ti-23.5Al-16.5Nb

Similar to Timetal 21S, the orthorhombic phase tifanium alloy is one of the most recent to be evaluated as a possible matrix alloy for elevated temperature aerospace applications. The orthorhombic alloy, Ti-22Al-23Nb(at%), comprises a three phase microstructure of alpha-2, an ordered beta phase (β_2), and an ordered orthorhombic phase (Ti_2AlNb). For simplicity, this alloy is termed "orthorhombic" due to the large volume fraction of this phase and its potential impact on the mechanical properties of this material. Ti-23.5Al-16.5Nb(at%) is considered "near-orthorhombic" due to the smaller volume fraction of the orthorhombic phase. Figures 10 and 11 identify the general microstructure of Ti-23.5Al-16.5Nb. As compared to alpha-2 alloys, this class has been shown to be stronger and stiffer and more thermomechanically processable[12,44,46]. TEM analysis of neat panels (panels without fibers) has indicated a two-phase microstructure at the foil surface comprised primarily of an ordered beta phase with orthorhombic phase lath precipitates dispersed throughout[47]. This two-phase mixture is likely to provide a relatively ductile/low strength zone at the surface and in the areas adjacent to the fiber/matrix interface. It has been postulated that based on the slower diffusion kinetics and reduced oxide scale formation and greater fracture toughness associated with the orthorhombic system, these alloys should outperform the alpha and alpha-2 classes under thermomechanical conditions at temperatures up to 630°C[44]. Additionally, orthorhombic composites have shown no beta depleted zone at or near the fiber/matrix interface[19,43,44].

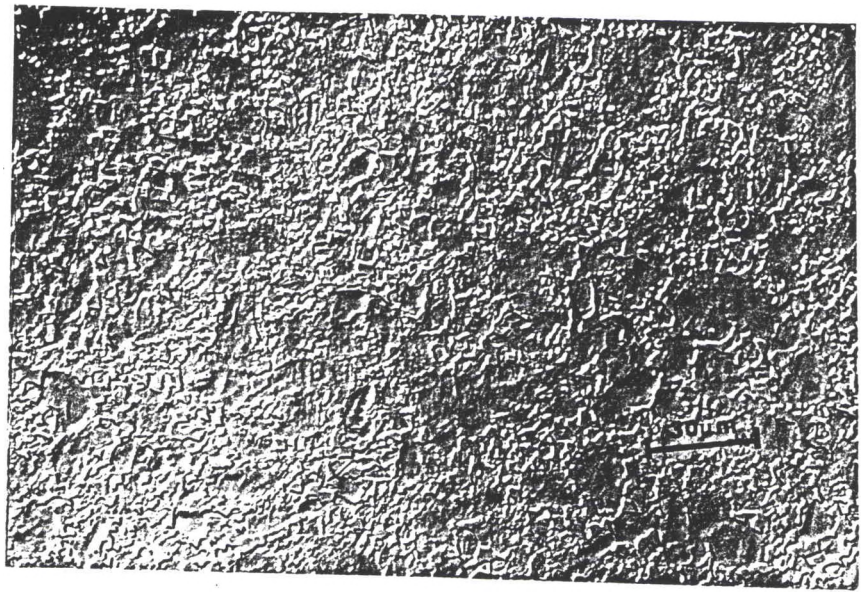

Figure 10. Rolled surface of Ti-23.5Al-16.5Nb in the as-processed condition (500X).

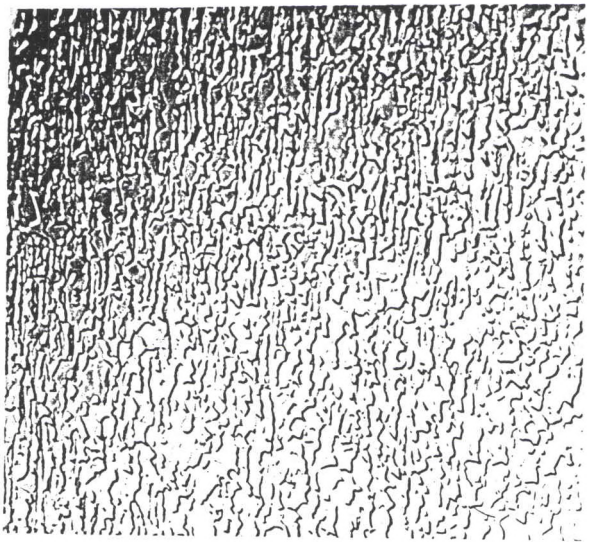

Figure 11. Transverse sample of cross-rolled Ti-23.5Al-16.5Nb (500X).

CHAPTER III

EXPERIMENTAL EQUIPMENT AND PROCEDURE

In order to evaluate the effects of OOP TMF on beta, alpha-2, and near-orthorhombic titanium alloys, rectangular specimens were subjected to thermomechanical cycling on an automated test system. The purpose of this chapter, which is divided into three parts; samples, equipment, and procedures, is to discuss the methodology and reasoning used for the testing of these alloys.

Samples

The materials used in this thesis came from monolithic sheets produced by TIMET. Ingots of the composition listed in Table 1 were forged to 50.8 mm by 152.4 mm by 304.8 mm slabs. The slabs were then rolled unidirectionally at above the beta transus temperature. Timetal 21S was unidirectionally rolled while Ti-24Al-11Nb and Ti-23.5Al-16.5Nb were cross-rolled. The sheet product was nominally 2 mm thick. It should be noted that because the Timetal 21S specimens had a preferentially rolled direction, close attention was paid to the machining and testing alignments so that the specimens were tested in the rolling direction. Initially, 3 mm was cut off the edges of the sheets to remove edge defects. Specimens were machined using a 0.914 mm diamond saw. The Timetal 21S specimens measured 127 mm by 10.16 mm, while the Ti-23.5Al-16.5Nb and Ti-24Al-11Nb specimens measured 114.5 mm by 7.62 mm. The Timetal 21S and Ti-23.5Al-16.5Nb sheets contained visible surface irregularities and those specimens were polished using 240, 320, 400, and 600 grit silicon carbide paper; respectively, to

remove potentially significant stress concentrations. The Ti-24Al-11Nb sheet was uniformly flat and consequently, those specimens were not polished. Before testing, all specimens were ultrasonically cleaned in acetone for five minutes to remove contaminates from the surface.

Table 1 Chemical Analysis in weight percent

Material	Ti	Al	Nb	Fe	O	N	Mo	Si
Timetal 21S	Bal	3.0	2.6				15	0.2
Ti-24Al-11Nb	Bal	13.9	20.9	.045	.095			
Ti-23.5Al-16.5Nb	Bal	12.6	30.4	.048	.082	.009		

Tensile properties for each material were determined previously at various temperatures and are presented in Appendix B. The tensile properties as a function of temperature were required as input to the micromechanics model discussed in Chapter II.

Prior to testing, Timetal 21S samples were subjected to a heat treatment previously developed and used on the SCS-6/Timetal 21S composite[11]. The aging heat treatment involved an 8 hour hold at 620°C in vacuum. Due to lack of experience and literature on the heat treatment of orthorhombic composites at the time of testing, the Ti-23.5-16.5Nb specimens were tested in the as-processed condition. The Ti-24Al-11Nb samples were also tested in the as-processed condition.

Equipment

The test equipment employed for this study was specially designed at Wright Laboratory's Materials Directorate in conjunction with the University of Dayton Research Institute (UDRI) to perform elevated temperature and thermomechanical fatigue testing of metals and metal and ceramic matrix composites[48]. The test apparatus is made up of three major components; test frame, control unit, and personal computer (PC). The testing utilized all three components. A photograph of the test system is provided in Figure 12.

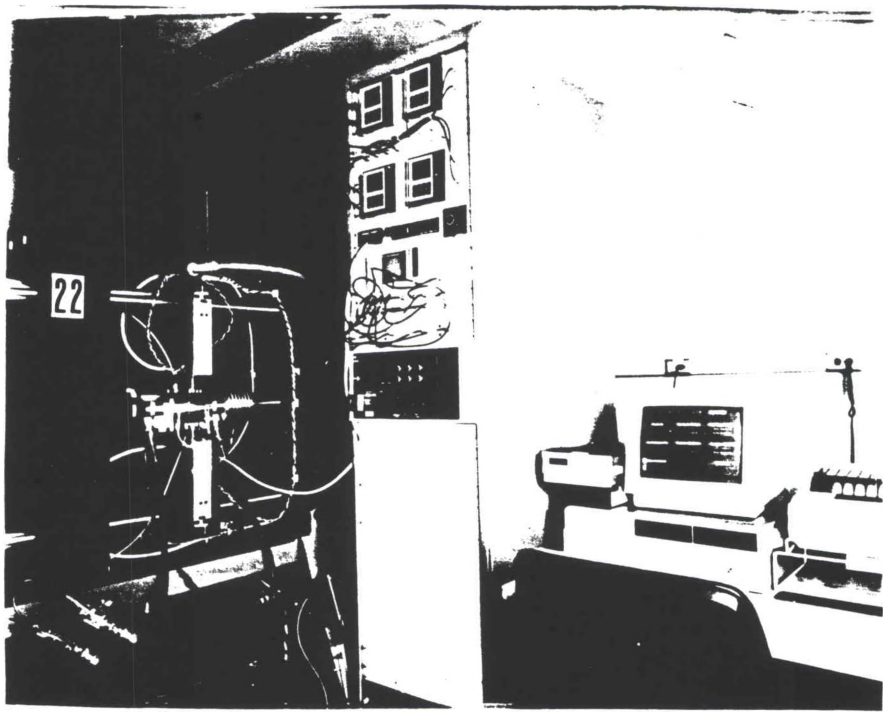

Figure 12. Test system

Test Frame

The load was controlled by a horizontal test frame using an MTS servohydraulic load actuator. The mechanical assembly consisted of a load control unit equipped with a load cell to measure the magnitude of the load. The test frame has a capacity of 25 kN.

Hydraulic friction grips were used to affix the specimen. Due to the uniaxial tension-tension nature of the OOP TMF tests, the primary function of the gripping system was to secure the specimen without inducing bending moments during the loading process. To help minimize bending, the grips incorporated precisely machined outer surfaces which were used to obtain transverse alignment to better than 0.025 mm and angular alignment to better than 0.0002 radians[48]. The grips were found to produce less than three percent bending for a variety of materials during evaluation tests[49]. The grip assemblies were actively cooled due to the high temperature involved in the TMF test. This was accomplished by pumping a water/anti-freeze mixture through cooling

channels drilled in the grips and then passing the coolant through a heat exchanger. The grip assembly is illustrated in Figure 13.

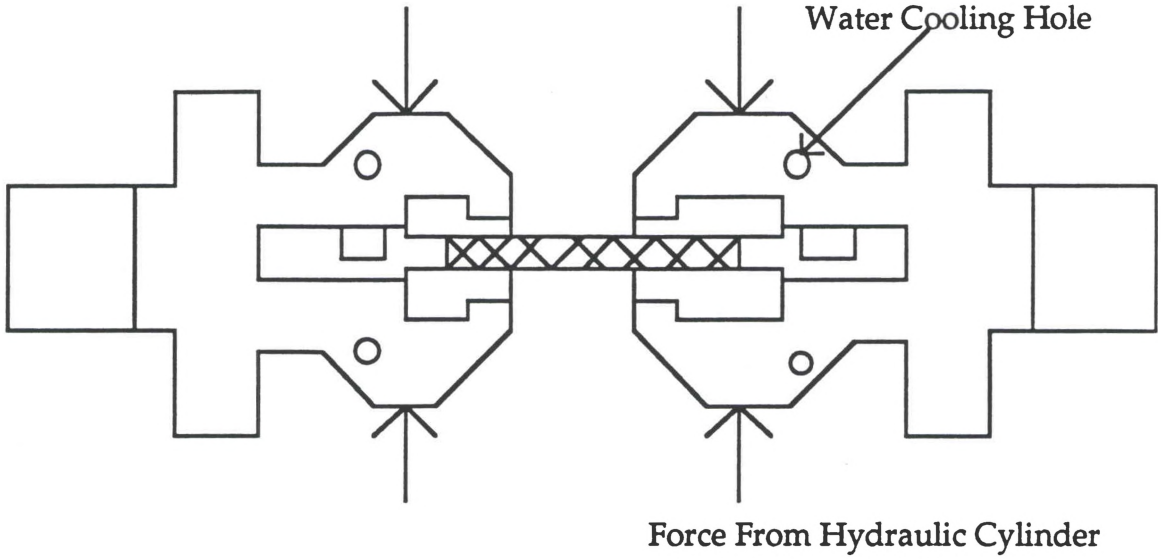

Figure 13. Grip/specimen system

Heating Unit

Thermal control of the test sample was provided by radiant energy heat lamps controlled by Barber Colman process control equipment. The lamps were designed fo' closed-loop (feedback) control of four zones, or areas, of a particular specimen. There was the capacity to monitor an additional 6 locations to assist in temperature/area mapping. Major components of the thermal control system include: two banks of four quartz lamp heaters, forced convection air-cooling of both the lamp cavity and open-air specimen, and a water/anti-freeze cooling system for the lamp bodies.

Radiant energy heating units were used because of their relatively quick and reliable response to evenly heat the test section in a controllable fashion[48]. Heating was applied using the two banks of quartz lamps, symmetrically located approximately 10 mm above and below the specimen. The completed lamp assembly contained four heating zones corresponding to thermocouple locations on the test specimen as depicted in Figure 14.

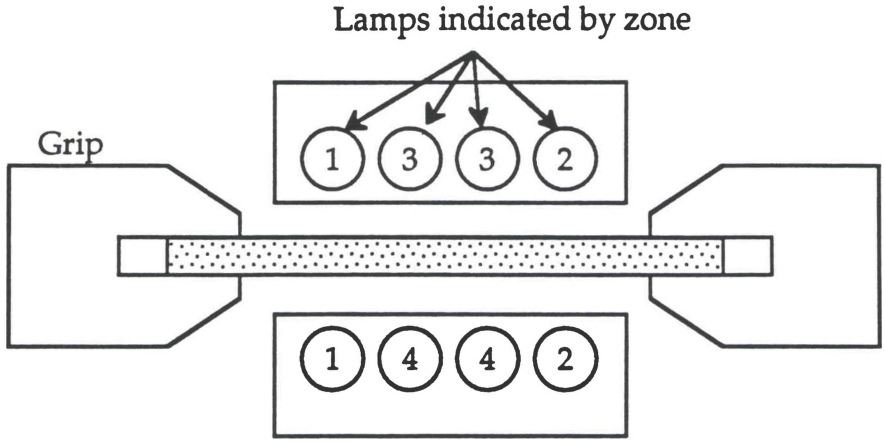

Figure 14. Side view of temperature zones.

Computer Controller

The core of the computer automated test equipment is a PC equipped with a National Instruments interface board and software specially designed to perform TMF testing. The software and component architecture were designed by George Hartman of UDRI. A block diagram of the computer system which controls the mechanical and thermal cycling is diagrammed in Figure 15. The combination of the interface board and software allows the user to program the MTS signal generator and Barber Colman to run a multitude of linearly ramped thermomechanical load control fatigue tests. The user enters test parameters including specimen thickness and width, maximum and minimum cycle temperature, waveform, load ratio, phase angle, cycle and hold times, maximum stress, etc. through a series of interactive menus. The program then sends tailored messages to the Barber Colman and MTS control units in order to perform the desired profile. The OOP stress/temperature profile used is plotted in Figure 4.

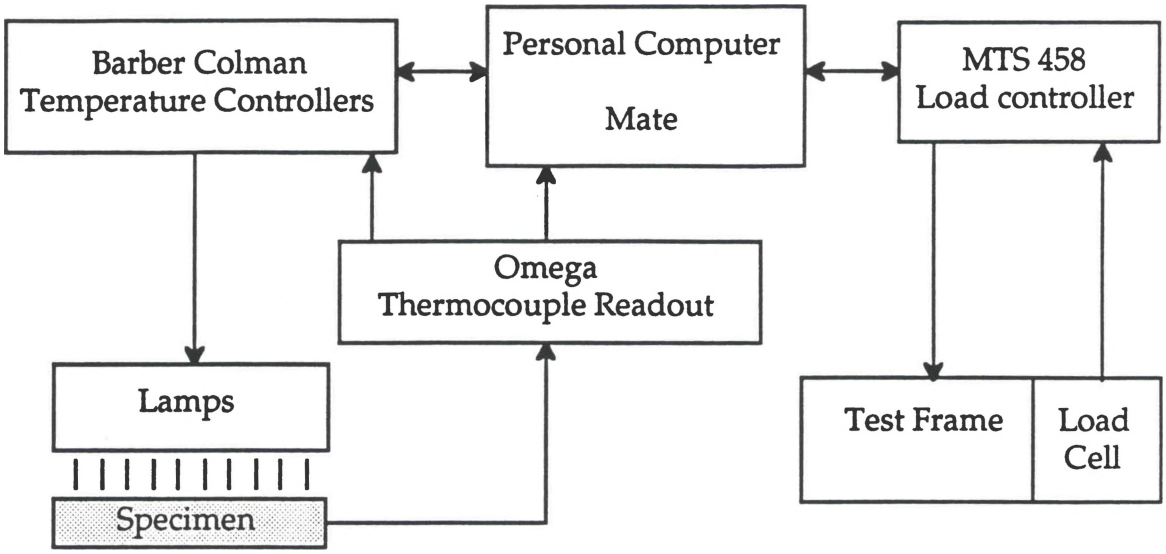

Figure 15. Computer controller block diagram

Throughout the test, the PC monitors load, displacement, and temperature values from the load cell, extensometer, and thermocouples; respectively. If discrepancies exist between the load and temperature values in reference to the requested profile, updates are performed and relayed to the waveform generator. For example, if the actual maximum temperature for a data acquisition cycle (DAC) is lower or higher than the requested temperature, the PC will update the profile accordingly.

The phasing of the load and temperature profiles is a critical parameter in OOP TMF testing. The approach taken to offset phase angle errors was to incorporate subtle shifts in the load cycle. During each data acquisition cycle, the program compared selected points, Load and Temperature Phase Break Points (LPBP and TPBP; respectively), in the load and temperature waveforms to ascertain the phase angle error. With the triangular waveforms, the best response (i.e. lowest phase angle errors) were ascertained when the LPBP and TPBP were addressed at the respective maximum values.

Extensometers

Two extensometers were used in the course of the TMF testing. The Timetal 21S specimens employed a 25.4 mm gage length MTS high temperature extensometer, fitted with 5 mm conic point ceramic rods. Because of the decreased gage length incorporated with the Ti-24Al-11Nb and Ti-23.5-16.5Nb specimens, a result of the decreased temperature/area control involved with the unique set up which is described in the next section, the same extensometer could not be used. Instead a 12.7 mm MTS high temperature extensometer with alumina silica ceramic rods was employed. The strain data stored in the data files was calculated from the displacement measured by these high temperature extensometers.

Procedures

Previous tests using directly welded thermocouples have proven to be the most reliable means of acquiring accurate temperature readings for MMCs[2,6,7,17,48,49]. However, thermocouple induced surface flaws proved to be detrimental to two of the monolithic alloys examined. This was not the case for Timetal 21S. Due to the tolerance to cracking and multiple initiation sites characteristic of the Timetal 21S specimens, it was determined that thermocouple induced cracking did not significantly affect fatigue life. Therefore, the 36 gauge type K thermocouples were welded directly onto the specimen surface in order to monitor the specimen's temperature. The temperatures were relayed to the Barber Colman to complete the temperature feedback control loop.

"Dummy" Set Up

For the Ti-24Al-11Nb and Ti-23.5Al-16.5Nb monolithic specimens, directly welding thermocouples to the specimen surface was not practical. The initial tests using directly welded thermocouples resulted in premature failure resulting from cracking initiated at thermocouple locations, as illustrated by the fracture surface in Figure 16.

The fracture properties of these materials, as opposed to Timetal 21S, necessitated an alternative method of temperature monitoring. The successful alternative method utilized a "dummy" specimen, machined from the same sheet as the test specimen. The "dummy" specimen was positioned parallel to the test specimen and instrumented for temperature control. The "dummy", half as wide and shorter than the test specimen, was only inserted into one grip and therefore carried zero load. To demonstrate, 6 thermocouples were placed on a demonstration specimen, while the four controlling thermocouples were placed on the "dummy" as shown in a top view of the "dummy" test setup, Figure 17. In order to obtain adequate temperature control of the test specimen, a regular OOP TMF test was performed with a maximum stress level of 50 MPa, and the temperature gradient of the demonstration specimen was mapped. Appendix C presents the temperature profiles of the successful trials. It was assumed that temperature gradients would not change after cycling for more than 500+ cycles due to the repetitive cycling involved with the OOP TMF test. Machine parameters such as convective airflow volume and alignment, "dummy" spacing, thermocouple placement, lamp spacing, etc. remained unchanged until the completion of each alloy's testing in order to provide similar temperature profiles on the loaded specimens. A check of the temperature mapping was performed during the testing of Ti-23.5Al-16.5Nb, where the "dummy" was replaced, and a similar temperature gradient was found when cycled 300+ times.

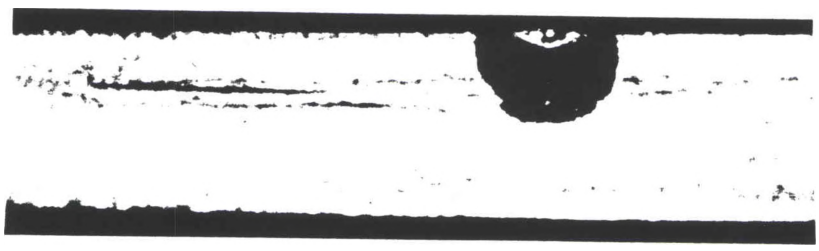

Figure 16. Ti-23.5Al-16.5Nb fracture surface - thermocouple induced crack (27X).

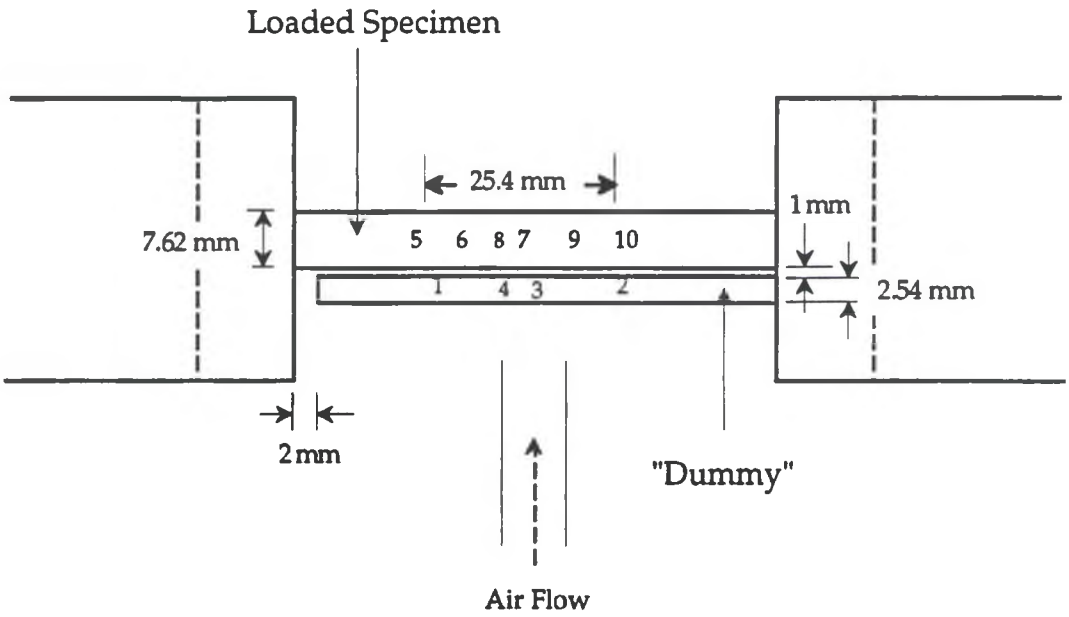

Figure 17. Temperature mapping set-up with thermocouple locations 1-10; thermocouples 4 and 8 are located underneath the "dummy" and demonstration specimens; respectively.

Testing

The initial step in a test is to mark the thermocouple and grip sections of the specimen. The specimen is then mounted and aligned in the grips. After the sample is aligned and the grips are activated, the four thermocouples are attached using a spot welder. Next, the extensometer is comfortably placed against the edge of the specimen at its center. To complete the physical set up, the lamps are positioned and the lamp and specimen cooling equipment are activated. After completing the physical set up, the initial room temperature modulus is measured. This measurement involves recording the stress and strain values during a load control tensile loading. The load profile is defined by a monotonic linear ramp from 0 to 100 MPa, at a approximately 2 MPa/second load rate. The upper limit of 100 MPa is used because 100 MPa is sufficient to ensure a purely elastic response with no introduction of damage to the sample. Upon completion of the initial room temperature modulus check, the specimen parameters and the TMF profile are entered interactively. Prior to cycling, the sample is ramped to maximum

cycle temperature after which a CTE value may be calculated. Next the sample is ramped to minimum load. Maximum temperature and minimum load was the starting point for each OOP TMF test performed. The tests were run at 0.00556 Hz (3 minute cycle) with a temperature range of 150-650°C and a stress ratio ($\sigma_{min}/\sigma_{max}$) of 0.05. After stable OOP TMF cycles were achieved, minimal adjustments to the airflow and air placement were performed throughout the test as necessary. The temperature, time, stress, and strain data were acquired periodically throughout the test. Each set of data represented an entire cycle and was acquired during requested data acquisition cycles (DACs). Typically, data was acquired every 0.9 seconds during the cycle in order to collect 200 points per DAC. The test specimen was cycled to failure, which was defined as the sample breaking into two parts.

CHAPTER IV

RESULTS

In this work, 20 TMF tests were conducted on monolithic titanium alloys. Examination of the effects of heat treatment or composite processing, or their implications on the fatigue life of the materials in question was not intended and no testing of composite material was conducted. This section is intended to provide a general description of the test data and is divided into three sections: fatigue life, strain measurements, and fracture analysis. A correlation to previously acquired composite data, involving micromechanical and experimental results, is provided in Appendix D.

Modulus, CTE, and Life

The approach in developing a tes. matrix was to evaluate a range of stresses in order to develop the fatigue S-N curves for each monolithic alloy, concentrating on lives ranging from 50 to greater than 2000 cycles. Maximum stresses ranged from 350 to 700 MPa for the three alloys tested. Data from the TMF tests included the initial room temperature modulus, CTE as calculated from the initial room temperature ramp, and temperature, stress, and strain from periodic DACs throughout the test. Cycles-to-failure was recorded with failure defined as the specimen breaking into two parts.

The initial room temperature modulus measurements were obtained in order to determine any variation between individual specimens. For each group of monolithic alloys, only small deviations from the average modulus existed. Table 2 lists the average moduli for each material. Timetal 21S displayed a significant stiffness advantage, which

most likely was a result of the stabilizing heat treatment, see Figure 8. Ti-24Al-11Nb held an advantage over Ti-23.5Al-16.5Nb probably as a result of the increased volume fraction of the strong alpha-2 phase. The scatter within the data for each material was minimal ranging from 2 to 7%.

Table 2. Average Moduli

Material	Modulus(GPa)
Timetal 21S	109.8 ± 1.9
Ti-24Al-11Nb	101.4 ± 3.8
Ti-23.5Al-16.5Nb	84.8 ± 5.8

The objective of the CTE measurement was to identify the magnitude of the strain/temperature relationship. Note that only the CTEs from the specimens which were monitored with directly welded thermocouples were reported. The CTE values, tabulated in Table 3, were calculated from the slope of the strain versus temperature plots found in Appendix F. Within the material groups, Timetal 21S and Ti-23.5Al-16.5Nb, the individual specimen CTEs were relatively constant at 9.60 ± 0.13 and 10.39 ± 0.68 mm/mm/°C; respectively.

Table 3. CTE for Selected Alloy Samples

Specimen#	Material	CTE(x 10^{-6} mm/mm/°C)
92-500	Timetal 21S	9.603
92-501	Timetal 21S	9.557
92-502	Timetal 21S	9.524
92-503	Timetal 21S	9.497
92-504	Timetal 21S	9.818
92-524	Ti-24Al-11Nb	11.407
92-530	Ti-23.5Al-16.5Nb	10.702
92-682	Ti-23.5Al-16.5Nb	9.616
93-239	Ti-23.5Al-16.5Nb	10.857

Figure 18 represents the fatigue life data for the three materials, where stress range is plotted as a function of cycles-to-failure (S-N Curve) and Table 4 presents the

corresponding data in tabular form for all the samples tested. For each alloy, the data could be described with a power law curve fit, $N_f = A(\Delta\sigma)^{-n}$. The constants A and n as well as the curve fit parameter, R, have been calculated for each material. A perfect curve fit corresponds to R = 1. The constants are provided in Table 5.

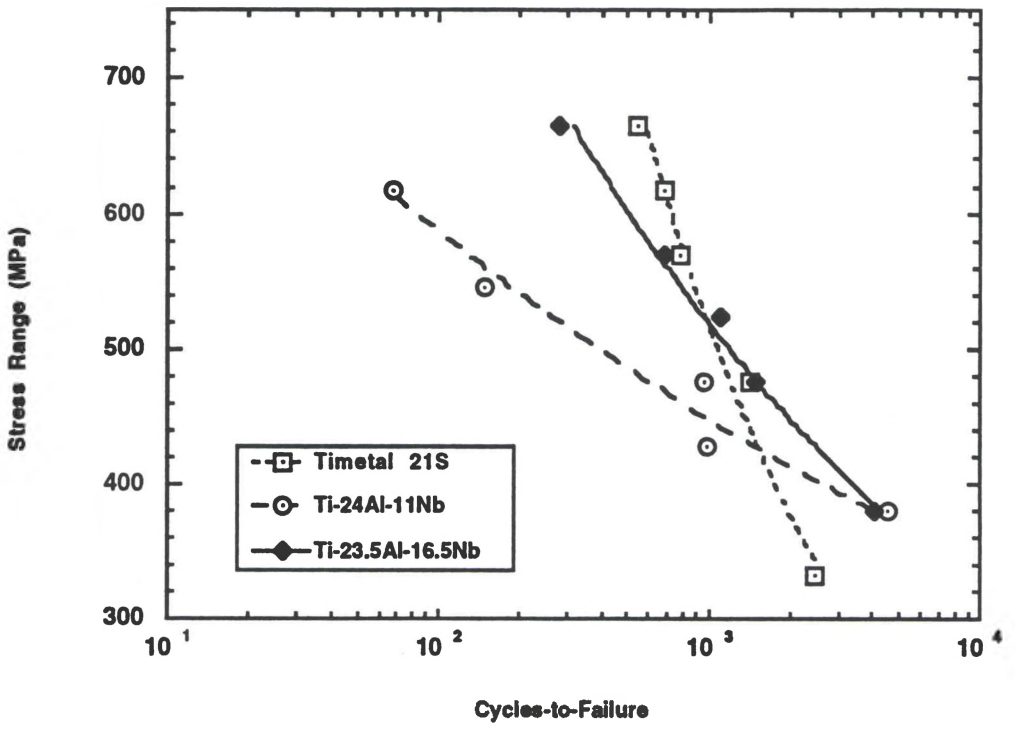

Figure 18. Stress range versus cycles-to-failure for all materials tested.

Table 4. Summary of Results

Specimen	E(GPa)	Max. Stress(MPa)	Strain-to-failure	Cycles
Timetal 21S:				
92-503	110.839	700	.065	542
92-502	unavailable	650	.071	689
92-504	111.032	600	.079	786
92-501	110.896	500	.041	1407
92-500	106.425	350	.019	2453
Ti-24Al-11Nb:				
92-665	106.188	650	.042	68
92-668	96.765	575	.025	148
92-523	106.188	500	.015	960
92-667	97.596	450	.005	982
92-666	102.469	400	.005	4603
Ti-23.5Al-16.5Nb:				
92-684	89.136	700	.074	278
92-683	86.873	600	.013	688
93-206	79.913	550	.007	1115
92-685	105.204	500	.007	1472
92-687	96.960	400	.005	4024

Table 5. Curve Fit Constants for Power Law Equation: $N_f = A(\Delta\sigma)^{-n}$

Material	A	n	R
Timetal 21S	1.15×10^{09}	2.2330	.990
Ti-24Al-11Nb	3.88×10^{26}	8.8924	.982
Ti-23.5Al-16.5Nb	6.98×10^{15}	4.7308	.994

Strain Measurements

The strain values examined in this study were maximum and minimum strain versus cycles and strain-to-failure. The maximum and minimum strain values were acquired each DAC and were plotted versus cycles. Strain-to-failure was defined as the maximum strain recorded on the last DAC. Accurate strain to failure measurements were sometimes difficult to obtain because of the lack of data just prior to failure. The tests

involved a high number of cycles and it was impractical to acquire data for each cycle. Therefore, the strain at failure must be conservatively assumed to be that of the last data cycle obtained. Strains-to-failure are used only to provide trends and are not considered as absolute values.

For Timetal 21S, the maximum/minimum strain plots closely resembled a strain plot from a constant load creep experiment[3]. As depicted in Figures 19 and 20, for the lowest and highest stress tests, the first few cycles (< 50) are comparable to a primary creep stage where strain accumulated at a decreasing rate. The intermediate cycles resemble that of secondary creep, where the strains increased at a nearly constant rate. The last 10% of life is comparable to a tertiary stage, where strain accelerated to catastrophic failure. The acceleration seen in the maximum/minimum strain during the last few cycles may indicate a reduction in the effective cross-sectional area of the specimen as it approaches failure. For the lower stress range cases, this apparent loss of cross sectional area did not seem to be caused by observable necking in the test section, but was probably a result of cracking. Some necking was observed in the higher stress cases.

The Ti-23.5Al-16.5Nb and Ti-24Al-11Nb maximum/minimum strain plots exhibited similar behavior to primary and secondary stage constant stress creep tests, Figures 21 and 22. Characteristic of brittle materials, a tertiary stage was not evident for either material, most likely due the creep resistance of the alpha-2 phase. The maximum/minimum strain versus cycles plots not represented in this chapter are presented in Appendix G.

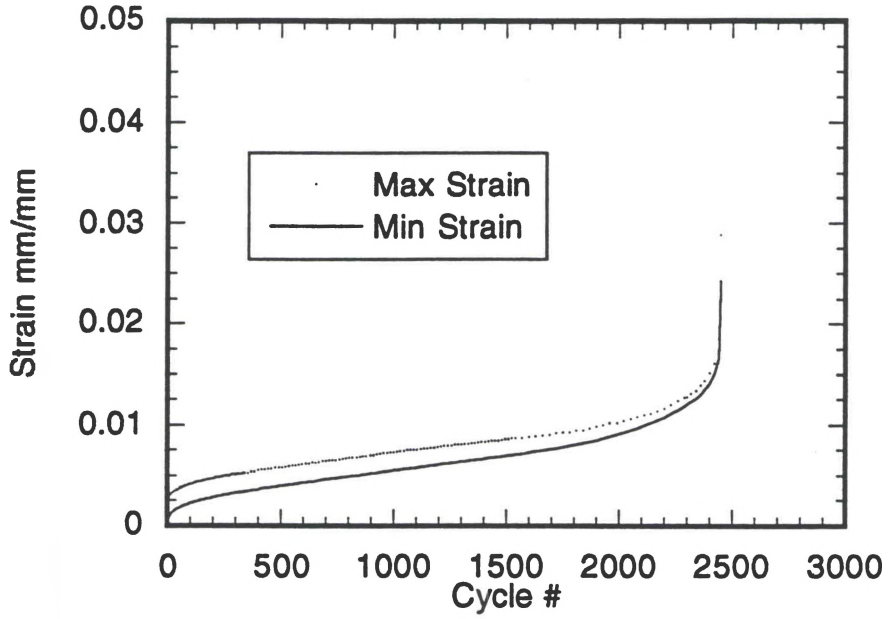

Figure 19. Max./min. strain versus cycles for Timetal 21S; max. stress = 350 MPa.

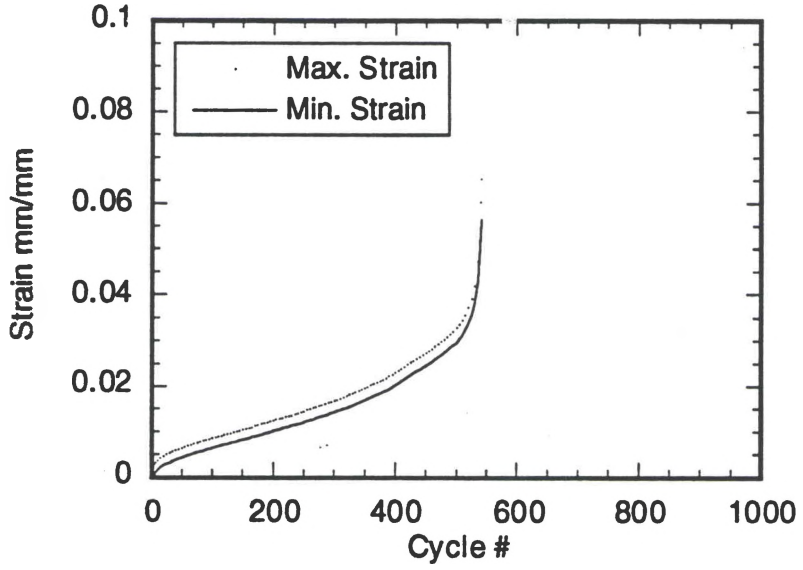

Figure 20. Max./Min. strain versus cycles for Timetal 21S, max. stress = 700 MPa.

The different strain/life behaviors of the three materials is best illustrated by the maximum strain versus cycles plot under identical testing conditions. Figure 23 compares strain measurements for the tests performed at a maximum stress of 500 MPa. Timetal 21S and Ti-23.5Al-16.5Nb reached similar cycles-to-failure, which were about 1.5 times greater than that reached by Ti-24Al-11Nb. However, the strain-to-failure of Timetal 21S was approximately 5.8 times greater than Ti-23.5Al-16.5Nb and 2.7 times greater than Ti-24Al-11Nb. Initial assessment of the strain plots reveal that each material may have experienced creep during the OOP TMF testing.

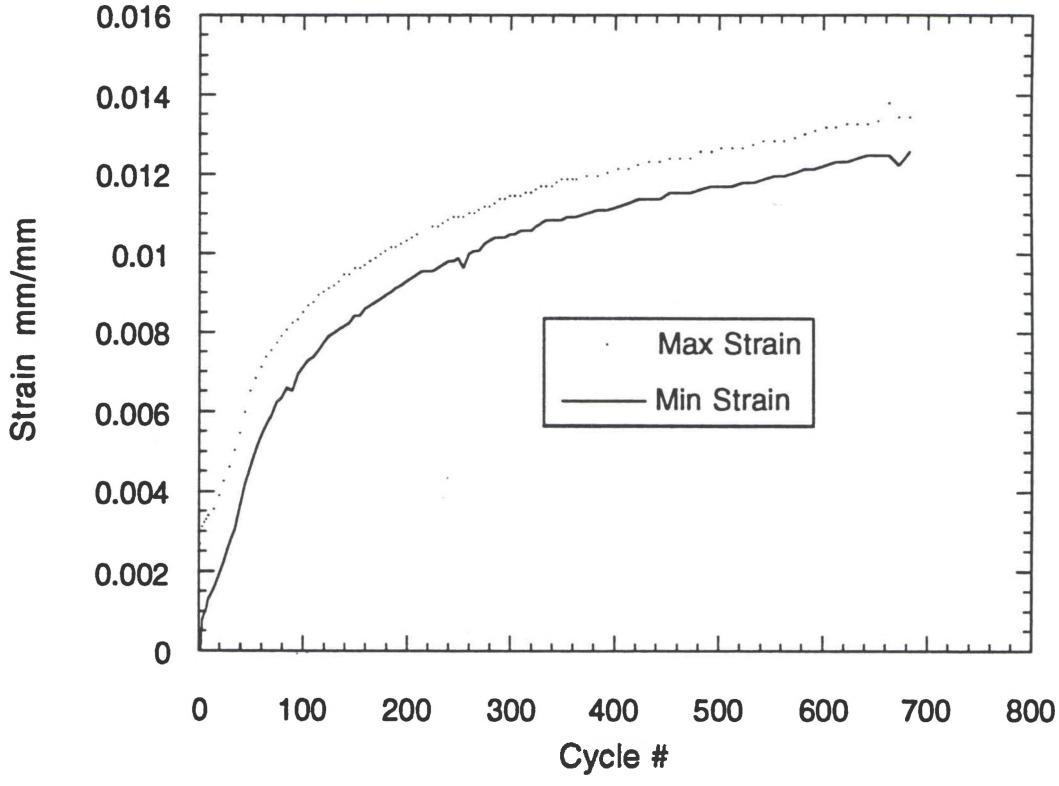

Figure 21. Max/Min strain vs cycles for Ti-23.5Al-16.5Nb; max. stress=600 MPa.

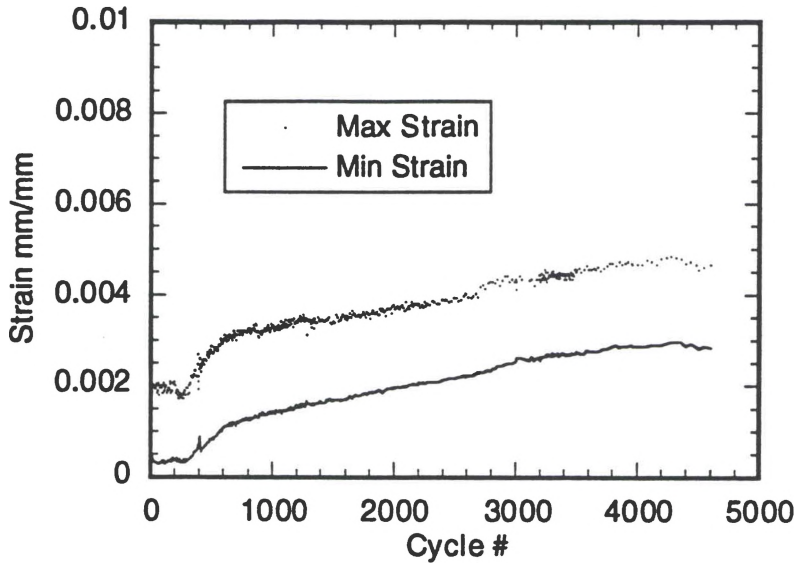

Figure 22. Max/min strain versus cycles for Ti-24Al-11Nb; max. stress = 400 MPa.

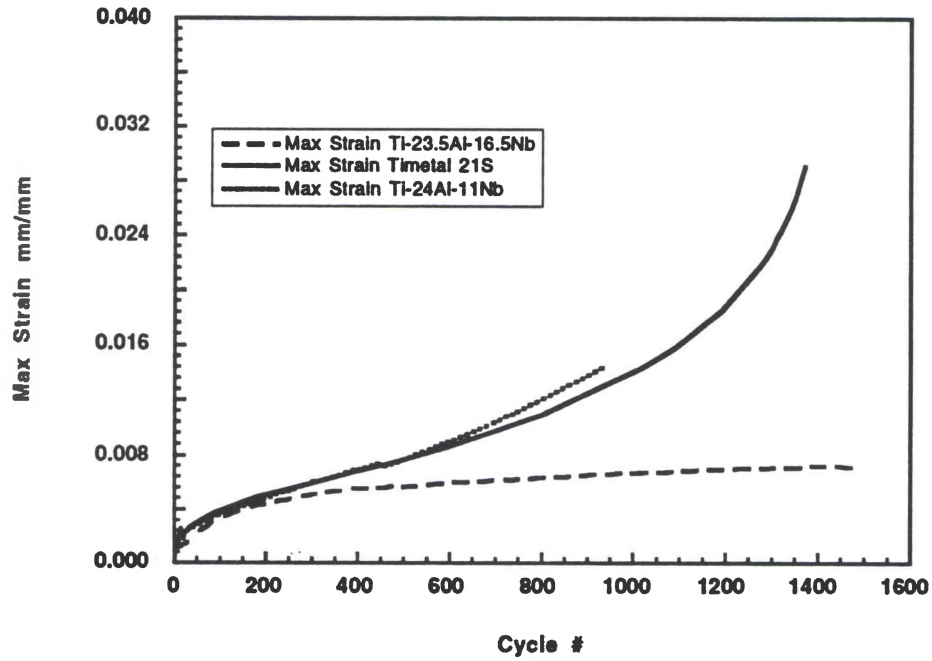

Figure 23. Max. strain versus cycles for the three materials at max. stress = 500 MPa.

Strains-to-failure for each test are provided in Table 4. In general, the higher maximum stress cases experienced greater strains-to-failure. This could be explained by the materials experiencing additional plastic strains in the initial cycles as a result of the higher stress. For the similar maximum stresses, Timetal 21S provided greater strains-to-failure than the other two alloys, while the strains-to-failure of Ti-24Al-11Nb and Ti-23.5Al-16.5Nb were similar. It is interesting to note that the monolithic data disagrees with that of $[0/90]_{2S}$ SCS-6/Timetal 21S composite performed by Hanson[13]. The composite demonstrated a time/cycle dependent function between the maximum applied stress and the strain-to-failure, which correlates to the creep type behavior discussed previously. Hanson explained that as the maximum applied stress is reduced, the number of cycles, and the amount of time at maximum stress and temperature, is increased. With increased time at maximum load and temperature, the composite responded with an increased permanent elongation. The monolithic material tested in this work did not show this time/cycle dependent behavior.

Fracture Analysis

This section is divided into fractographic and metallographic examinations. The techniques used for examination of environmental crack damage and fracture analysis involved both optical and scanning electron microscopy. Optical microscopy (OM) was utilized to examine both the fracture surface and areas adjacent to the fracture surface. In order to evaluate interior damage, tested specimens were sectioned using a low-speed diamond saw and mounted in a thermoplastic resin. The mounted samples were polished with successively finer grades of silicon carbide paper, diamond paste, and a final polish of master met so that microstructural damage occurring in the numbered faces represented in Figure 24 could be observed. Each mount was then etched in a Kroll's reagent to reveal the grain structure. Scanning electron microscopy (SEM) was used to

evaluate the unmounted fracture surfaces, which were cleaned in an acetone ultrasonic bath prior to inspection.

Fractography

Low magnification photomicrographs of Timetal 21S fracture surfaces indicate that the cross-sectional area for a higher stress case was smaller than for the lowest stress case, Figures 25 and 26. Therefore, the higher stress case necked more than the lowest stress case. SEM photomicrographs reveal that the Timetal 21S fracture surface of the highest stress case contained what appeared to be several initiation sites located along the surface edges, Figure 27, while the lowest stress case contained fewer but larger cracks, Figure 28. For every case, ductile dimpling was evident throughout the interior, and an example is shown in Figure 29. Secondary cracking along the sample's side face (#1 in Figure 24) is illustrated in Figures 30 and 31, where the highest stress case contained considerably more cracking than the lowest stress case. Additionally, a point of initiation is identified in the lowest stress case, Figure 32.

Ti-24Al-11Nb samples did not exhibit ductile dimpling. Instead cleavage was characteristic of the overload regions, Figure 33. Crack growth was identified by a discolored region representing the oxidized zone for each case. Low magnification photomicrographs indicate that this oxidized crack growth region is related to maximum stress whereby the highest maximum stress exhibited the smallest oxidized zone and the lowest maximum stress case exhibited the largest oxidized zone, Figures 34 and 35. For every case, initiation occurred at a corner location, characterized by the greatest area of planar fracture, where due to the rectangular geometry, the greatest stress concentration exists, Figure 36.

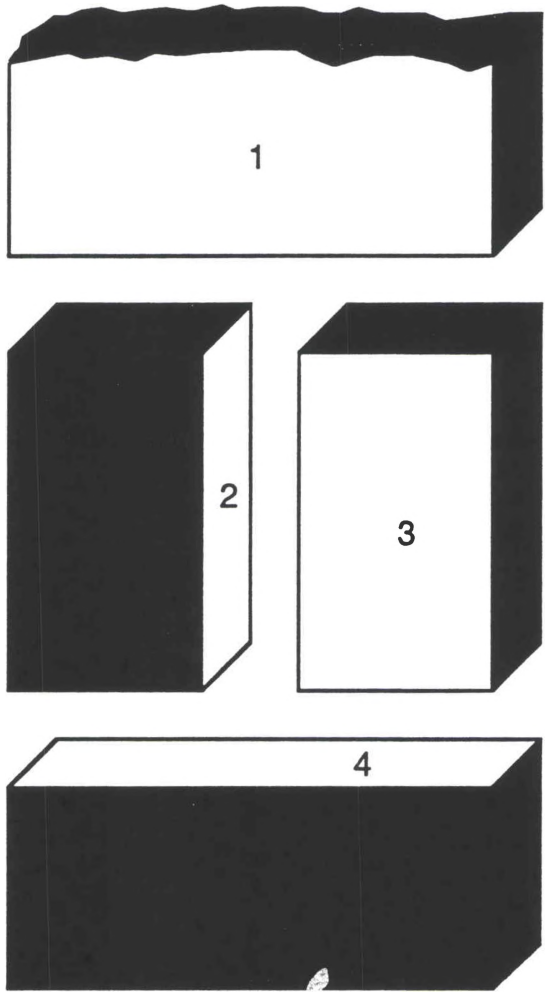

Figure 24. Sectioned heated zone polished surfaces: 1 - top face adjacent to fracture surface; 2 - longitudinal face; 3 - top face in gage section; 4 - transverse face.

The near-orthorhombic alloy, Ti-23.5Al-16.5Nb, exhibited fracture characteristics comparable to both the Timetal 21S and Ti-24Al-11Nb alloys. Like the alpha-2 alloy, the fracture surface interior demonstrated cleavage, Figure 37, and the initiation sites were located at corners, Figure 38. Similar to Timetal 21S, the number of initiation sites seemed to be a function of the stress level. At higher stress levels, the greatest number of crack initiation and propagation regions occurred along the edges, Figure 39, while in lower stress cases initiation sites were mainly found at corner locations. Very little

secondary cracking was observed along the sample sides for Ti-23.5Al-16.5Nb, Figure 40, and Ti-24Al-11Nb, Figure 41.

Figure 25. Timetal 21S fracture surface of maximum stress = 650 MPa (24X).

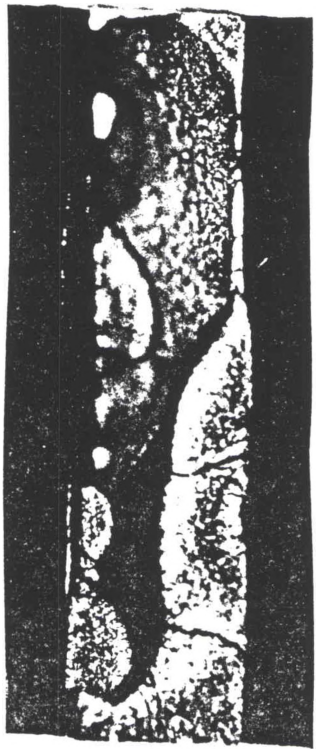

Figure 26. Timetal 21S fracture surface of maximum stress = 350 MPa (24X).

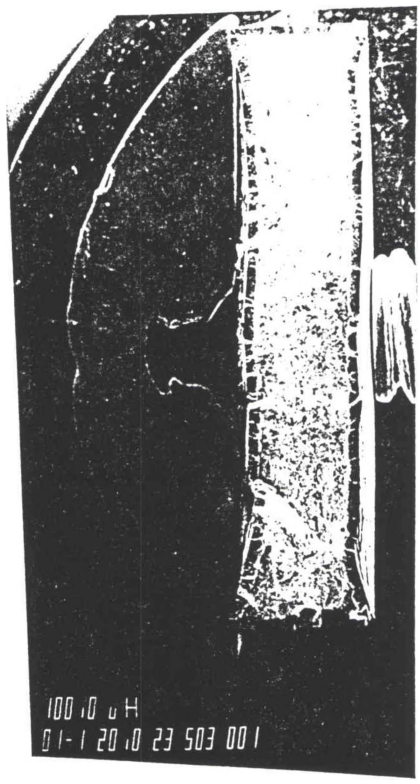

Figure 27. Timetal 21S fracture surface of maximum stress = 700 MPa.

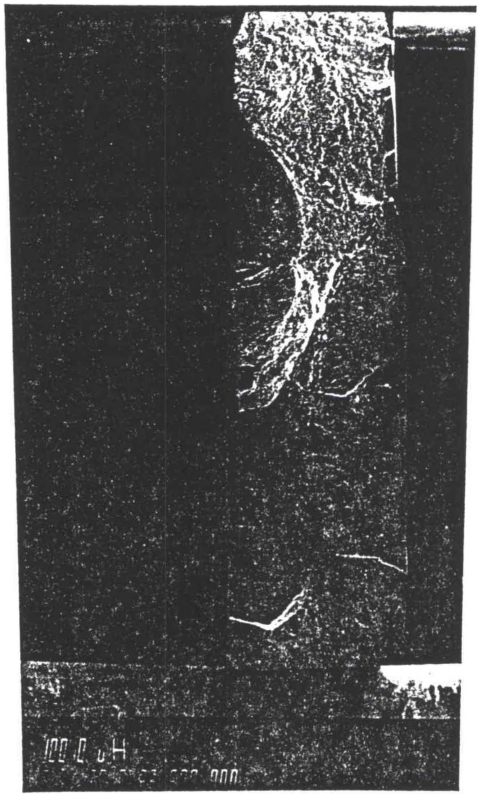

Figure 28. Timetal 21S fracture surface of maximum stress = 350 MPa.

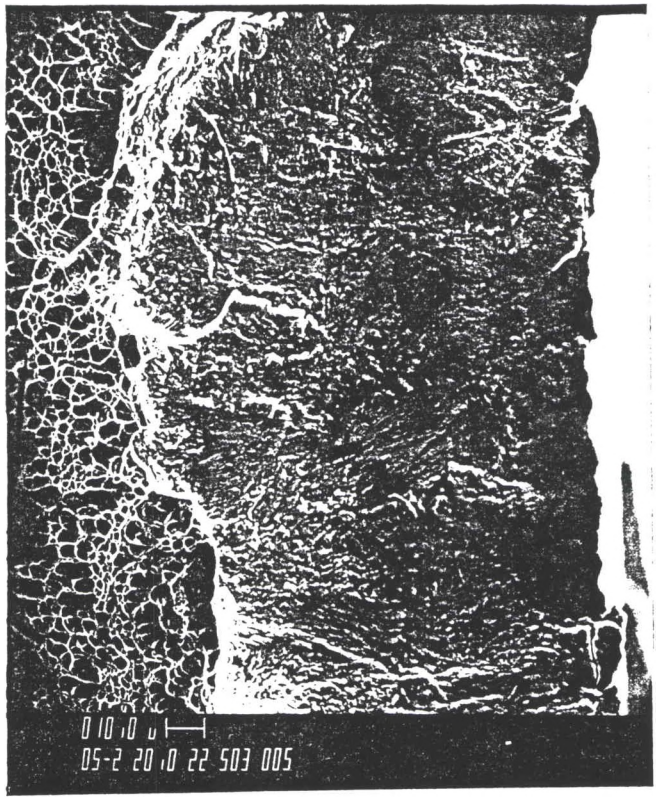

Figure 29. Timetal 21S, 700 MPa exhibiting dimpling at edge of fatigue crack zone.

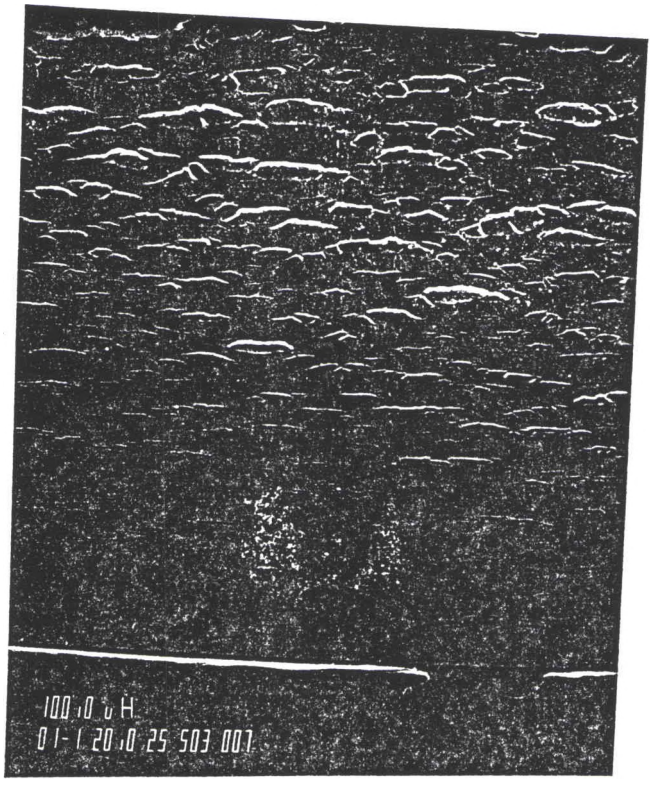

Figure 30. Timetal 21S exhibiting cracking at the surface for max stress = 700 MPa.

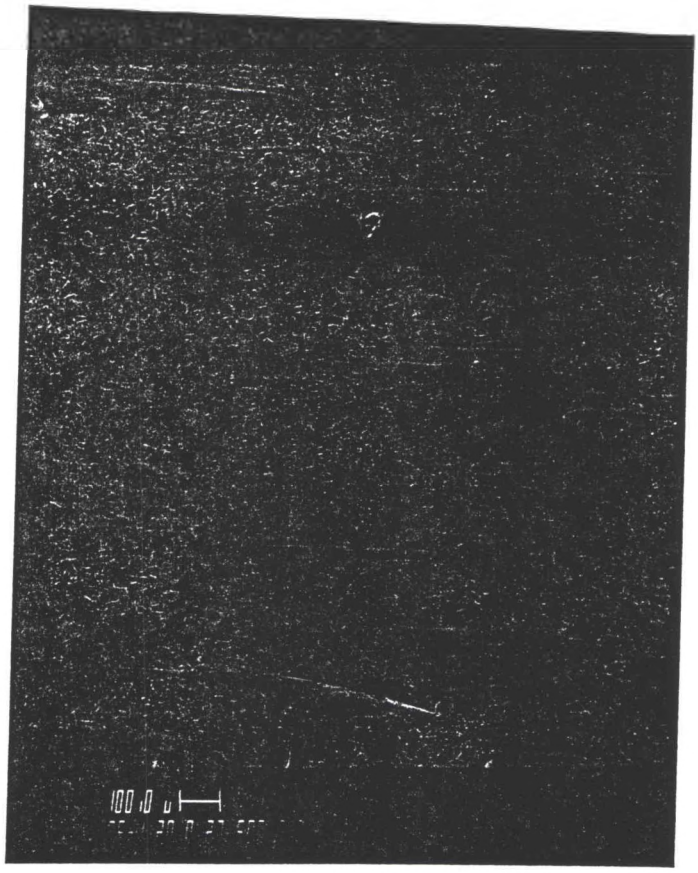

Figure 31. Timetal 21S exhibiting cracking at surface for max. stress = 350 MPa.

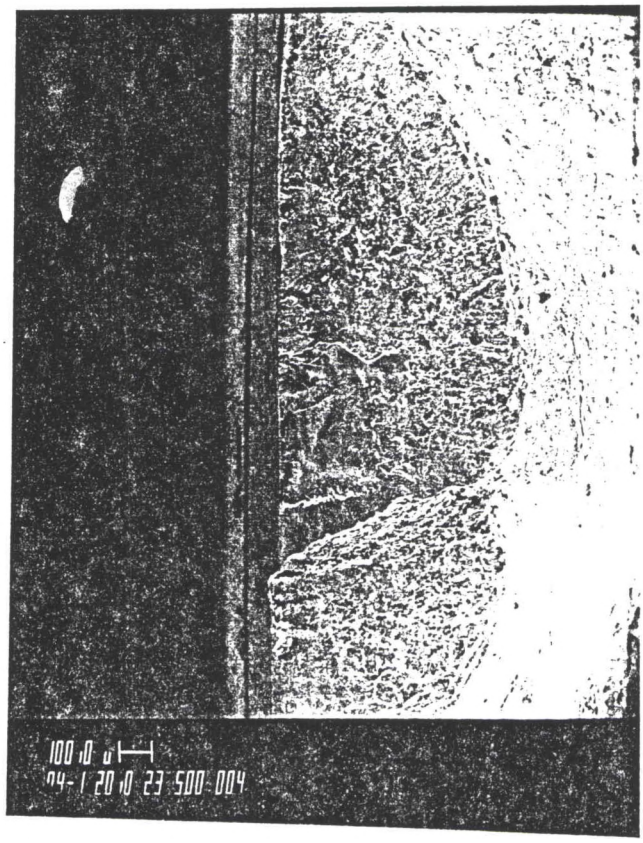

Figure 32. SEM photograph indicating initiation site (center) Timetal 21S; 350 MPa.

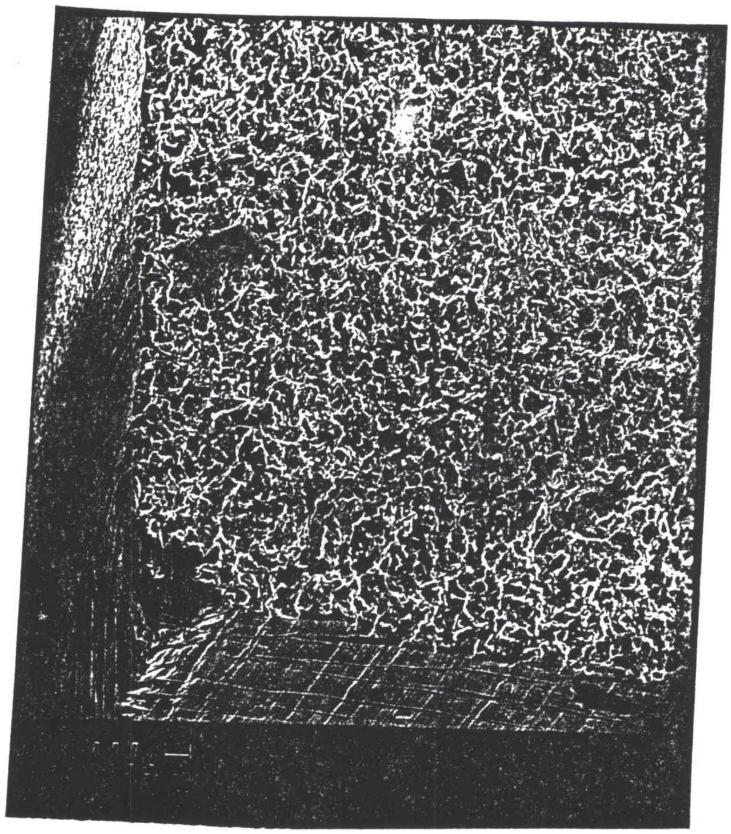

Figure 33. Ti-24Al-11Nb overload zone exhibiting cleavage; max stress=400 MPa.

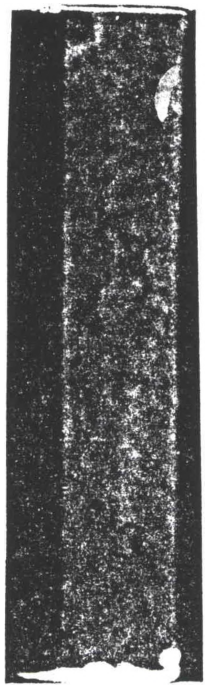

Figure 34. Ti-24Al-11Nb fracture surface for maximum stress = 650 MPa (20X).

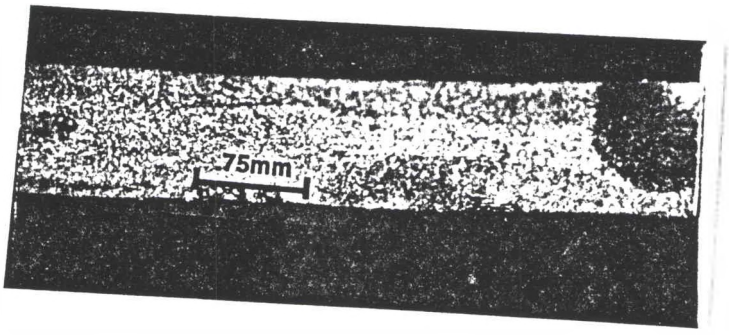

Figure 35. Ti-24Al-11Nb fracture surface for maximum stress = 400 MPa (24X).

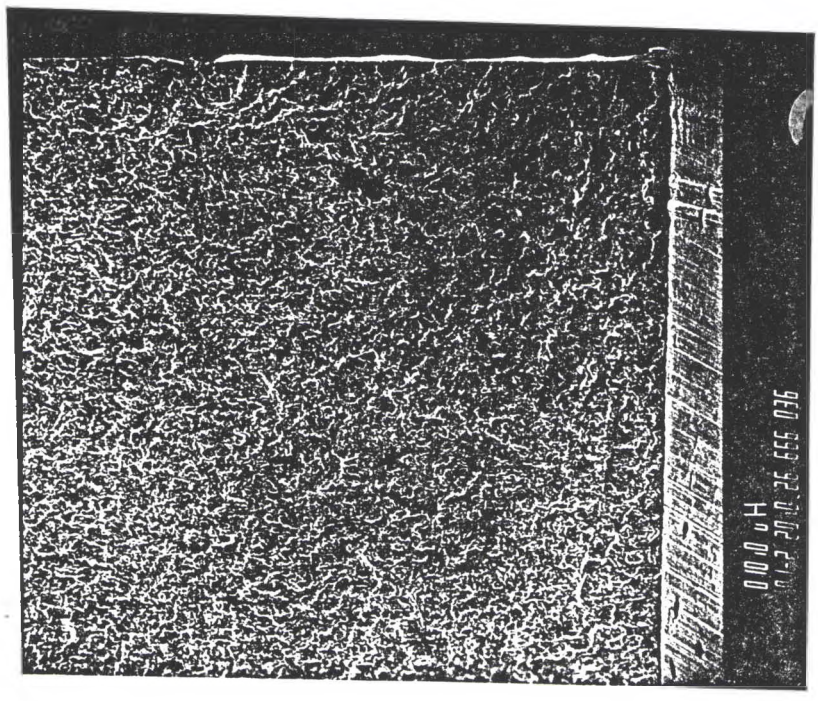

Figure 36. Ti-24Al-11Nb oxidized corner for maximum stress = 400 MPa.

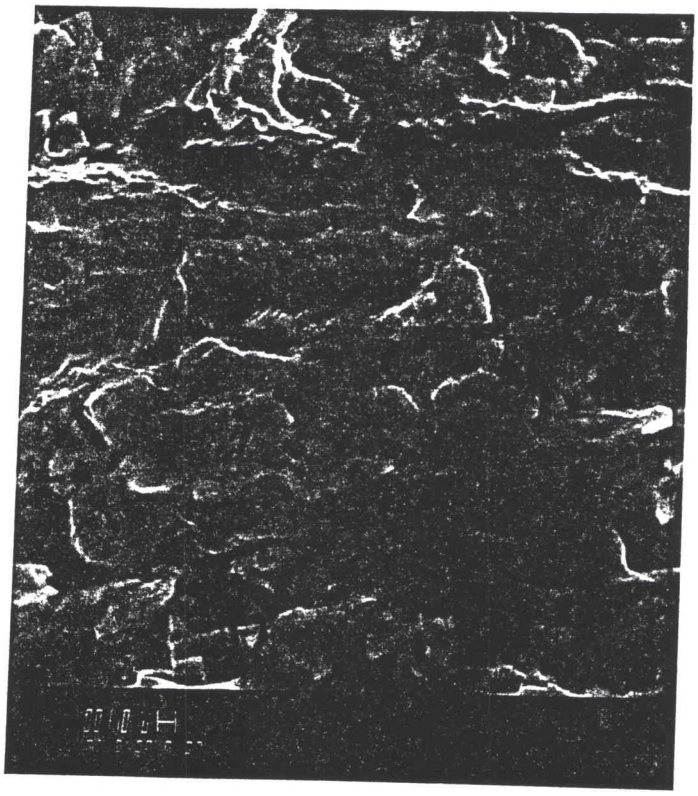

Figure 37. Cleavage/overload region of Ti-23.5Al-16.5Nb, max. stress = 700 MPa.

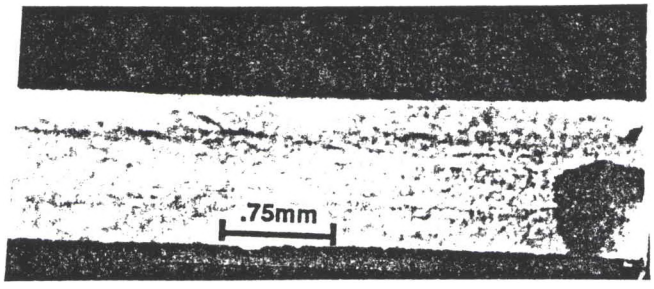

Figure 38. Oxidized zone for Ti-23.5Al-16.5Nb at max. stress = 500 MPa (24X).

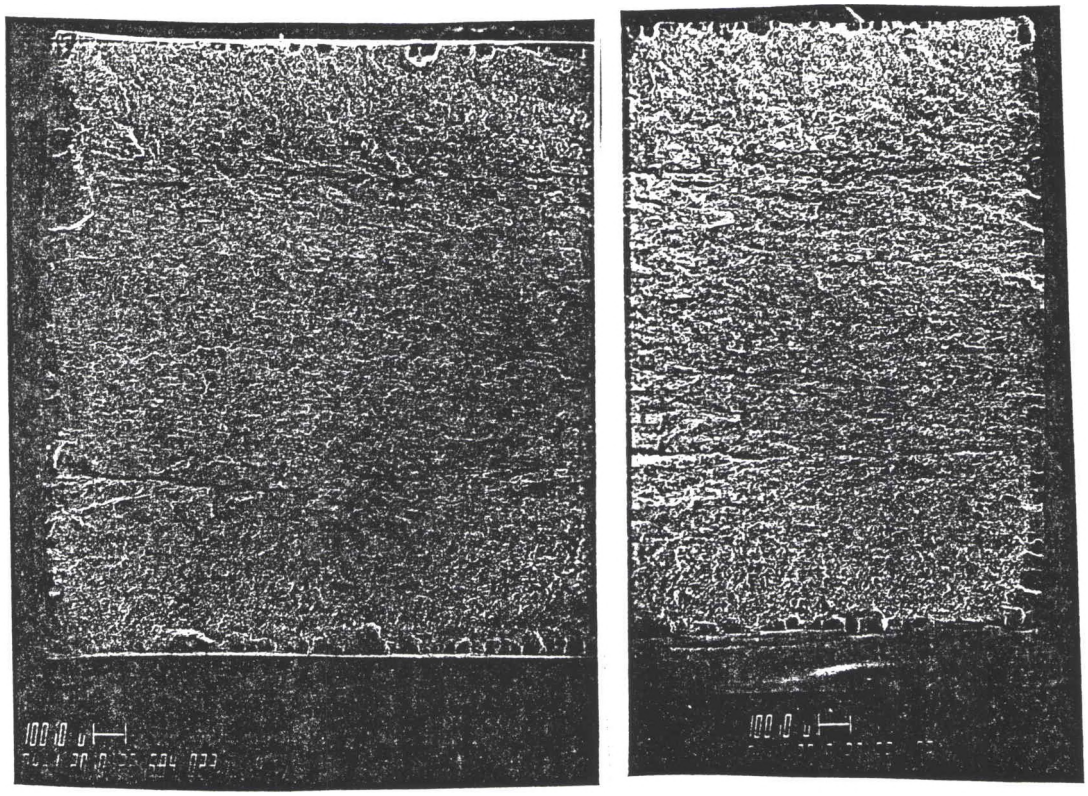

Figure 39. Ti-23.5Al-16.5Nb surface crack initiation/propagation regions; 700 MPa.

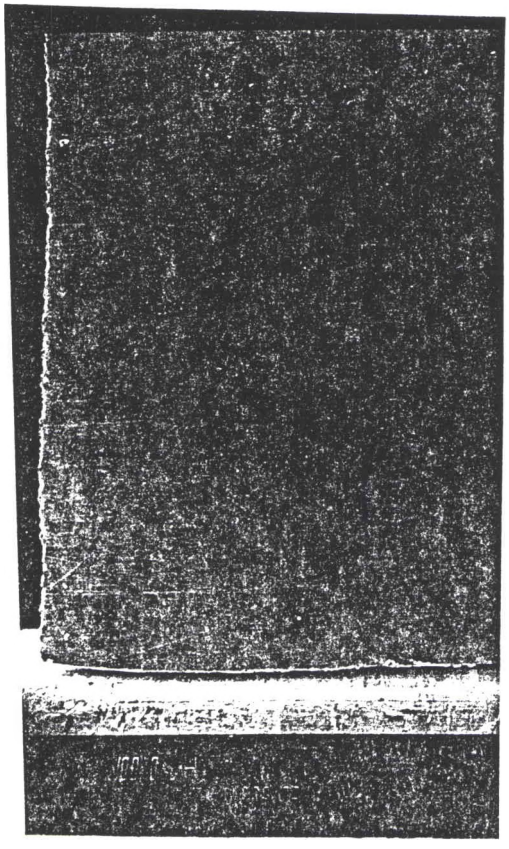

Figure 40. Surface of Ti-23.5Al-16.5Nb for maximum stress = 500 MPa.

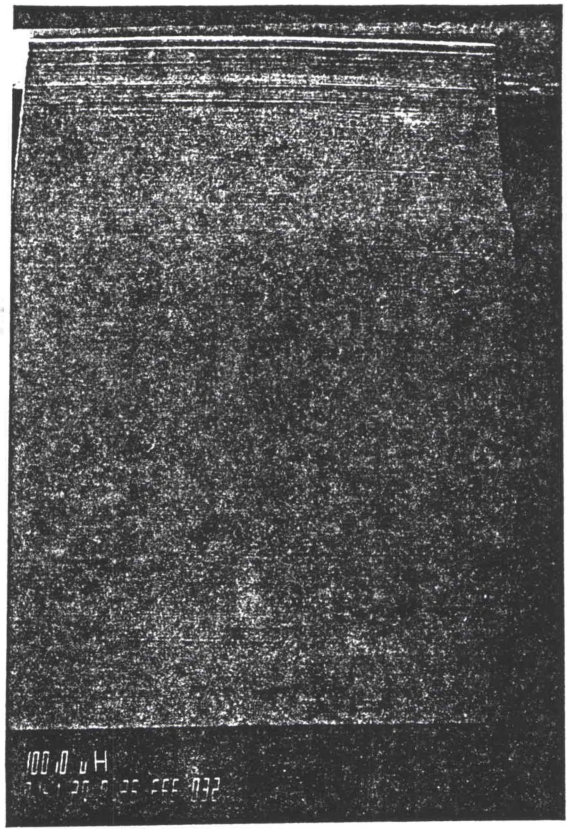

Figure 41. Surface of Ti-24Al-11Nb for maximum stress = 400 MPa.

Metallography

Optical microscopy (OM) was used to analyze the oxidized regions adjacent to the fracture surfaces of specimens. Differences were observed between the alloys. Timetal 21S contained cracking throughout the heated zone, with the highest stress samples showing considerably more secondary cracking where the cracks were shorter than in the lowest case, Figures 42 and 43. Ti-24Al-11Nb had much less secondary cracking, which was limited to surface edges. However, when evident, it was on the same order of magnitude as the alpha-2 grain size, Figure 44. The near-orthorhombic alloy, which exhibited larger alpha-2 grains, contained secondary cracks found at the surface and interior locations which were larger than those of Ti-24Al-11Nb, Figures 45 and 46.

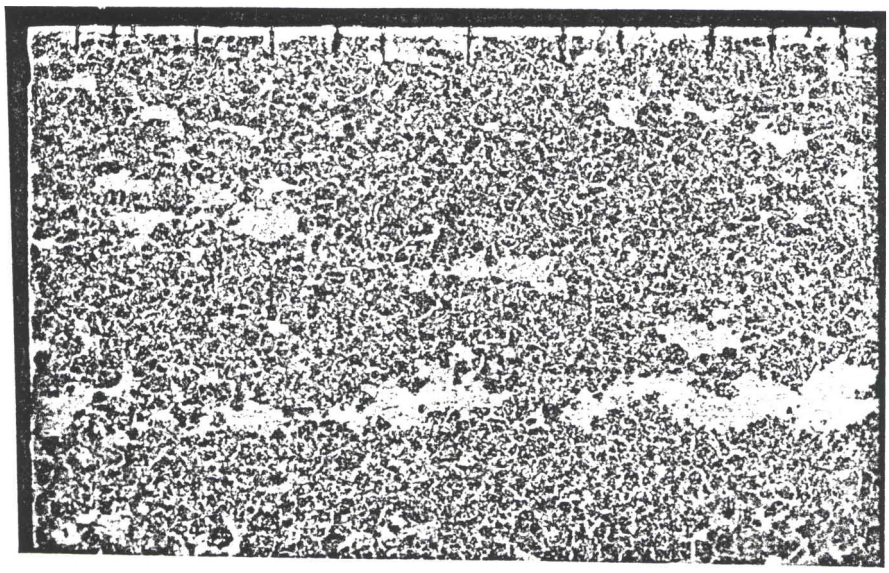

Figure 42. Secondary cracking in Timetal 21S for maximum stress = 700 MPa (50X).

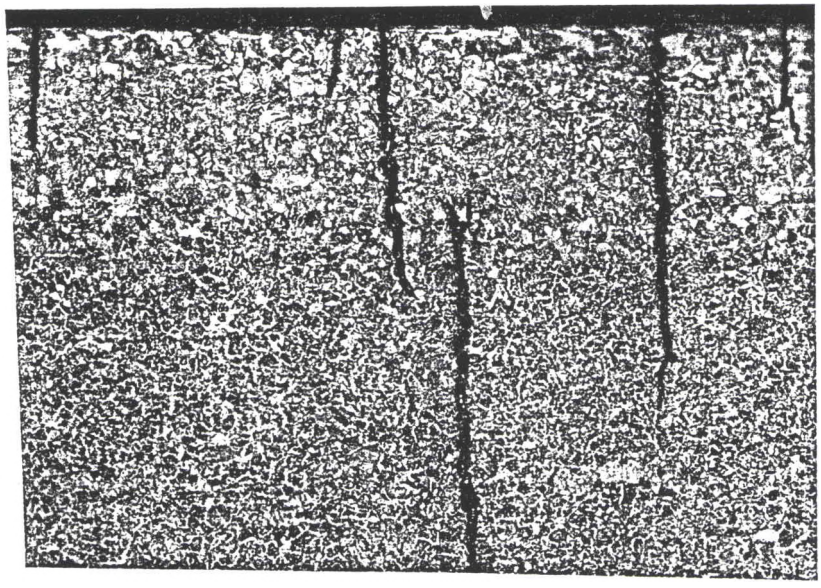

Figure 43. Secondary cracking in Timetal 21S for max. stress = 350 MPa (50X).

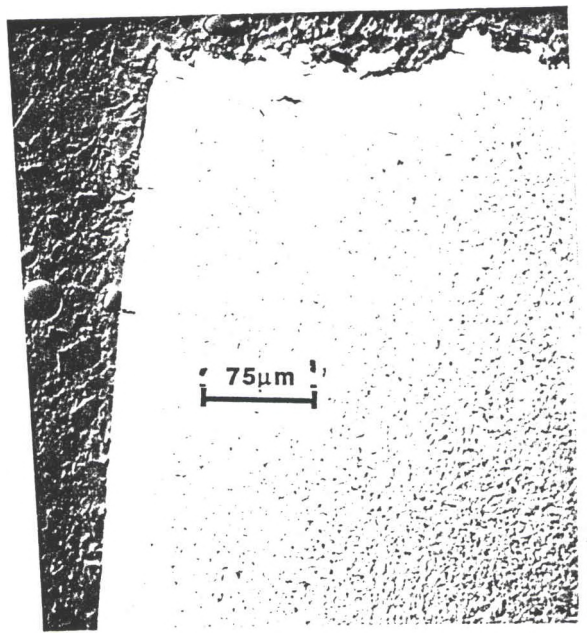

Figure 44. Secondary cracking in Ti-24Al-11Nb for max. stress = 650 MPa (200X).

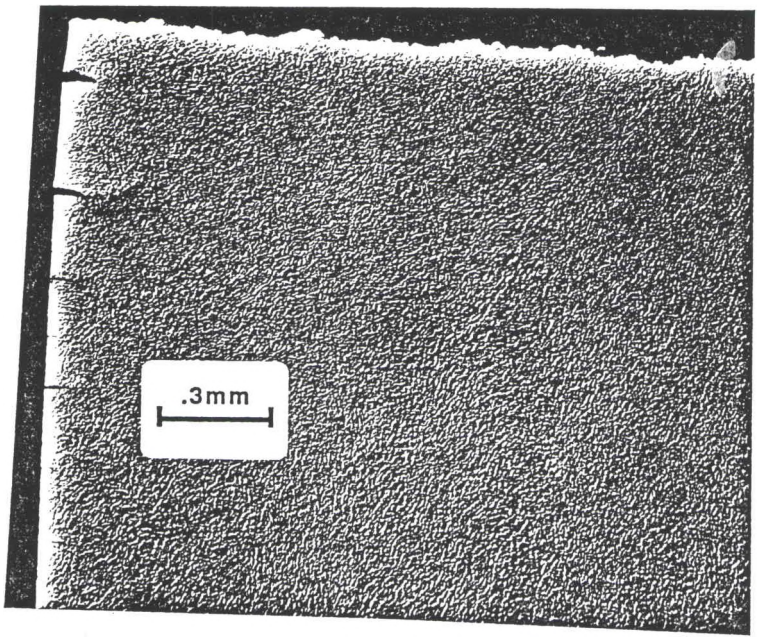

Figure 45. Ti-23.5Al-16.5Nb surface secondary cracks; max stress=700MPa (40X).

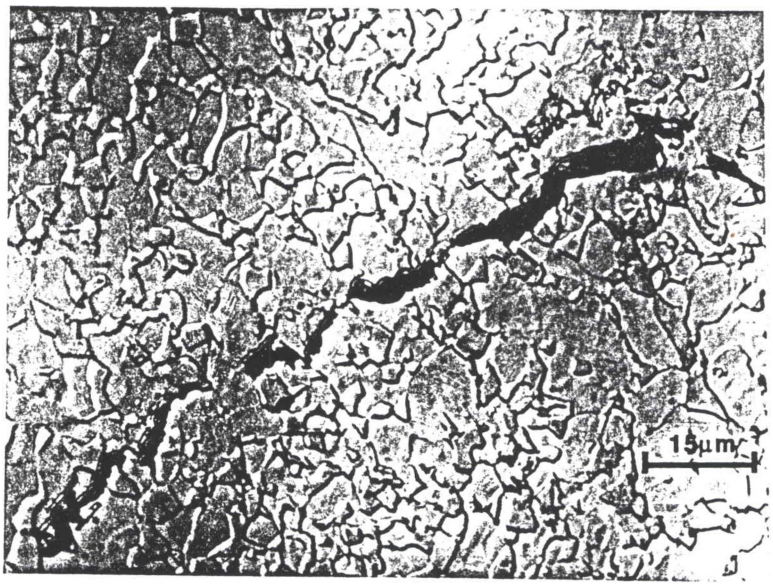

Figure 46. Ti-23.5Al-16.5Nb interior secondary crack; max stress=500 MPa(1000X).

Hardness

Vicker's hardness (Hv) was computed for the Timetal 21S metallographic samples, specifically on the polished and etched transverse faces (#4 of Figure 24), to determine if there was a hardness difference through the thickness of the specimens. Hardness values were computed at specified locations along the thickness of the transverse samples as depicted in Figure 47. Hv as a function of distance from the closest edge is depicted graphically in Figure 48. The areas closer to the edge were harder than interior regions indicating that more alpha phase may have been present at the edges.

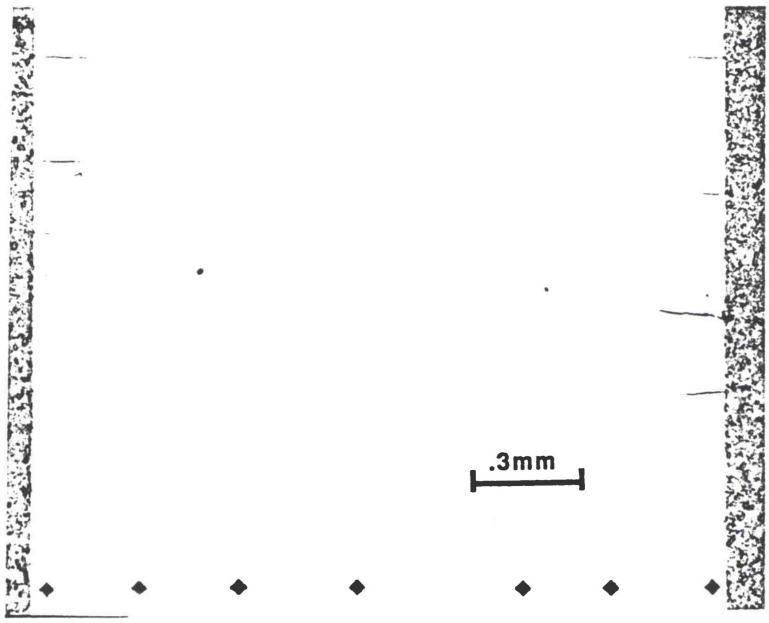

Figure 47. Vickers hardness indentations along the thickness of Timetal 21S (50X).

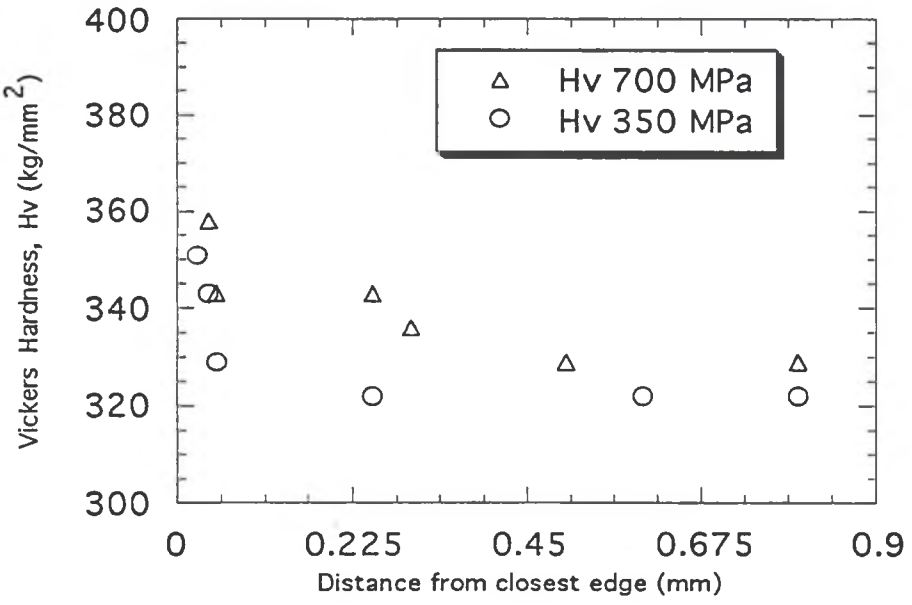

Figure 48. Vickers hardness versus distance from the closest edge.

CHAPTER V

ANALYSIS AND DISCUSSION

Fatigue Curves

Metals and alloys tend to exhibit fatigue S-N plots of two basic shapes, one incorporates a fatigue limit and the other, associated with non-ferrous metals, does not experience an endurance or fatigue limit below which the material can be cycled indefinitely. It has been observed that at low stress levels, titanium alloys do not possess a fatigue limit[30]. This particular evaluation, with all specimens failing before 10,000 cycles, which for purposes of this work was considered the run-out limit, did not attempt to prove or disclaim this assessment of titanium alloys. As would be expected, as the stress level was increased the resulting fatigue life was reduced.

When comp ring all three materials, Timetal 21S experienced the greatest life at the highest stress ranges, Ti-24Al-11Nb experienced greatest life at the lowest stress range, and Ti-23.5Al-16.5Nb experienced the greatest life at the intermediate stress ranges, Figure 18. At the higher stress range, Ti-23.5Al-16.5 Nb had fatigue behavior closer to Timetal 21S, Figure 18.

Cross-Over of S-N Curves

The fatigue life of metals can be conveniently divided into two stages: crack initiation and crack propagation[30]. At low stress levels, fatigue crack initiation dominates fatigue life, while at high stress levels, crack propagation dominates. However, one major drawback of studies of fatigue behavior of a material using the S-N

approach is that no distinction can be made between the crack initiation phase and the crack propagation phase. In each material studied, the crack initiation and propagation phases are thought to be characteristically different. The cross-over in life experienced between Timetal 21S and Ti-24Al-11Nb at relatively low stress ranges, shown in Figure 18, can be explained through crack initiation and propagation lives. At lower stress levels, the period for a crack to initiate is longer than at higher stress levels. Due to the potentially higher crack resistance of Ti-24Al-11Nb, this alloys experiences a longer initiation life than Timetal 21S. However at higher stress levels, cracks take less time to initiate. Once the crack initiated in Ti-24Al-11Nb, it more quickly propagated until reaching critical length, when fracture immediately ensued. Timetal 21S, on the other hand, is more tolerant to cracking and did not experience one dominant crack. Cracks initiated at several locations and grew until the cross-sectional area was decreased to the point where the load was greater than the load carrying capability. Thereby, cracks developed and propagated over a longer period of time than Ti-24Al-11Nb. This can explain why at high stress ranges, Timetal 21S experienced longer lives while at the lowest stress ranges, the Ti-24Al-11Nb life was longer.

Ti-23.5Al-16.5Nb appeared more tolerant to cracking than Ti-24Al-11Nb, yet similar to Ti-24Al-11Nb, failure was controlled by a dominant crack. Therefore, this alloy can be considered to have a longer crack propagation life than Ti-24Al-11Nb and a longer initiation life than Timetal 21S, which explains why at the intermediate stress ranges Ti-23.5Al-16.5Nb experienced the longest lives. At low stress levels Ti-23.5Al-16.5Al displayed behavior closer to Ti-24Al-11Nb, and at the highest stress levels the lives more resembled Timetal 21S.

Fracture Characteristics

The failure modes and fracture surfaces for each monolithic material differed. The mechanisms of failure which appeared to occur for all materials were fatigue crack

initiation and propagation, oxidation, and creep. In the overload regions, Timetal 21S failed in a ductile manner, while Ti-24Al-11Nb and Ti-23.5Al-16.5Nb failed in a more brittle manner.

Timetal 21S experienced a more ductile fracture than either Ti-24Al-11Nb or Ti-23.5Al-16.5Nb, Figure 29. The fracture surfaces revealed several crack initiation sites located at the specimen edges, Figures 27 and 28. The cracked regions surrounded an interior region of overload fracture with ductile dimpling. Comparing a specimen having experienced a higher stress condition to that of a lower stress test, an increased number of initiation sites were observed for the higher stress conditions. The fracture surfaces revealed a smaller oxidized crack growth area for the high stress tests than for the low stress tests. This is expected since the fracture toughness is achieved for smaller cracked areas at higher stresses. However, for secondary cracks away from the fracture surface, the higher stress test specimen experienced more cracking than the lower stressed samples. The secondary cracking observed was not as severe as the cracking on the fracture surface. The damage appeared to be a synergistic effect of fatigue, creep, and environmental aspects, oxidation and oxygen embrittlement.

The Ti-24Al-11Nb alloy experienced a brittle flat-type fracture where the overload region exhibited cleavage, Figure 33. Initiation sites were located at corners, where for each specimen a discolored area representing the oxidized crack region was observed, Figures 34 and 35. Typically, a dominant crack developed and grew until a critical crack length was reached, whereupon a catastrophic overload brittle fracture occurred. Critical crack size appeared to be dependent on the stress level. As shown in Figures 34 and 35, the oxidized region was smallest for the highest stress case, and the lowest stress cases displayed the largest oxidized zone. No attempt was made to calculate the fracture toughness based on the stress level, crack geometry, and critical crack length. Overall, the fracture surfaces, excluding the crack region, contained cleavage. The initiation sites and crack growth regions were relatively smooth and featureless.

Secondary cracking, however, was not as prevalent as in the Timetal 21S specimens, and observed cracking was on the order of the alpha-2 grain size, Figure 44.

Ti-23.5Al-16.5Nb experienced failure modes having characteristics of both the Timetal 21S and Ti-24Al-121Nb. For the highest stress levels, Figure 39, the fracture surfaces revealed several initiation sites at the specimen corners, similar to Ti-24Al-11Nb, and along the face, similar to Timetal 21S. Similar to Ti-24Al-11Nb, the overload region experienced brittle cleavage failure, Figure 37. For the lower stressed conditions the fracture surface more resembled the Ti-24Al-11Nb alloy, where fewer, larger cracks were observed, and initiation was primarily at corners. Secondary cracks extended beyond one grain size and were larger than the secondary cracks for Ti-24Al-11Nb, yet were not as prevalent as those of Timetal 21S.

Oxidation

Oxidation posed a considerable problem because the oxide was in tension at low temperature, when the oxide is more brittle. The highest stressed Timetal 21S specimen, Figures 25 and 27, demonstrated a uniform depth of cracking which may have been an indication of an oxygen diffusion zone. Additionally, Figures 42 and 43 depict a lighter region close to the surfaces which explains the higher hardness measured at the location adjacent to the edge, Figure 48. Because oxygen is an alpha stabilizer, when the beta phase becomes saturated with oxygen, which diffuses through the alloy at the surface, it has the propensity to transform to alpha phase ($TiAl_3$). This transformed alpha phase has been observed in previous evaluations of this material at similar temperatures/times[32]. The alpha phase tends to be stronger and harder than the beta phase. The increased hardness experienced at edges, Figure 48, can then be explained by oxygen diffusion enabling the harder alpha phase to precipitate out of the beta phase. Although an in-depth fractographic analysis evaluating the microstructure of failed specimens at high magnifications was not performed, edge locations would be expected to exhibit more

alpha phase within beta grain boundaries than interior locations. Crack initiation and propagation is therefore thought to have been enhanced by oxidation damage mechanisms at the specimen surface, where the lower stress tests provided more oxidation damage then the higher stress cases due to the longer time at temperature, allowing for increased oxygen diffusion.

Creep

Although the creep damage has not been quantified, there were indications that the monolithic Timetal 21S failures were enhanced by creep damage mechanisms. There also appeared to be a synergistic effect due to the combination of fatigue and creep. The graphical representation of strain versus cycles, Figures 19 and 20, exhibits similar characteristics of a creep curve where primary, secondary, and tertiary stages were represented. To better illustrate this creep representation a plot of strain versus time is presented in Figure 49. In Chapter I, it was established that Timetal 21S matrix composites creep at 650°C with an applied load of 345 MPa[9]. Therefore, the matrix alone is expected to creep under identical conditions. Although, in this work the range of applied stresses at this temperature included 17-35 MPa (5% of maximum stress), where notches or stress concentration areas could have locally increased the effect of these stress levels, the author feels that the majority of creep damage occurred at times between the maximum and minimum temperature and applied stress. In this study, monolithic Timetal 21S experienced times at stresses of 350 MPa with temperatures ranging from 150-360°C. It is felt that creep may have occurred at intermediate points in the OOP TMF cycle such as this, where intermediate loads are applied at intermediate temperatures.

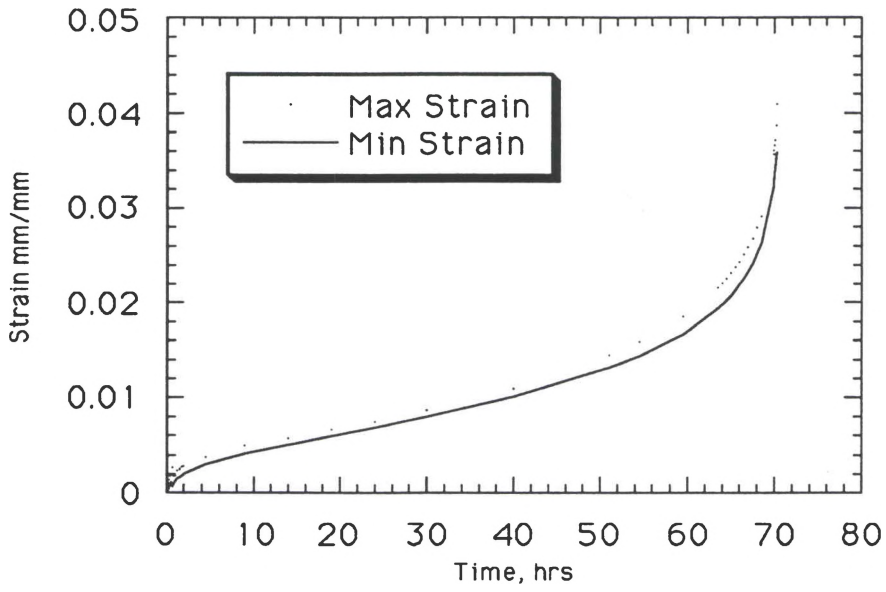

Figure 49. Max and Min strain versus time for Timetal 21S; max stress = 500 MPa.

Although, the fatigue life cross-over behavior has been explained by fatigue crack initiation and propagation assisted by oxidation, creep is expected to have influenced the lives as well. Yet, because creep is both time and load dependent, it can be argued that more creep damage occurred at the higher stress levels or, because of the longer time at temperature, lower stress levels. This issue is complicated by the fact that creep damage is considerably difficult to quantify and the relative significance of creep over the stress ranges tested therefore remains unanswered.

Creep may have occurred in the other two alloys as well. However, due to the excellent creep resistance of alpha-2 phase alloys, creep is not expected to affect the behavior as much as for Timetal 21S. The indications of creep are best explained through the first two creep stages. At the onset of the test the strain behavior for both materials revealed an gradual increase in mean strain similar to primary creep, Figures 21 and 22. This increase was followed by a relatively constant mean strain, or steady-state increase,

similar to secondary creep. Logarithmic creep, which occurs at relatively low temperature and at stresses close to the yield, appeared to be characteristic of these two alloys. During logarithmic creep, strain remains relatively constant over a majority of life, which was evidenced through the strain plots exhibited by these alloys, Figure 21 and 22. Common to less ductile materials deformed in creep (especially logarithmic creep), a tertiary stage was not observed. The cleavage type brittle fracture that occurred probably prevented the plastic deformation necessary for localized necking and microvoid formation. Additionally, secondary cracking at the interior for Ti-23.5Al-16.5Nb was at times transgranular where cracking appeared to nucleate and grow from grain boundaries, Figure 46.

TMC Correlation

MMCs, when loaded parallel to the fibers, show better fatigue resistance than monolithic matrix materials mainly due to the excellent stiffness, strength, and fatigue resistance of the fibers. Correspondingly, at identical stress ranges, the lives of MMCs are longer than their respective monolithic matrix materials. In general, one would expect the scatter in fatigue data of composites to be much greater than that in fatigue of monolithic materials. This is because of the existence of additional damage mechanisms in composites, such as random distribution of matrix microcracks, fiber/matrix interface debonding, fiber breaks, and so on.

It is well documented that cracks, originating from areas acting as stress risers, led to failure of titanium aluminide composite specimens[2,3,7,16,28,50,51]. It is also well established that environmental damage played a significant role in the failure process where environmentally assisted cracking has been found to initiate at surface locations in several creep, IF, thermal cycling, and TMF test samples[1,5-7,9,10,15,16,28,34]. This suggests that the surface plays a decisive role in the damage processes. In TMF, a matrix dominated failure, initiated by matrix microcracking at embrittled surface locations, is

compatible with the fact that OOP conditions maximize the longitudinal stress and stress range in the matrix. Therefore, it is justified that for life prediction purposes, since surface initiated cracking contributes to the life of composites and monolithics, it should be used in modeling efforts.

From the fractography results and discussion, it was deduced that cracks initiated at surface locations in all monolithic cases. A correlation has been drawn between the monolithic and composite data which takes into account matrix stresses which may induce crack initiation at locations away from the fiber/matrix interface, Figures 55 and 56 located in Appendix D. The correlation links effective stress range at the modeled surface of the matrix to applied stress range of the monolithic. These stress ranges are then applied to the corresponding cycles-to-failure experienced experimentally. A relationship exists within the material groupings, Timetal 21S and Ti-24Al-11Nb, which suggests the composite data can be bounded by multiplying the monolithic life as described by the power law equation by factors of 1.5 for the lower bound and 3 for the upper bound, Figure 57. Due to the correlation noted for the alloys modeled, a similar relationship is expected for the Ti-23.5Al-16.5Nb alloy as well.

CHAPTER VI

SUMMARY AND CONCLUSIONS

This work discussed the results of a systematic study of OOP TMF testing of three titanium alloys: Timetal 21S (beta), Ti-24Al-11Nb (alpha-2 + beta), and Ti-23.5Al-16.5Nb (alpha-2 + beta + orthorhombic). Each alloy has recently been used as matrix materials for composites. The objective was to identify differences between the separate monolithic alloys and to better estimate the OOP TMF behavior of the respective titanium matrix composites: SCS-6/Timetal 21S, SCS-6/Ti-24Al-11Nb(at%), and SCS-6/Ti-23.5Al-16.5Nb(at%). The load, temperature, and strain activities were monitored as the specimens were subjected to OOP TMF conditions. In the interpretation of the data, a correlation of the experimental monolithic life to the experimental composite life was noted. Fractography, metallography, and supplementary data, such as micromechanical stress and strain, aided in a better understanding of this relationship.

The monolithic specimens tested failed due to a combination of fatigue, oxidation, and creep damage mechanisms. Timetal 21S experienced the longest lives at the higher stress ranges, > 525 MPa, than the other alloys, where oxidation and creep were evident in the damage evolution. Timetal 21S specimens failed in a ductile manner where more crack initiation sites developed for the higher maximum stresses. Ti-24Al-11Nb experienced the longest life at the lowest stress level, 350 MPa. Crack initiation occurred at corner locations for each specimen. Environmentally assisted cracking and crack growth in the form of oxygen embrittlement significantly lowered lives at higher stress ranges. A cleavage type overload fracture was observed in all cases. Ti-23.5Al-16.5Nb

experienced longer lives than the other alloys at the intermediate stress ranges. The specimens failed in a brittle type manner, and cracking initiated at locations both along the surface faces and edges. At higher stress levels this alloy displayed an intermediate fatigue strength lower than Timetal 21S but higher than Ti-24Al-11Nb. Similarly, at the lowest stress level this alloy displayed an intermediate fatigue strength, lower than Ti-24Al-11Nb but higher than Timetal 21S.

A correlation was proposed linking monolithic behavior to composite behavior. Composite life was modeled employing both a micromechanical code, to calculate matrix stresses during the OOP TMF cycling, and the experimental data, while monolithic life was modeled using applied stress range and experimental data.

Recommendations

1) Additional testing on other titanium alloy systems is necessary if this correlation is to be better understood and adapted.

2) Data points taken outside the stress ranges tested may aid the curve fit offered in both the composite and monolithic test matrices analyzed.

3) Testing of neat materials which more closely represents the composite matrix condition should provide a better example of matrix behavior.

4) Not enough time was devoted to analyzing the significantly different matrix micromechanical stress behaviors occurring radially outward from the fiber/matrix interface for the respective composite systems. A more in-depth study, beyond the scope of this thesis, could be conducted investigating the reasons and resulting effects of these differences.

5) Testing of the near-orthorhombic composite systems is necessary to verify the relationship between monolithic and composite TMF lives proposed.

6) A life prediction model for both the monolithic and respective composite materials was determined beyond the scope of this thesis and should be given consideration in a future study.

APPENDIX A

The following plots represent FIDEP results of the micromechanical stresses in the constituents of a composite. The plots describe the axial and effective constituent stresses at locations directed radially from the center of a fiber to a distance away from the fiber/matrix interface at an extreme points in the OOP TMF cycle. R is taken from the center of the fiber to the edge of the surrounding matrix at B. To determine the location of the fiber/matrix interface, Ri, Vf is used according to:

$$Vf = (pi)Ri^2/(pi)B^2.$$

Matrix effective stresses are modeled according to:

$$Seff = (0.5^{0.5}) \times [(Sr-Stheta)^2 + (Sr-Sz)^2 + (Sz-Stheta)^2]^{0.5}$$

where Sz, Sr, and Stheta are the matrix axial, radial, and tangential stresses; respectively.

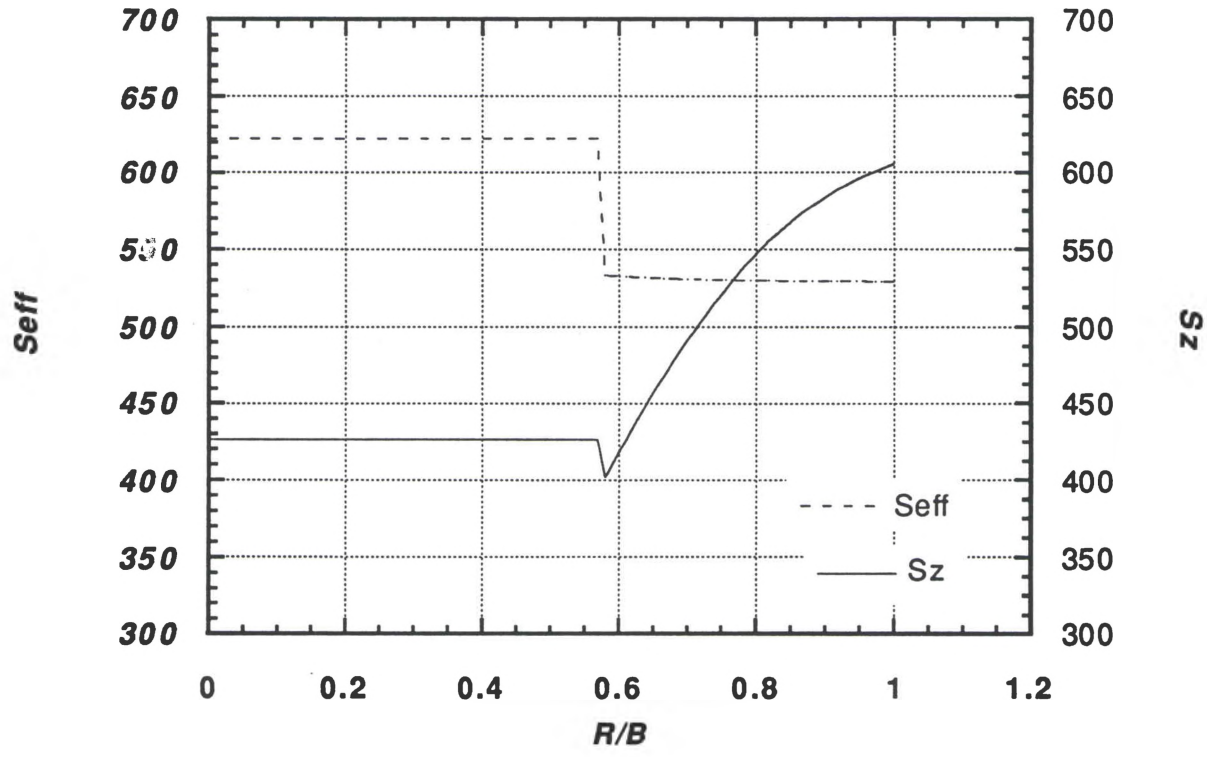

Figure 50. Stresses of the fiber and matrix along a cross-section of the SCS-6/Ti-24Al-11Nb composite at 150°C and 500 MPa of an OOP TMF cycle as calculated using FIDEP.

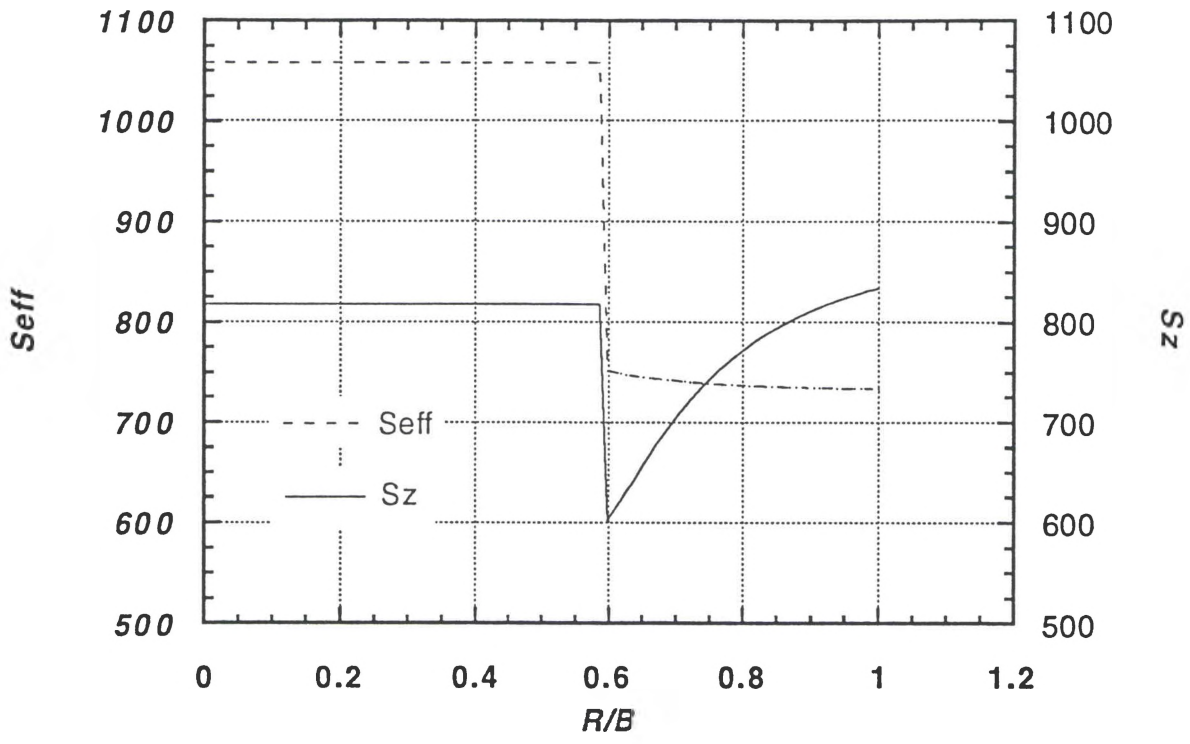

Figure 51. Stresses of the fiber and matrix along a cross-section of the SCS-6/Ti-23.5Al-16.5Nb composite at 150°C and 780 MPa of an OOP TMF cycle as calculated using FIDEP.

APPENDIX B

The following pages provide the tensile data, for both the monolithic alloys and the SCS-6 fiber, which are used in the FIDEP analysis of the micromechanical stresses and strains in the composite systems. The data includes poissons ratio (Nu), elastic modulus (E), CTE, YS, and plastic modulus (EP), all as a function of temperature. Notice that the fiber was modeled in order to account for only elastic behavior and the yield stresses listed are exaggerated. An OOP TMF profile of 150-650°C and R=0.1, in agreement with the experimental parameters, was used in the analysis for each material. The SCS-6/Timetal 21S composite involved heat treatment and subsequent cool down steps in addition to the consolidation and subsequent cool down steps. Consolidation occurred at 900°C while the heat treatment was maintained at 620°C for 8 hours and the fiber volume fraction was either 0.32 or 0.38 according to the tests performed. The consolidation temperature for the SCS-6/Ti-24Al-11Nb(at%) composite was 1010°C and the fiber volume fraction was 0.33. The consolidation temperature for SCS-6/Ti-23.5Al-16.5Nb was 940°C with no appropriate heat treatment developed at this time and a volume fraction of 0.34. All consolidation temperatures mentioned are from actual composite processing data received from Textron. After consolidation a cool down step to room temperature (22°C) with no applied load was entered before the OOP TMF cycle was initiated.

Table 6. Tensile Data

Timetal 21S data acquired from Round Robin Stress Control Tests performed at WPAFB
Strain rate = 0.0008344

T(°C)	Nu	E(GPa)	CTE($x10^{-6}$mm/mm/°C)	YS(MPa)	EP(GPa)
21	.34	117	9.4514	1050	3.84
316	.34	101	9.988	775	5.4
482	.34	95.4	10.313	690	6.38
566	.34	78.1	10.477	470	16.96
621	.34	73.2	10.59	289	14.72
650	.34	70.6	10.651	269	0
900	.34	50.9	11.168	94	0

Ti-24Al-11Nb data acquired by UDRI, tests performed at WPAFB
Strain rate = 0.0008344

T(°C)	Nu	E(GPa)	CTE($x10^{-6}$mm/mm/°C)	YS(MPa)	EP(GPa)
20	.3	94	11.31	604	1.3
93	.3	92	11.48	560	0.9
204	.3	91	11.69	498	.719
316	.3	89	11.88	447	.692
427	.3	79	12.096	421	.415
538	.3	70	12.365	381	.11
649	.3	49	12.727	356.5	0
760	.3	24.5	13.217	252.4	2.35
871	.3	18	13.87	138.3	2.62
982	.3	15.9	14.72	38.04	1.18
1010	.3	15	14.972	30	1

Ti-23.5Al-16.5Nb data acquired by Krishnamurthy, tests performed at WPAFB
Displacement rate = 0.21mm/s

T(°C)	Nu	E(GPa)	CTE($x10^{-6}$mm/mm/°C)	YS(MPa)	EP(GPa)
23	.3	106	unavailable	807	5.9
593	.3	113	unavailable	471	3.2
760	.3	60	unavailable	197	2

SCS-6 Fiber: data acquired by UDRI, tests performed at WPAFB

T(°C)	Nu	E(GPa)	CTE($x10^{-6}$mm/mm/°C)	YS(GPa)	EP(GPa)
20	.3	413	4.5834	1000	0
101	.3	413	4.7007	1000	0
203	.3	413	4.8503	1000	0
299	.3	413	4.9829	1000	0
400	.3	413	5.1238	1000	0
500	.3	413	5.2348	1000	0
598	.3	413	5.3451	1000	0
702	.3	413	5.453	1000	0
800	.3	413	5.5461	1000	0
900	.3	413	5.6288	1000	0
1001	.3	413	5.7124	1000	0
1010	.3	413	5.719	1000	0

APPENDIX C

The following tables includes cyclic maximum and minimum temperature data monitored on the demonstration specimen while the "dummy" specimen temperature controlled the tests. The tests were performed with a maximum stress of 50MPa, R=0.05, and frequency=0.00556Hz. The data is depicted in graphical form after the corresponding tables are given for both Ti-24Al-11Nb and Ti-23.5Al-16.5Nb. One thermocouple reading could be acquired at the maximum and minimum temperature of each cycle due to the availability of only one thermocouple readout gage. During testing of the Ti-24Al-11Nb and Ti-23.5Al-16.5Nb specimens, the "dummy" specimens, heated from 100-580°C and 130-630°C; respectively, controlled the test specimen's temperature.

Table 7. Temperature Mapping for Ti-24Al-11Nb

Ti-24Al-11Nb: Recorded cycles temperature of demonstration specimen while the "dummy" specimen was controlled from 100-580°C.

Cycle	TC#6		TC#7		TC#8		TC#9	
1							628	144
3					635	153		
4			633	150				
5	637	152						
6							644	147
7					654	152		
8			650					
9	642	151						
11			648	152				
12	644							
13							657	144
14					662	150		
15			655	149				
16	644	151						
17							648	145
18					653	145		
19	644		653					
20	641							
22			651					
23	643							146
24					145		654	
25							648	
54	646	152						
55			654	149				
56					656	149		
57							653	145
60	643							
62							650	
63						141		
64			657	149				
66	652	148						
95							645	143
96					655	150		
97			647	150				
98			649	149				
99	647	152						
100							644	143
117								142
118							651	143
119						151		
510							643	146
511					654	151		
512			650	149				
513		153						
514	642							
517							649	144
518					650	151		

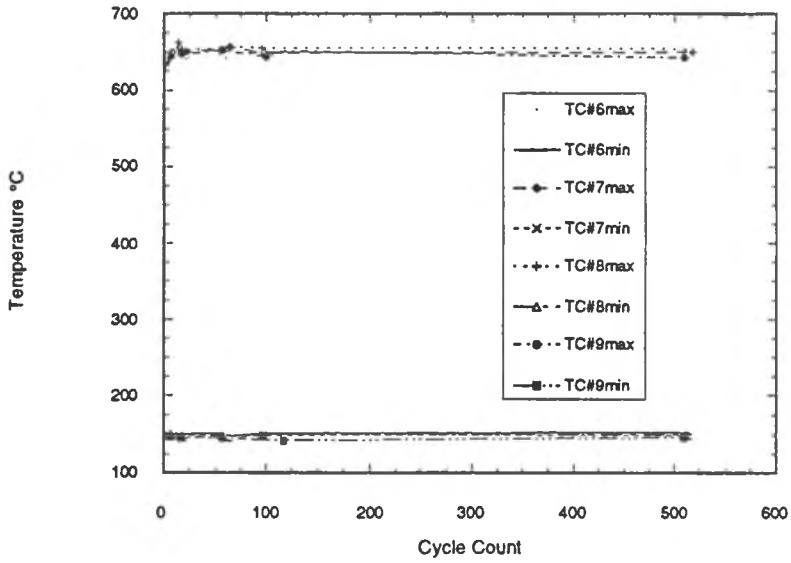

Figure 52. Demonstration specimen temperature vs cycle count for Ti-24Al-11Nb.

Table 9. Temperature Mapping for Ti-23.5Al-16.5Nb

Ti-23.5Al-16.5Nb: Recorded cycle temperature of the demonstration specimen while the "dummy" specimen was controlled from 130-660°C.

Cycle	TC#6		TC#7		TC#8		TC#9	
0					616	167		
1			633	172				
2	633	173						
3		165					665	
4							660	141
5					649	140		
6			154	653				
7	167	650						
8							663	144
9					641	146		
10			653	151				
11	653	166						
12							664	148
13					648	149		
14			649	156				
15	653	167						
16							665	149
17					651	148		
18			651	156				
19	652	167						
20							667	149
21	651	167						
82							664	148
83					649	145		
84			651	153				
85	656	163						
159							669	144
160					653	145		
161			648	152				
162	652	165						
583	657	163						
584			654	149				
585					649	142		
586							658	144
588							661	

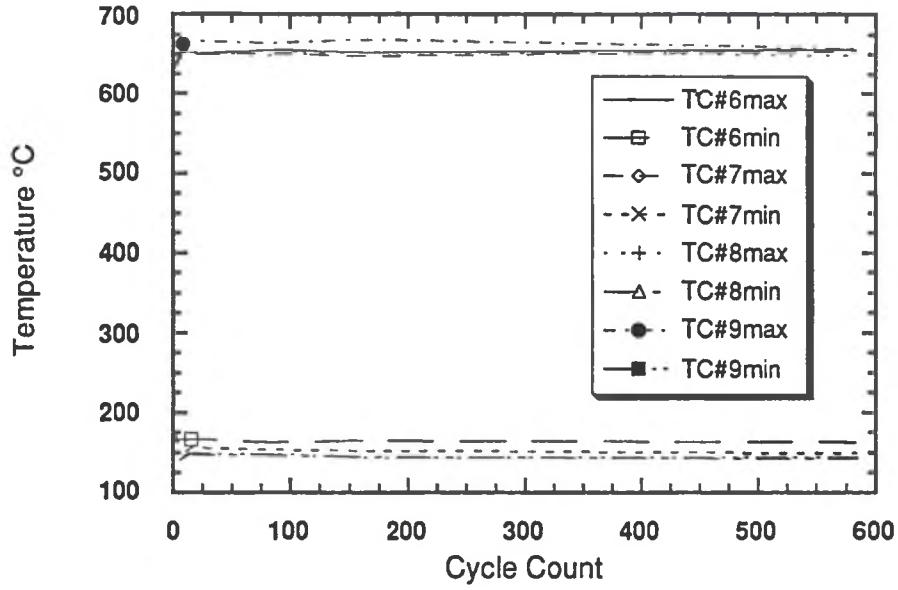

Figure 53. Demonstration specimen temperature vs cycle count; Ti-23.5Al-16.5Nb.

APPENDIX D

Correlation

In the attempt to correlate the OOP TMF life of TMCs with the respective monolithic materials, the monolithic matrix lives, determined experimentally, were compared to composite lives, from previous testing efforts which are presented in Appendix E. The purpose of this analysis is to evaluate parameters which may enable the prediction of composite material behavior through testing of monolithic materials.

For modeling purposes the micromechanical stresses and strains during the composite consolidation, heat treatment (if available), and loading conditions were calculated using FIDEP. Cycles to failure were compared using several parameters. The parameters investigated included applied stress range, maximum applied stress, and micromechanical stresses within the matrix. For the micromechanical parameters, eight variations were evaluated. The comparisons included the maximum applied stress and applied stress range of the monolithic materials to FIDEP matrix axial and effective maximum stresses and stress ranges at two locations, the fiber/matrix interface and the greatest radial distance away from the fiber. It should be emphasized that the main thrust of this analysis is not to develop a comprehensive set of guidelines to judge TMCs from monolithic materials. Instead, the objective is to demonstrate trends which suggests that the OOP TMF behavior of the unidirectional TMCs analyzed, relates to that of the

monolithic titanium matrices tested. Therefore, there was no attempt to further refine, weight, or normalize the correlation.

There seemed to be no apparent correlation of the data using maximum applied stress or applied stress range. The latter is depicted in Figure 54. This observation, combined with results of the fracture analysis led to the consideration of matrix effective stress range at the greatest radial distance away from the fiber in the concentric cylinder model as the correlating parameter linking composite to monolithic for life prediction.

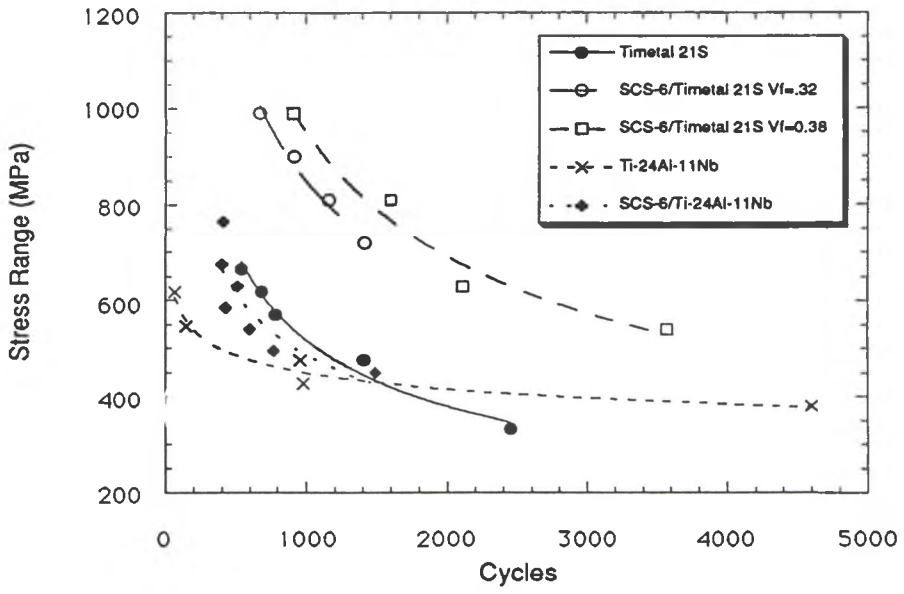

Figure 54. Applied stress range versus cycles-to-failure for monolithic and composite Timetal 21S and Ti-24Al-11Nb.

Depicted in Figures 55 and 56 are the power law curve fits for the monolithic tests versus cycles-to-failure for both Timetal 21S and Ti-24Al-11Nb; respectively. The monolithic curves are compared to the matrix effective and axial stress ranges both at points closest to and farthest away radially from the fiber/matrix interface versus experimentally determined cycles-to-failure for the two corresponding composite systems. For Timetal 21S, the monolithic lives are reduced by approximately a factor of

two as compared to the matrix effective stress range away from the fiber/matrix interface of the composite.

As for the Ti-24Al-11Nb, a similar correlation between the monolithic and the composite data was observed. Based on FIDEP output, the effective stress range as calculated at the location furthest away from the fiber/matrix interface presents a good correlation, Figure 56. Together with the surface initiated cracking, these results express a linking parameter between the composite and monolithic OOP TMF lives.

Assuming a similar frequency effect as noted by Nicholas and Russ[6] under isothermal fatigue of the same composite, the composite data was adjusted to account for the longer cycle time than used during the monolithic testing, 6 minutes and 3 minutes respectively. Taking into account this frequency effect assumption, the monolithic lives are reduced by approximately a factor of two as compared to the matrix effective stress range away from the fiber/matrix interface of the composite. This finding was similar to that of Timetal 21S.

In an attempt to bound the Seff range away from the fiber/matrix interface versus experimental data curves, the monolithic cycles-to-failure were multiplied by a factor of 1.5, for the lower bound, and 3, for the upper bound, and plotted against the same applied stress range, Figure 58 This relationship, for Timetal 21S and Ti-24Al-11Nb, serves to bound the modeled composite well.

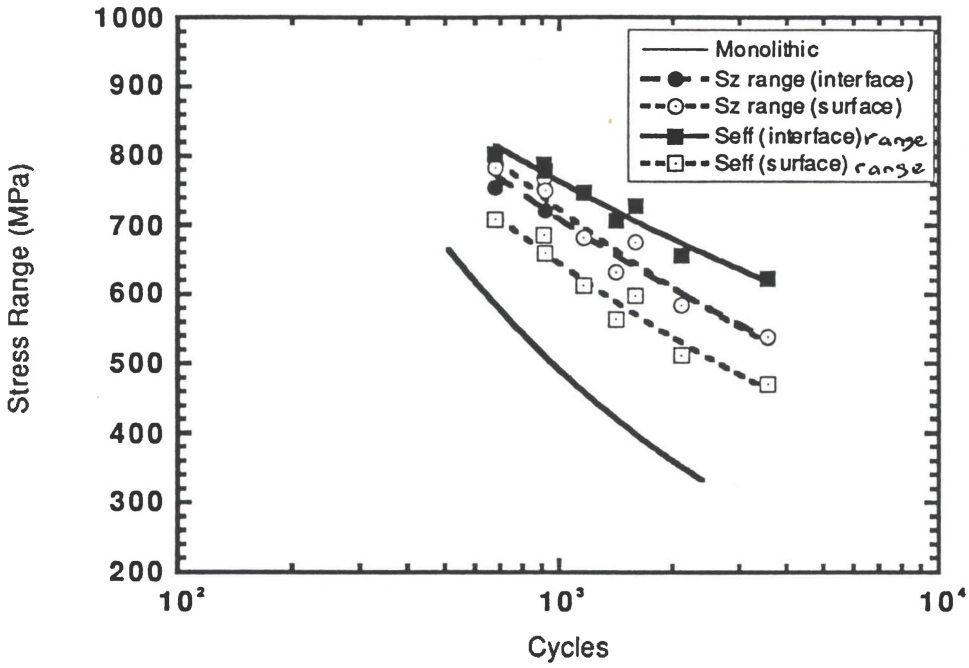

Figure 55. FIDEP Correlations for Timetal 21S

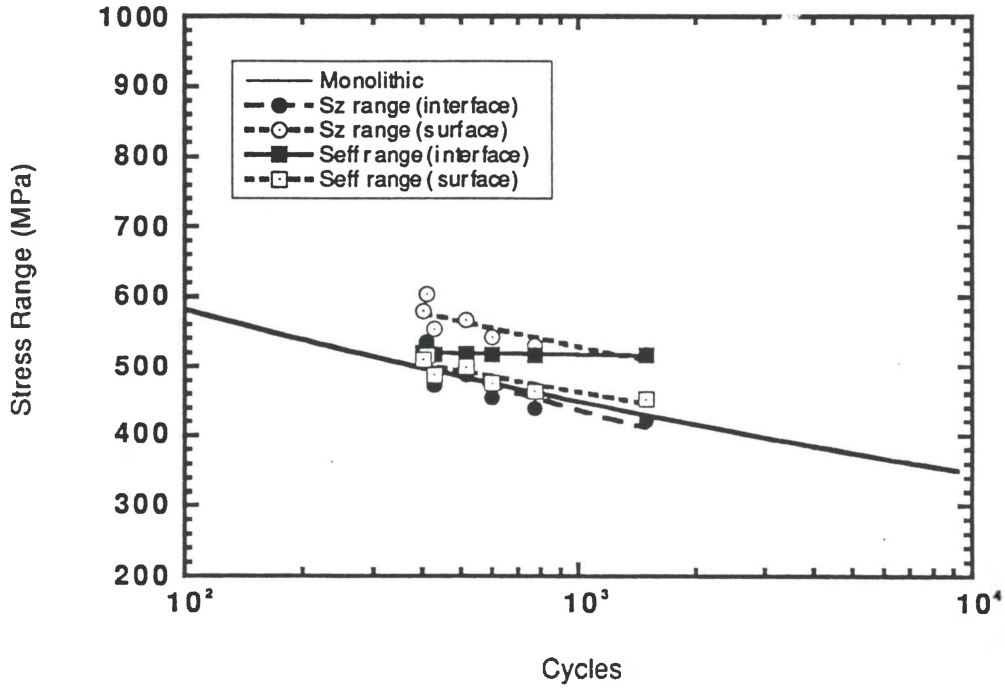

Figure 56. FIDEP Correlations for Ti-24Al-11Nb

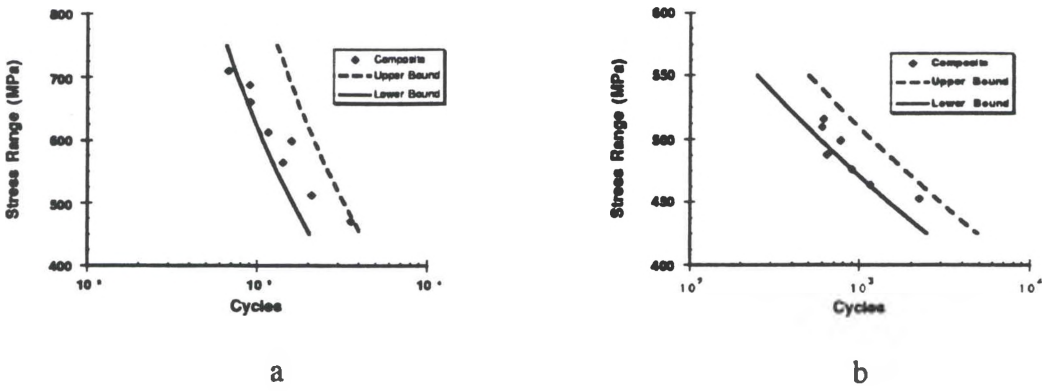

Figure 57. Boundary plots for a) Timetal 21S and b) Ti-24Al-11Nb

APPENDIX E

The following pages provide the SCS-6/Timetal 21S and Ti-24Al-11Nb OOP TMF data as performed by Neu and Russ; respectively. Listed for each material are test parameters and test data including plots of stress range versus cycles-to-failure.

Table 9. OOP TMF S-N Data of SCS-6/Timetal 21S Vf=0.32

Tests were performed from 150-650°C with frequency = 0.00556 Hz and R=0.01.

Maximum stress MPa	Cycles-to-Failure
1100	675
1000	919
900	1162
800	1414

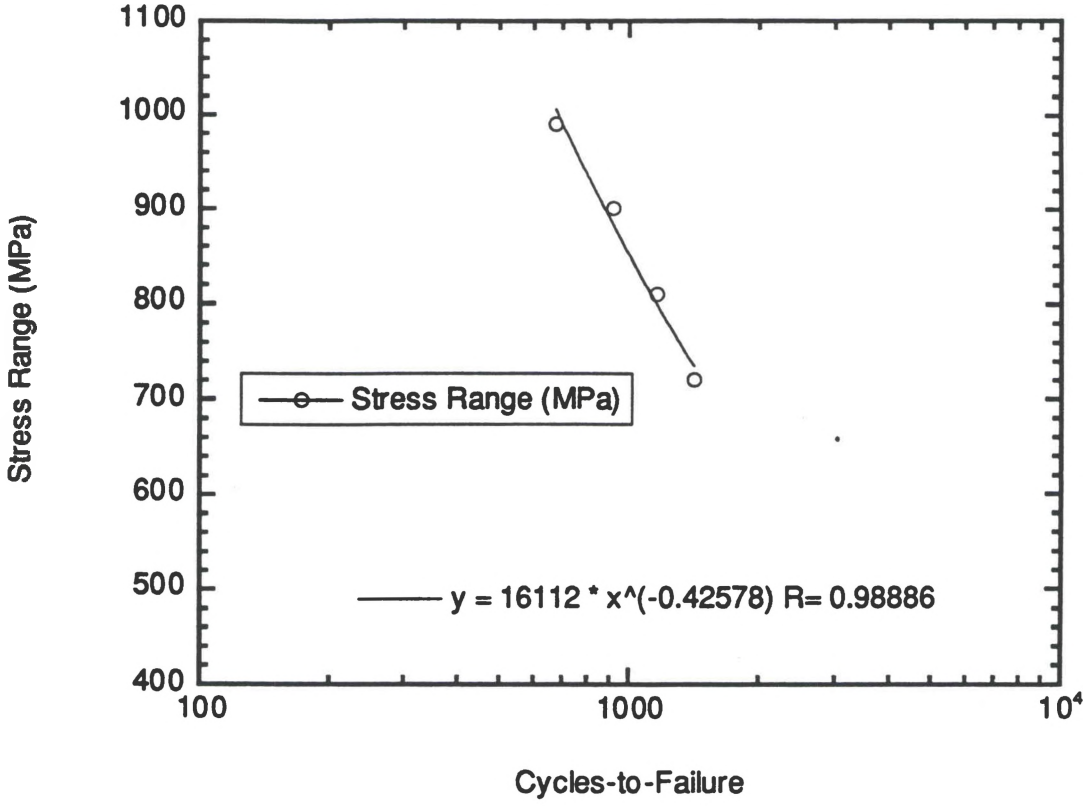

Figure 58. Stress range versus cycles-to-failure for SCS-6/Timetal 21S, Vf = 0.32.

Table 10. OOP TMF S-N Data of SCS-6/Timetal 21S Vf=0.38

Tests were performed from 150-650°C with frequency = 0.00556 Hz and R = 0.01.

Maximum stress MPa	Cycles-to-Failure
1100	410
900	1597
700	2112
600	3574

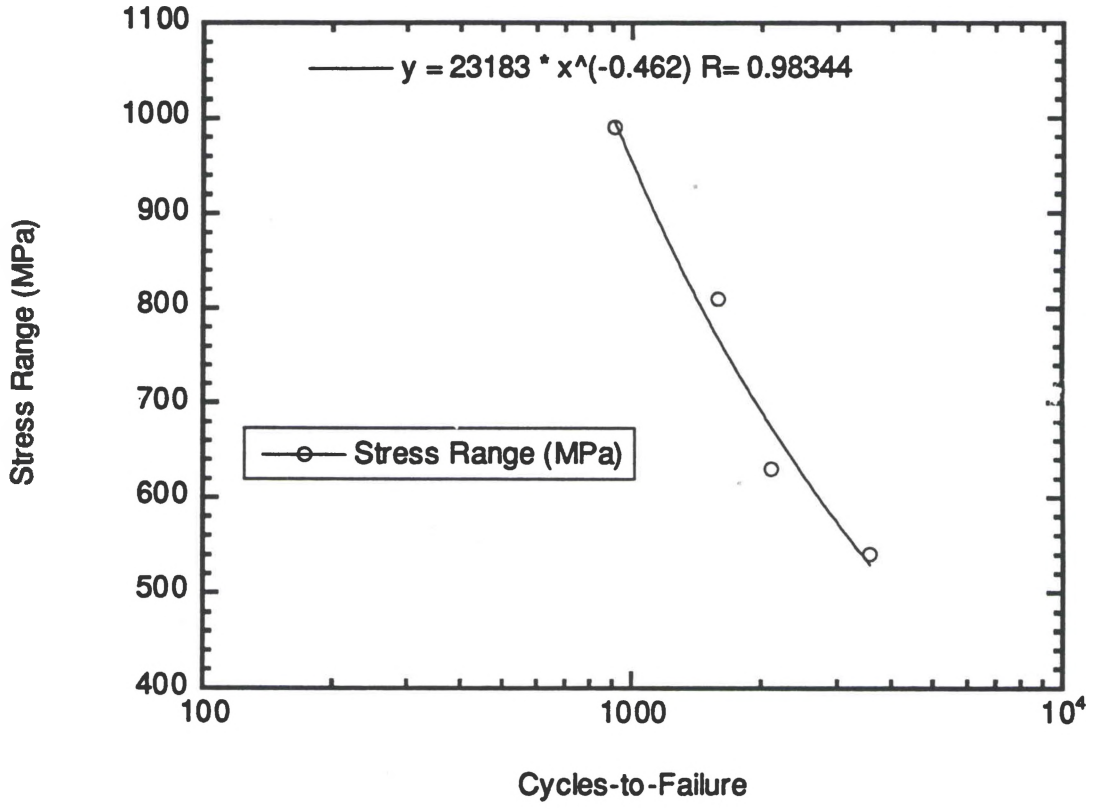

Figure 59. Stress range versus cycles-to-failure for SCS-6/Timetal 21S, Vf = 0.38.

Table 11. OOP TMF S-N Data of SCS-6/Ti-24Al-11Nb Vf=0.33

Tests were performed from 150-650°C with frequency = 0.00288Hz and R = 0.01.

Maximum stress MPa	Cycles-to-Failure
850	410
750	402
700	514
650	428
600	598
550	771
500	1487

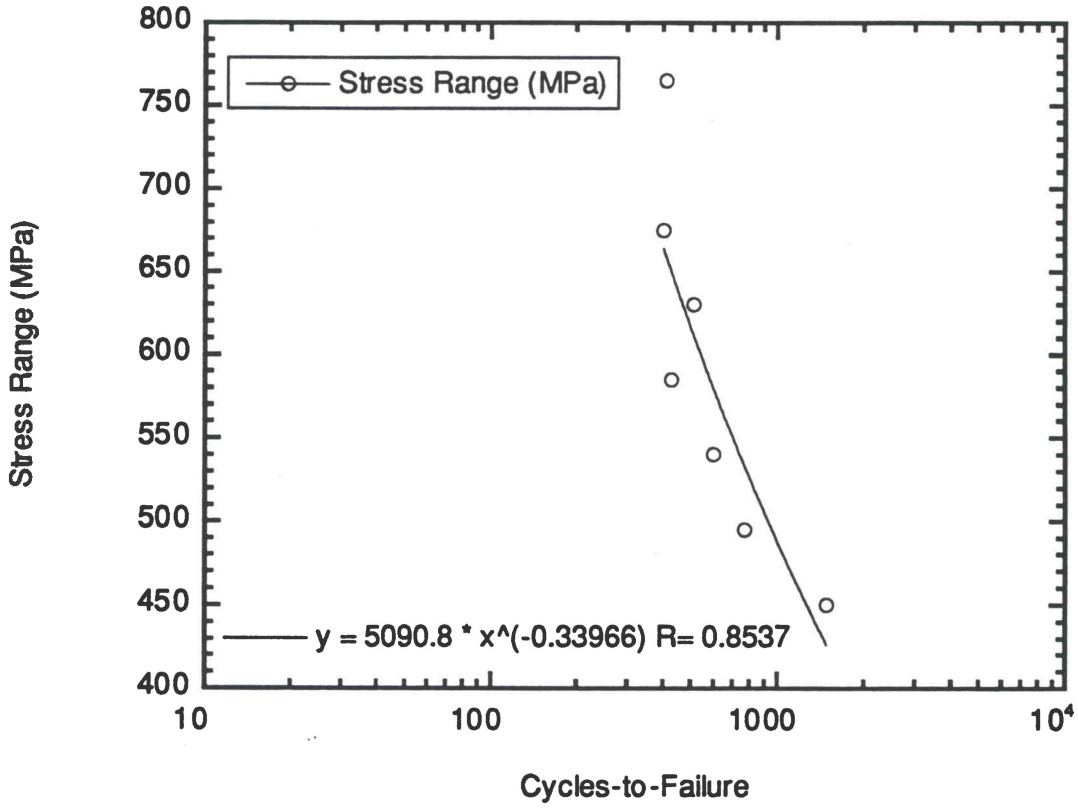

Figure 60. Stress range versus cycles-to-failure for SCS-6/Ti-24Al-11Nb, Vf = 0.33.

Appendix F

The following pages include the strain versus displacement curves from the start-up of the TMF tests where temperature is ramped from room temperature to maximum temperature with negligible load applied. The graphs are given only for the tests that were performed with the controlling thermocouples directly on the specimen. CTEs can be approximated from these curves by taking the slope of the linear curve fit.

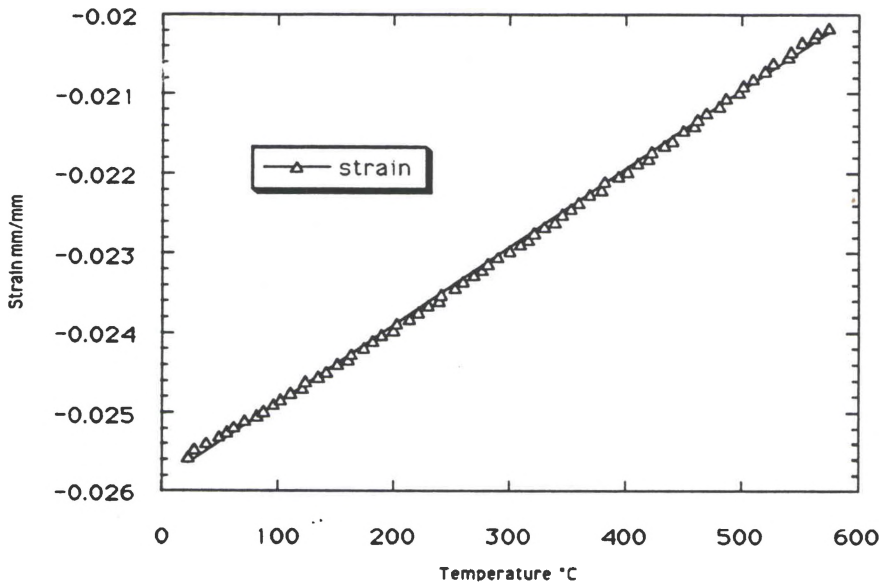

Figure 61. Strain versus temperature for Timetal 21S; specimen #92-504.

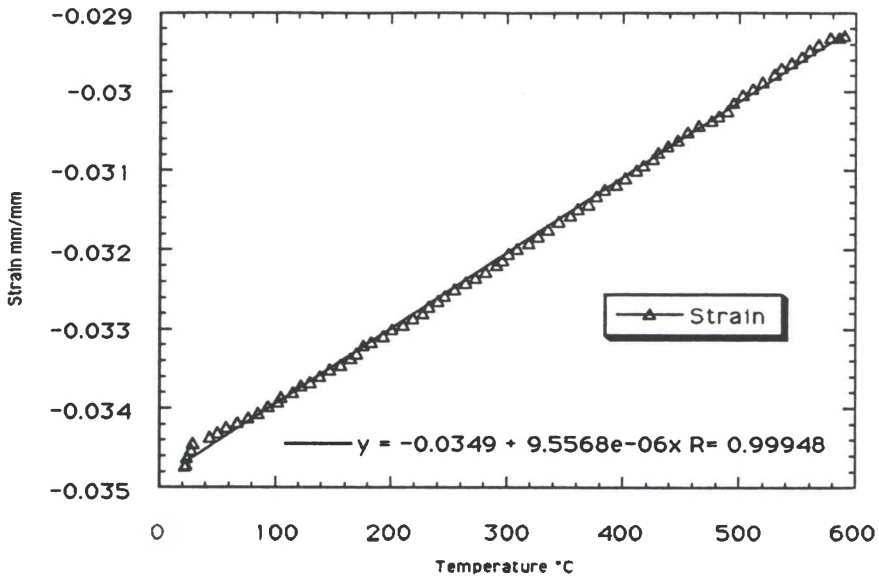

Figure 62. Strain versus temperature for Timetal 21S, specimen #92-501.

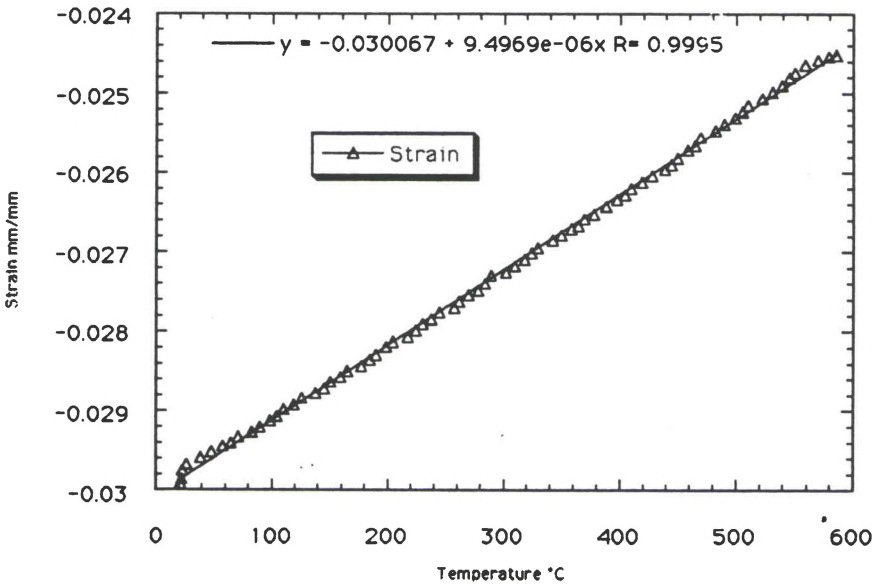

Figure 63. Strain versus temperature for Timetal 21S; specimen #92-503.

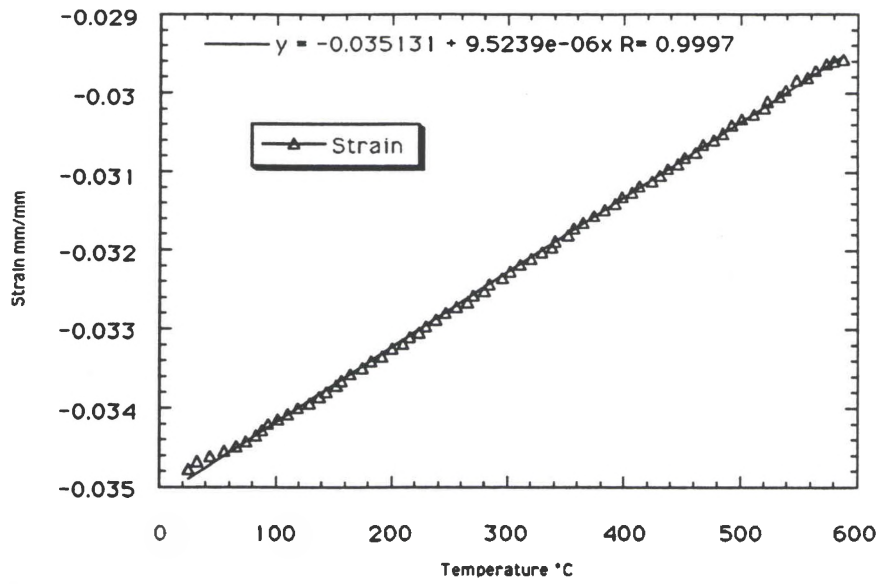

Figure 64. Strain versus temperature for Timetal 21S; specimen #92-502.

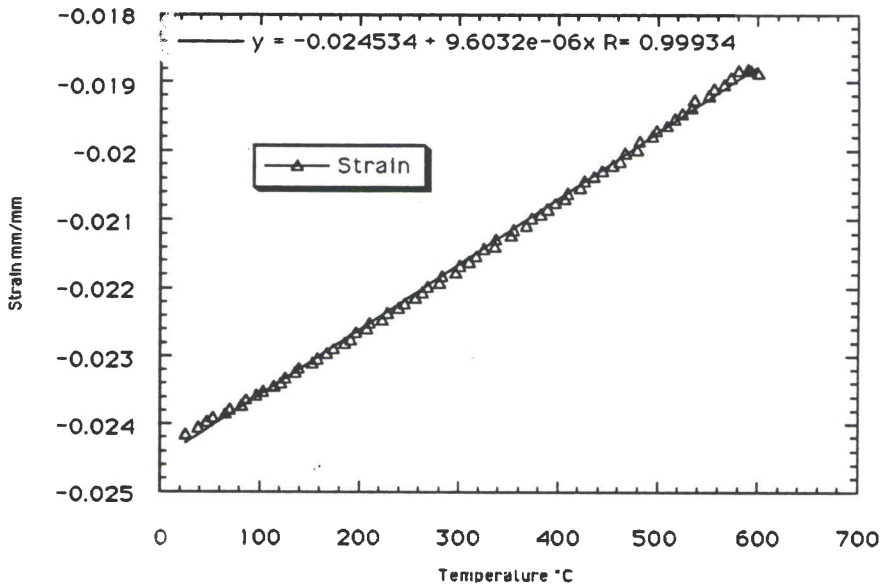

Figure 65. Strain versus temperature for Timetal 21S; specimen #92-500.

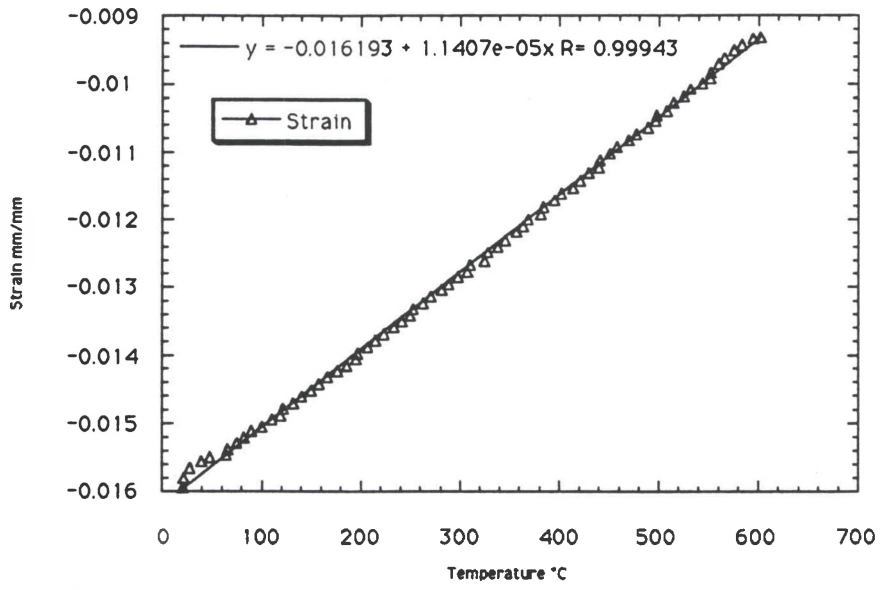

Figure 66. Strain versus temperature for Ti-24Al-11Nb, specimen #92-524.

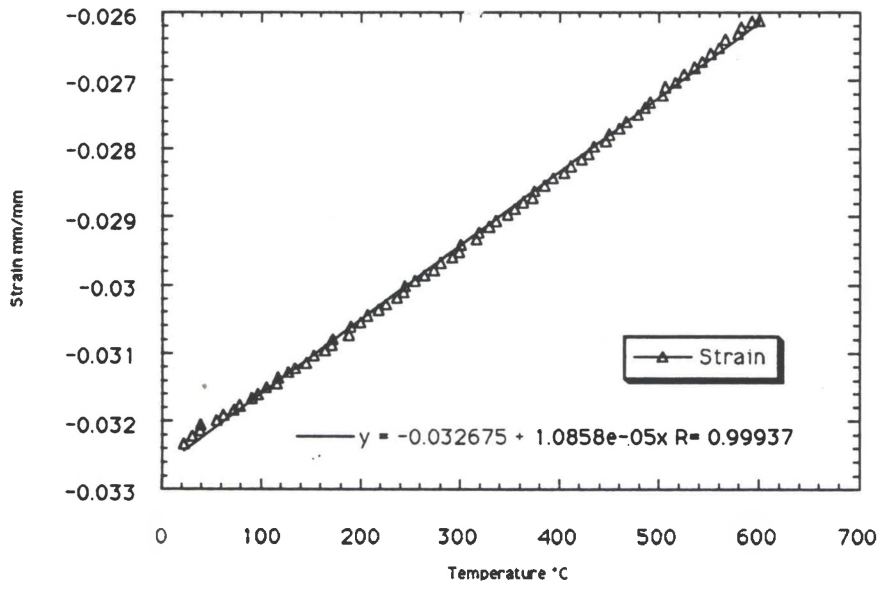

Figure 67. Strain vs temperature for Ti-23.5Al-16.5Nb, specimen #93-239.

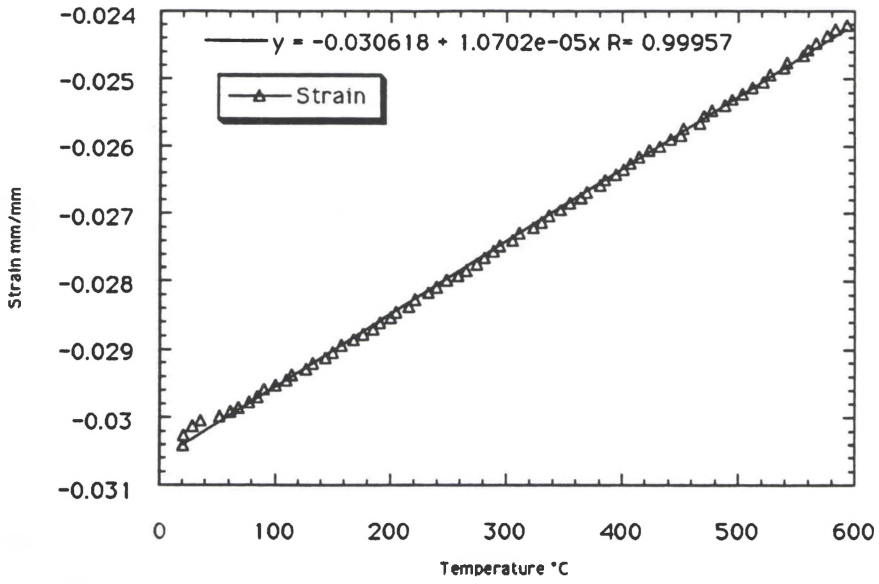

Figure 68. Strain versus temperature for Ti-23.5Al-16.5Nb; specimen #92-530.

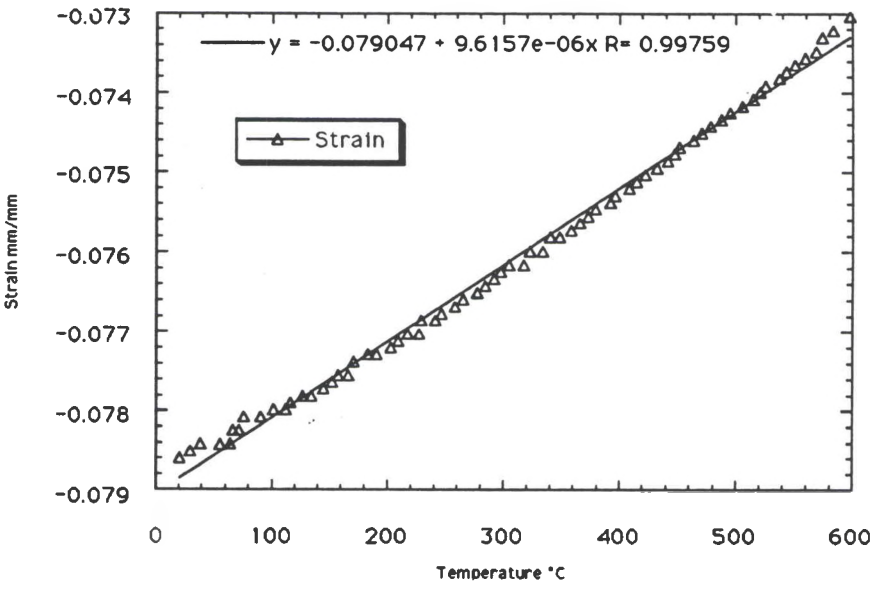

Figure 69. Strain vs temperature for Ti-23.5Al-16.5Nb, specimen #92-682.

APPENDIX G

The following pages provide a listing of the maximum/minimum strain versus cycles plots for each of the specimens not exhibited in Chapter IV.

Timetal 21S

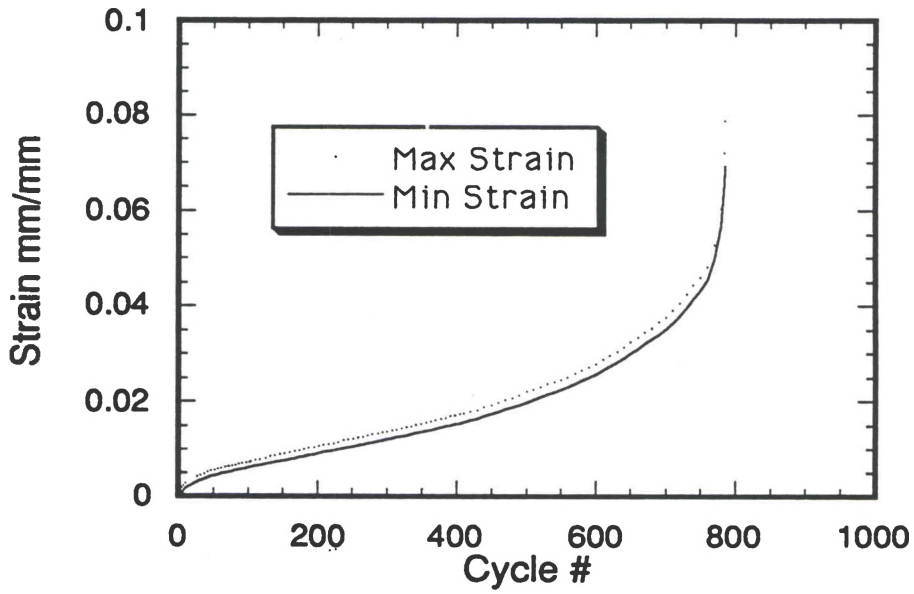

Figure 70. Max/min strain versus cycles for Timetal 21S at max stress = 600 MPa.

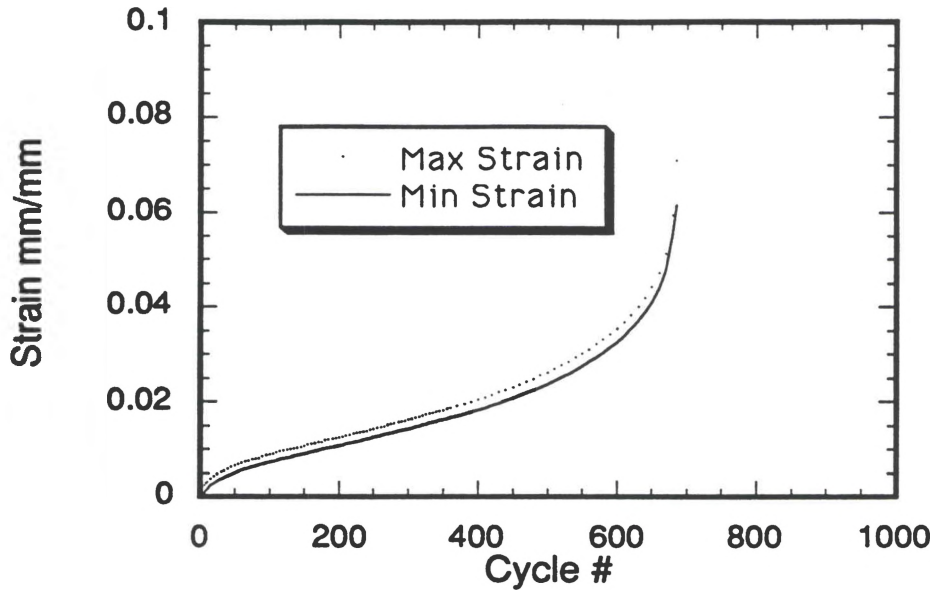

Figure 71. Max/min strain versus cycles for Timetal 21S at max stress = 650 MPa.

Ti-24Al-11Nb

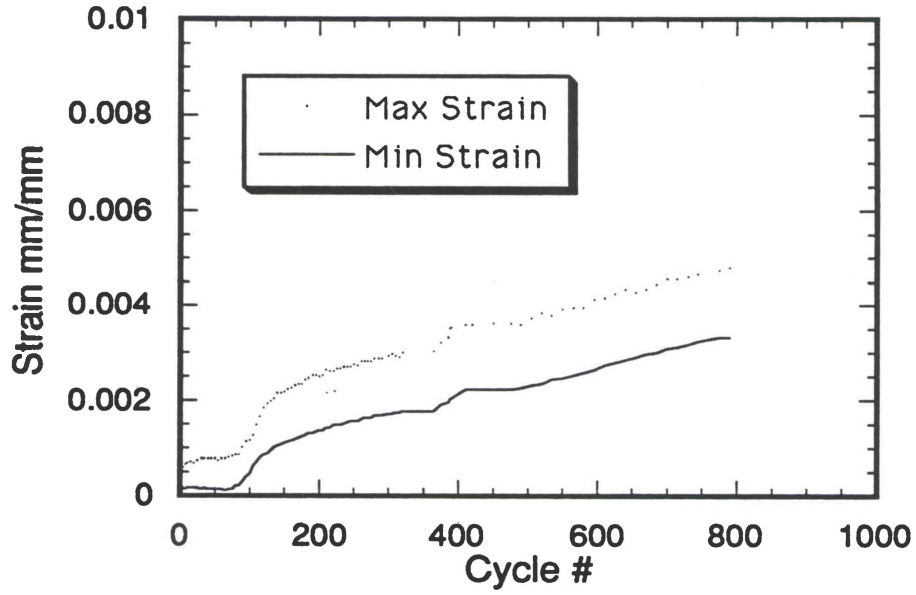

Figure 72. Max/min strain versus cycles for Ti-24Al-11Nb at max stress = 450 MPa.

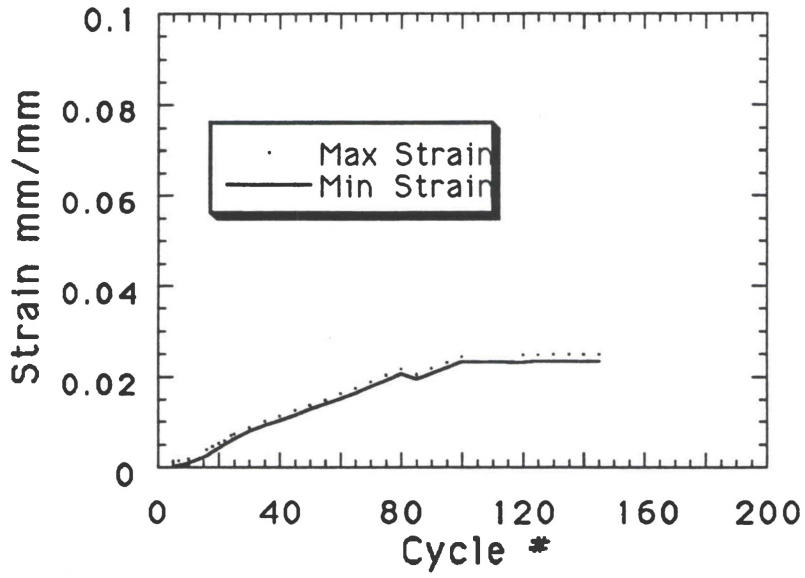

Figure 73. Max/min strain versus cycles for Ti-24Al-11Nb at max stress = 575 MPa.

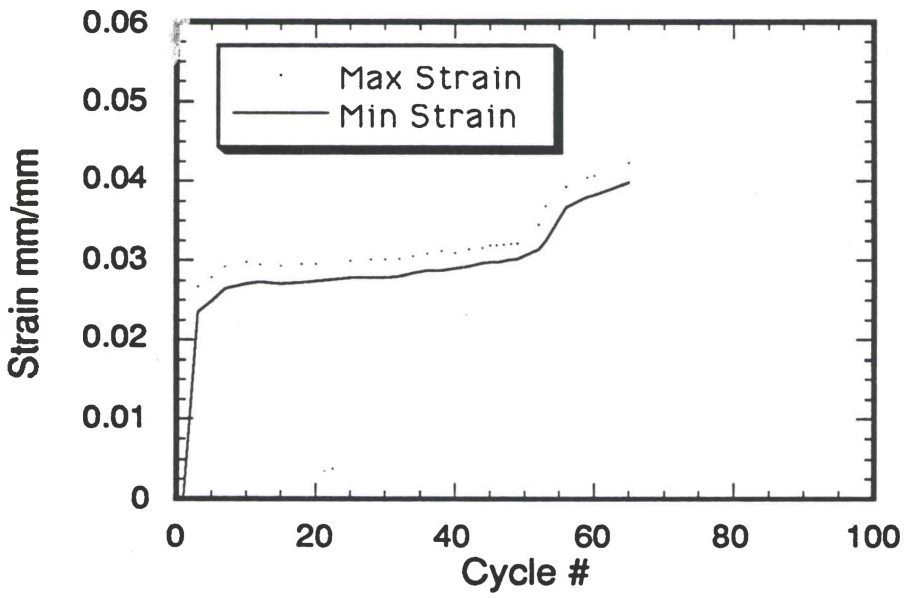

Figure 74. Max/min strain versus cycles for Timetal 21S at max stress = 650 MPa.

Ti-23.5Al-16.5Nb

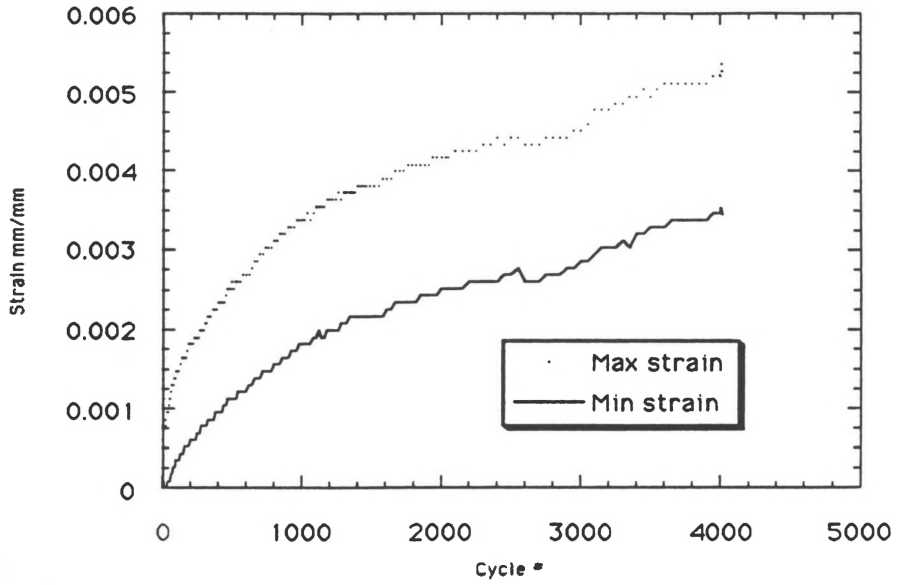

Figure 75. Max/min strain vs cycles for Ti-23.5Al-16.5Nb at max stress = 400 MPa.

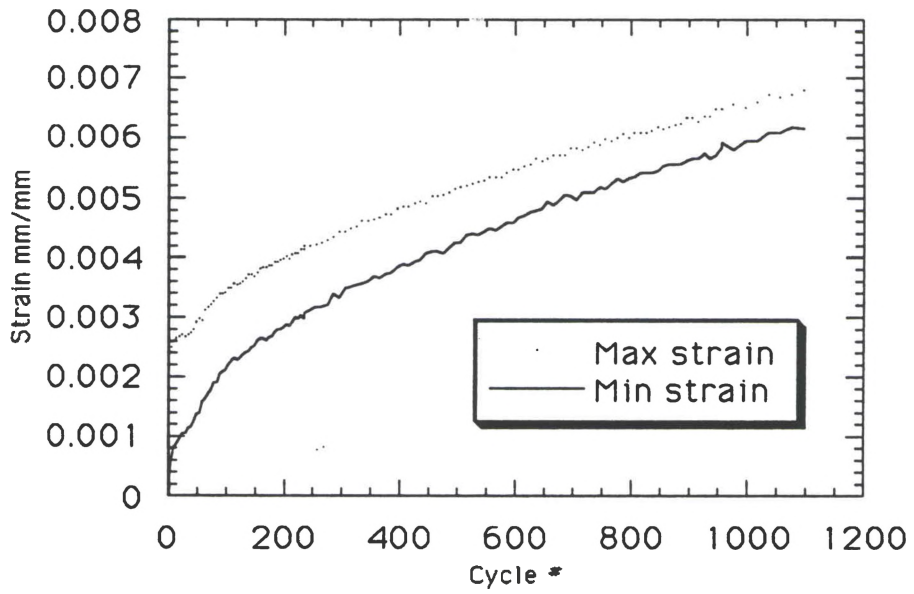

Figure 76. Max/min strain vs cycles for Ti-23.5Al-16.5Nb at max stress = 550 MPa.

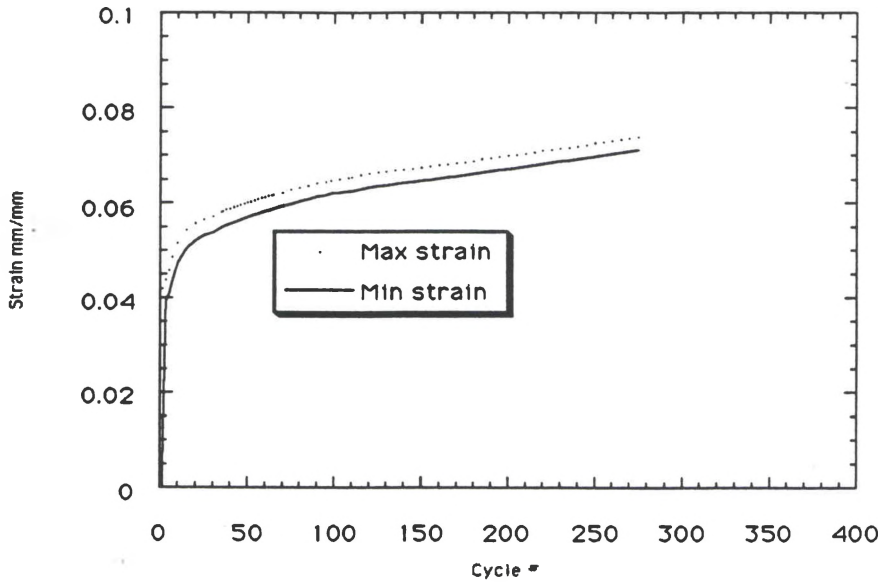

Figure 77. Max/min strain vs cycles for Ti-23.5Al-16.5Nb at max stress = 700 MPa.

BIBLIOGRAPHY

1. Revelos, W.C. and Smith, P.R., "Effect of Environment on the Thermal Fatigue Response of a Ti-24Al-11Nb/SCS-6 Composite," ***Titanium Aluminide Composites***, P.R. Smith, S.J. Balsone, and T. Nicholas, Eds., WL-TR-91-4020, Wright-Patterson Air Force Base, February 1991, pp 399-415.

2. Russ, S.M. and Nicholas, T., "Thermal and Mechanical Fatigue of Titanium Aluminide Metal Matrix Composites," ***Titanium Aluminide Composites***, P.R. Smith, S.J. Balsone and T. Nicholas, Eds., WL-TR-91-4020, Wright-Patterson Air Force Base, February 1991, pp 431-49.

3. Khobaib, M., "Creep Behavior of SCS-6/Ti-24Al-11Nb Composite," ***Titanium Aluminide Composites***, P.R. Smith, S.J. Balsone and T. Nicholas, Eds., WL-TR-91-4020, Wright-Patterson Air Force Base, February 1991, pp 450-66.

4. Kortyna, B.R. and Ashbaugh, N.E., "Fatigue Characteristics of a Titanium Aluminide Composite," ***Titanium Aluminide Composites***, P.R. Smith, S.J. Balsone and T. Nicholas, Eds., WL-TR-91-4020, Wright-Patterson Air Force Base, February 1991, pp 467-83.

5. Brindley, P.K., MacKay, R.A. and Bartolotta, P.A., "Thermal and Mechanical Fatigue of a SiC/Ti-24Al-11Nb Composite," ***Titanium Aluminide Composites,*** P.R. Smith, S.J. Balsone and T. Nicholas, Eds., WL-TR-91-4020, Wright-Patterson Air Force Base, OH, February 1991, pp 484-96.

6. Nicholas, T. and Russ, S.M., "Elevated Temperature Fatigue Behavior of SCS-6/Ti-24Al-11Nb," ***Journal of Material Science and Engineering***, A153, 1992, pp. 514-519.

7. Russ, S. M. and Nicholas, T., Bates, M. and Mall, S., "Thermomechanical Fatigue of SCS-6/Ti-24Al-11Nb Metal Matrix Composite," ***Failure Mechanisms in High Temperature Composites Materials***, AD-Vol. 22/ AMD-Vol. 122, G.K. Haritos, G. Newaz and S. Mall, Eds., American Society of Mechanical Engineers, New York, 1991, pp 37-43.

8. Das, G., "Microstructure/Property Correlation in a Unidirectional SiC (SCS-6) Fiber-Reinforced Ti-24Al-11Nb Composite," ***Proceedings of the Seventh World Conference on Titanium***, June 1992, San Diego, California.

9. Das, G., Russ, S.M. and Khobaib, M., "Microstructure of Unidirectional SCS-6/Ti-24Al-11Nb Composite Deformed in Tension, Fatigue and Creep," ***Proceedings of the Seventh World Conference on Titanium***, June1992, San Diego, California.

10. Russ, S.M., "Thermal Fatigue of Ti-24Al-11Nb/SCS-6," ***Metallurgical Transactions***, Vol. 21A, June 1990, pp 1595-1602.

11. McAfee, J.L., Spear, S.R., Niemann, J.T. and Lewis, W.J., "The Thermal Stability of Beta 21S Titanium Alloy and it's Suitability as a Matrix Alloy for the X-30 TMC Fuselage," ***Proceedings of the Titanium Matrix Composite Workshop***, May 6-8, 1991, Orlando, Florida, pp 65-79.

12. Smith, P.R., Graves, J.A., Rhodes, C.G., James, M.R., and Porter, J.R., "Evaluation of an SCS-6/Ti-22Al-23Nb "Orthorhombic" Composite," ***Proceedings of the Titanium Matrix Composite Workshop***, May 6-8, 1991, Orlando, Florida, pp 115-44.

13. Hanson, D.G., "Thermomechanical Fatigue of a SCS-6/Timetal 21S [0/90]2s Composite," **Master's Thesis**, December, 1991, Air Force Institute of Technology, Wright-Patterson Air Force Base.

14. Mall,S., Hanson, D.G., Nicholas, T. and Russ, S.M., "Thermomechanical Fatigue Behavior of a Cross-Ply SCS-6/ß21-S Metal Matrix Composite," ***Constitutive Behavior of High Temperature Composites***, MD-Vol. 40, B.S. Majumdar, G.M. Newaz and S. Mall, Eds., American Society of Mechanical Engineers, New York, 1992, pp. 91-106.

15. Mirdamadi, M., Johnson, W.S., Bahei-El-Din, Y.A. and Castelli, M.G., "Analysis of Thermomechanical Fatigue of Unidirectional Titanium Metal Matrix Composites," ***Proceedings of the ASTM Symposium of Composite Materials: Fatigue and Fracture IV***, May 6-9, 199¹, Indianapolis, Indiana.

16. Castelli, M.G., Bartolotta, P.A. and Ellis, J.R., "Thermomechanical Testing of High Temerature Composites: TMF Behavior of SiC(SCS-6)/Ti-15-3, " ***Composite Materials: Testing and Design (Tenth Volume), ASTM STP 1120***, G.C. Grimes, Ed., American Society for Testing and Materials, Philadelphia, 1991.

17. Neu, R.W. and Nicholas, T.,"Effect of Laminate Orientation on the Thermomechanical Fatigue Behavior of a Titanium Matrix Composite", Submitted to ***Journal of Composites Technology and Research***, 1993.

18. Russo, P.A. and Seagle, S.R., "Deformation and Recrystallization of Ti and Its Alloys", **ASM International Home Study and Extension Courses**, H.D. Kessler, Ed., 1989.

19. Spear, S.R., "Evaluation of Silicon Carbide Fiber for Use in Titanium Matrix Composites for NASP Applications," ***Titanium Aluminide Composites***, P.R. Smith, S.J. Balsone and T. Nicholas, Eds., WL-TR-91-4020, Wright-Patterson Air Force Base, February 1991, pp 73-95.

20. Everett, R.K., "Diffusion Bonding", **Metal Matrix Composites: Processing and Interfaces**, R.K. Everett and R.J. Arsenault, Eds., Academic Press Inc., San Diego, California, 1991, pp 17-41.

21. Chawla, K.K., **Composite Materials Science and Engineering**, Springer-Verlag New York Inc., New York, 1987.

22. K.K. Chawla, "Fatigue of Continuously Reinforced MMCs", **Metal Matrix Composites: Properties and Mechanisms**, R.K. Everett and R.J. Arsenault, Eds., Academic Press Inc., San Diego, California, 1991, pp 235-253.

23. Hahn, T. A., "Thermal Expansion of MMCs", **Metal Matrix Composites: Properties and Mechanisms**, R.K. Everett and R.J. Arsenault, Eds., Academic Press Inc., San Diego, California, 1991, pp 329-354.

24. Neu, R.W. and Sehitoglu, H., "Thermomechanical Fatigue, Oxidation and Creep: Part I. Damage Mechanisms," ***Metallurgical Transactions,*** Vol. 20A, September 1989, pp 1755-67.

25. Conway, J., "Creep-Fatigue Interaction", **Metals Handbook**, Ninth Edition, American Society for Metals, Vol. 8 Mechanical Testing, 1985, p. 346.

26. Sehitoglu, H. and Boismier, D.A., "Thermo-Mechanical Fatigue of Mar-M247: Part I. Experiments," ***Engineering Materials and Technology***, Vol. 112, January 1990, pp 68-79.

27. Neu, R.W. and Sehitoglu, H., "Thermomechanical Fatigue, Oxidation and Creep: Part II. Life Prediction," ***Metallurgical Transactions,*** Vol. 20A, September 1989, pp 1769-83.

28. Gabb, T.P. and Gatda, J., "Isothermal and Nonisothermal Fatigue Behavior of a Metal Matrix Composite," ***Journal of Composite Materials***, Vol. 24, 1990 pp 667-676.

29. Johnson, W.S., "Damage Development in Titanium Metal Matrix Composites Subjected to Cyclic Loading," ***Proceedings of the Symposium on Fatigue and Fracture of Inorganic Composites***, March 31 - April 2, 1992, Cambridge, UK.

30. Hertzberg, R.W., **Deformation and Fracture Mechanics of Engineering Materials**, Second Edition, John Wiley and Sons, New York, 1983.

31. Anderson, T.L., **Fracture Mechanics Fundamentals and Applications**, CRC Press Inc., Boca Raton, Florida, 1991.

32. Revelos, W.C., Jones, J.W. and Dolley, E.J., "Thermal Fatigue of SiC/Ti-15Mo-2.7Nb-3Al-0.2Si(wt%) Composites", to be submitted to ***Metallurgical Transactions*** in June 1993.

33. Kwei, L.K. and Chawla, K.K., "Thermal-mechanical Fatigue Behaviour of Alumina Fibre/Aluminium-lithium composite," ***Journal of Material Science***, Vol. 27, February 1992, pp 1101-6.

34. Mall, S. and Ermer, P.G., "Thermal Fatigue Behavior of Unidirectional SCS-6/Ti-15-3 Metal Matrix Composite," ***Journal of Composite Materials***, Vol. 25, December 1991, pp 1668-86.

35. Ball, D.L., "Thermomechanical Fatigue Life Prediction of SCS-6/Beta-21S Composites," ***Proceedings of the Titanium Matrix Composite Workshop***, May 6-8, 1991, Orlando, Florida, pp 372-90.

36. Wright, P.K., "Creep Behavior and Modeling of SCS-6/Titanium MMC," ***Proceedings of the Titanium Matrix Composite Workshop***, May 6-8, 1991, Orlando, Florida, pp 251-76.

37. Martin, P.L., Bingel, W.H. and Mahoney, M.W., "SiC Reinforced ß-21S Creep Properties," ***Proceedings of the Titanium Matrix Composite Workshop***, May 6-8, 1991, Orlando, Florida, pp 277-91.

38. Sehitoglu, H. and Boismier, D.A., "Thermo-Mechanical Fatigue of Mar-M247: Part II. Life Prediction," ***Engineering Materials and Technology***, Vol. 112, January 1990, pp 80-89.

39. Kroupa, J.L., Sherwood, J.A., Ashbaugh, N.E., Quimby, H.M. and Boyle, M.J., "Comparison of Responses of a MMC Using Classical and Unified Constitutive Matrix Behaviors," ***Proceedings of the Titanium Matrix Composite Workshop***, May 6-8, 1991, Orlando, Florida, pp 410-29.

40. Bigelow, C.A., Johnson, W.S. and Naik, R.A., "A Comparison of Various Micromechanics Models for Metal Matrix Composites," ***Mechanics of Composite Materials and Structures***, J.N. Reddy and J.L. Telpy, Eds., Book No. H00464, American Society of Mechanical Engineers, 1989, pp 21-31.

41. Kroupa, J.L., "Elastic-Plastic Finite Element Analysis of MMC subjected to Thermomechanical Fatigue," ***Titanium Aluminide Composites***, P.R. Smith, S.J. Balsone and T. Nicholas, Eds., WL-TR-91-4020, Wright-Patterson Air Force Base, February 1991, pp 576-85.

42. Coker, D., Ashbaugh, N.E. and Nicholas, T., "Analysis of Thermomechanical Cyclic Behavior of Unidirectional Metal Matrix Composites, "***Thermomechanical Fatigue Behavior of Materials***, ASTM STP 1186, American Society for Testing and Materials, Philadelphia, 1990.

43. Buchanon, D.L., "Characterization of SiC/Beta 21S Composites for NASP," ***Proceedings of the Titanium Matrix Composite Workshop***, May 6-8, 1991, Orlando, Florida, pp 236-50.

44. Amato, R.A. and Pank, D.R., "Advanced Titanium Matrix Alloy Development," ***Proceedings of the Titanium Matrix Composite Workshop***, May 6-8, 1991, Orlando, Florida, pp 80-97.

45. Pank, D.A., Ritter, A.M., Amato, R.A. and Jackson, J.J., "Structure-Property Relationships in Ti3Al/SCS-6 Composites," ***Titanium Aluminide Composites***, P.R. Smith, S.J. Balsone and T. Nicholas, Eds., WL-TR-91-4020, Wright-Patterson Air Force Base, February 1991, pp 382-98.

46. Smith, P.R., Rhodes, C.G. and Revelos, W.C., "Interfacial Evaluation in a Ti-25Al-17Nb/SCS-6 Composite," ***Titanium Aluminide Composites***, P.R. Smith, S.J. Balsone and T. Nicholas, Eds., WL-TR-91-4020, Wright-Patterson Air Force Base, February 1991, pp 178-201.

47. Sukonnik, I.M., Smith, P.R., Graves, J.A., Shaw, M.C., Krishnamurthy, S. and Pandley, A., "Advances in Thermomechanical Processing of Titanium Aluminide "Orthorhombic" Foils," ***Proceedings of the Titanium Matrix Composite Workshop***, May 6-8, 1991, Orlando, Florida, pp 98-114.

48. Hartman, G.A. and Russ, S.M., "Techniques for Mechanical and Thermal Testing of Ti3Al/SCS-6 Metal Matrix Composites," ***Metal Matrix Composites: Testing, Analysis and Failure Modes, ASTM STP 1032***, W.S. Johnson, Ed., American Society for Testing and Materials, Philadelphia, 1989, pp 43-53.

49. Hartman, G.A., Zawada, L.P. and Russ, S.M., "Techniques for Elevated Temperature Tensile Testing of Advanced Ceramic Composite Materials," ***Proceedings of the Fifth Annual Hostile Environment and High Temperature Measurements Conference***, 1988, Society for Experimental Mechanics, Costa Mesa, California, pp 31-38.

50. Bampton, C.C. and Graves, J.A., "Process Modeling for Titanium Matrix Composites," ***Proceedings of the Titanium Matrix Composite Workshop***, May 6-8, 1991, Orlando, Florida, pp 145-57.

51. Larsen, J.M., Williams, K.A., Balsone, S.J. and Stucke, M.A., "Titanium Aluminide Composites for Aerospace Applications," ***High Temperature Aluminides and Intermetallics***, S.H. Whang, C.T. Liu, D.P. Pope and J.O. Stiegler, Eds., TMS/ASM International, USA, 1990, pp 521-556.